



**TURUN  
YLIOPISTO**  
UNIVERSITY  
OF TURKU

# DEVELOPMENT OF RADIOPHARMACEUTICALS FOR PET IMAGING OF INFLAMMATION

VAP-1, FR- $\beta$  and CLEVER-1  
as Target Molecules

---

Olli Moisio





**TURUN  
YLIOPISTO**  
UNIVERSITY  
OF TURKU

# **DEVELOPMENT OF RADIOPHARMACEUTICALS FOR PET IMAGING OF INFLAMMATION**

VAP-1, FR- $\beta$  and CLEVER-1  
as Target Molecules

---

Olli Moisio

## University of Turku

---

Faculty of Medicine  
Department of Clinical Physiology and Nuclear Medicine  
Drug Research Doctoral Programme  
Turku PET Centre

## Supervised by

---

Professor Anne Roivainen, PhD  
Turku PET Centre and  
Turku Center of Disease Modelling  
University of Turku  
Turku, Finland

Assistant Professor Xiang-Guo Li, PhD  
Department of Chemistry and  
Turku PET Centre  
University of Turku  
Turku, Finland

## Reviewed by

---

Assistant Professor Cécile Philippe, PhD  
Department of Biomedical Imaging and  
Image-guided Therapy  
Medical University of Vienna  
Vienna, Austria

Associate Professor Peter J.H. Scott, PhD  
Department of Radiology and Center for  
Positron Emission Tomography  
University of Michigan  
MI, USA

## Opponent

---

Professor Jason Phillip Holland, PhD  
Department of Chemistry  
University of Zurich  
Zurich, Switzerland

The originality of this publication has been checked in accordance with the University of Turku quality assurance system using the Turnitin OriginalityCheck service.

ISBN 978-951-29-9070-2 (PRINT)  
ISBN 978-951-29-9071-9 (PDF)  
ISSN 0355-9483 (Print)  
ISSN 2343-3213 (Online)  
Painosalama, Turku, Finland 2022

*To Family and Friends*

UNIVERSITY OF TURKU

Faculty of Medicine

Department of Clinical Physiology and Nuclear Medicine

OLLI MOISIO: Development of Radiopharmaceuticals for PET Imaging of Inflammation - VAP-1, FR- $\beta$  and CLEVER-1 as Target Molecules.

Doctoral Dissertation, 196 pp.

Drug Research Doctoral Programme (DRDP)

November 2022

## ABSTRACT

Positron emission tomography (PET) is a non-invasive technology widely used in oncology, cardiology, neurology and inflammation imaging. PET can detect the expression of receptors, genes and molecular pathways in both patients and experimental animals. Thus far, the radiopharmaceutical 2-deoxy-2- $^{18}\text{F}$ fluoro-*D*-glucose ( $^{18}\text{F}$ FDG) has been employed in the clinic for several indications involving inflammation. While  $^{18}\text{F}$ FDG uptake in regions of inflammation is increased, it is not specific for inflammation, which can lead to difficulty in analysis as well as false positive findings. Therefore, development of alternative, inflammation-specific PET radiotracers is justified.

Our aim is to develop and evaluate new PET radiopharmaceuticals for imaging inflammation-specific targets. We propose these tools may be valuable for both clinical practice and medical research of the inflammatory conditions such as atherosclerosis and rheumatoid arthritis. In this work, three molecules associated with inflammation were selected as targets: vascular adhesion protein-1 (VAP-1), folate receptor  $\beta$  (FR- $\beta$ ) and common lymphatic endothelial and vascular endothelial receptor-1 (CLEVER-1). These receptors are associated with leukocyte recruitment into inflamed tissues as well as activated macrophages at sites of inflammation. Five different radiopharmaceuticals targeting these receptors were evaluated in experimental disease models or in humans.

The results showed that VAP-1-targeting tracers  $^{68}\text{Ga}$ Ga- and  $^{18}\text{F}$ AIF-NOTA-Siglec-9 could visualize sterile skin inflammation in rats. Compared to each other, the tracers showed similar uptake characteristics. Another Siglec-9-derived tracer,  $^{68}\text{Ga}$ Ga-DOTA-Siglec-9 was shown to be safe and well tolerated in healthy volunteers and was able to visualize inflammation in arthritic joints. Further,  $^{68}\text{Ga}$ Ga-NOTA-Folate was successfully used to target FR- $\beta$  positive macrophages in inflamed atherosclerotic lesion in mice. Finally,  $^{89}\text{Zr}$ Zr-DFO-bexmarilimab showed increased uptake in fibrotic rabbit kidneys expressing CLEVER-1.

In conclusion, the tracers studied in this thesis were able to visualize their intended targets in vivo.

**KEYWORDS:** CLEVER-1, fluorine-18, folate receptor  $\beta$ , gallium-68, inflammation, PET, radiometallic labelling, VAP-1, zirconium-89

TURUN YLIOPISTO

Lääketieteellinen tiedekunta

Kliininen fysiologia ja isotooppilääketiede

OLLI MOISIO: Radiolääkeaineiden kehitys tulehduksen PET-kuvantamiseksi

– VAP-1, FR- $\beta$  and CLEVER-1 kohdemolekyyleinä

Väitöskirja, 196 s.

Lääketutkimuksen tohtoriohjelma

Marraskuu 2022

## TIIVISTELMÄ

Positroniemissiotomografia (PET) on ei-invasiivinen kuvantamistekniikka, jota käytetään laajalti onkologiassa, kardiologiassa, neurologiassa ja viime aikoina myös tulehduksen kuvantamisessa. PET:llä voidaan kuvantaa aineenvaihduntaa, reseptorien toimintaa ja geeniekspressiota sekä potilaissa että koe-eläimissä. Toistaiseksi 2-deoksi-2- $^{18}\text{F}$ fluori-*D*-glukoosia ( $^{18}\text{F}$ FDG) on kliinisessä käytössä useisiin tulehdukseen liittyvissä indikaatioissa, mutta vaikka  $^{18}\text{F}$ FDG:n kudoksikertymä onkin kohonnut tulehtuneissa kudoksissa, merkkiaine ei ole spesifinen tulehdukselle. Tämä voi johtaa vaikeuksiin kuvien analyysissä sekä mahdollisesti vääriin positiivisiin tuloksiin. Siksi vaihtoehtoisten, tulehdukselle spesifisten PET-radiolääkeaineiden kehittäminen on perusteltua.

Tavoitteena on kehittää ja arvioida uusia radiolääkeaineita tulehdukselle spesifisten kohteiden kuvantamiseen. Uudet diagnostiset työkalut voivat tulevaisuudessa olla arvokkaita tulehduksellisten tautien, kuten ateroskleroosin ja nivelreuman lääketieteellisessä tutkimuksessa. Tätä tarkoitusta varten on valittu kolme kohdemolekyyliä tulehduksen kuvantamiseksi: verisuonen pinnan tartuntamolekyyli-1 (VAP-1), folaattireseptori  $\beta$  (FR- $\beta$ ) ja yleinen lymfaattisen endoteelin ja verisuonten endoteelin reseptori-1 (CLEVER-1). Reseptorit liittyvät valkosolujen siirtymiseen tulehtuneisiin kudoksiin sekä aktivoituneisiin makrofageihin. Viittä erilaista, näihin reseptoreihin sitoutuvaa radiomerkkiainetta tutkittiin joko kokeellisissa tulehduksen tautimalleissa tai ihmisissä.

Tulokset osoittivat, että VAP-1:een kohdistuvat merkkiaineet  $^{68}\text{Ga}$ Ga- ja  $^{18}\text{F}$ AIF-NOTA-Siglec-9 pystyivät visualisoimaan steriilin ihotulehduksen rotissa ja merkkiaineiden kudoksikertymät olivat keskenään samankaltaiset. Toisen Siglec-9-peptidiin perustuvan merkkiaineen,  $^{68}\text{Ga}$ Ga-DOTA-Siglec-9:n osoitettiin olevan turvallinen ja hyvin siedetty terveissä vapaaehtoisissa, ja merkkiaine havaitsi tulehduksen reumapotilaan nivelissä. Lisäksi  $^{68}\text{Ga}$ Ga-NOTA-Folate-merkkiainetta käytettiin onnistuneesti FR- $\beta$ -positiivisten makrofagien kuvantamiseen hiirien tulehtuneissa ateroskleroottisissa leesioissa. Lopuksi  $^{89}\text{Zr}$ Zr-DFO-bexmarilimab havaitsi kohonneen CLEVER-1-expression kanin fibroottisissa munuaisissa.

Yhteenvedona voidaan todeta, että väitöskirjatutkimuksessa kehitetyt merkkiaineet pystyivät kuvantamaan kohdemolekyyliensä elävässä kohteessa.

AVAINSANAT: CLEVER-1, fluori-18, folaattireseptori  $\beta$ , gallium-68, PET, tulehdus, radiometallinen leimaus, VAP-1, zirkonium-89.

# Table of Contents

<b>Abbreviations .....</b>	<b>8</b>
<b>List of Original Publications .....</b>	<b>10</b>
<b>1 Introduction .....</b>	<b>11</b>
<b>2 Review of the Literature .....</b>	<b>13</b>
2.1 Positron emission tomography .....	13
2.2 Radiochemistry in PET .....	15
2.3 Radiometallic labelling .....	18
2.3.1 Radiolabelling with gallium-68 .....	20
2.3.2 Radiolabelling with aluminium-fluoride-18 .....	25
2.3.3 Radiolabelling with zirconium-89 .....	28
2.4 PET imaging of inflammation .....	33
2.4.1 Vascular adhesion protein-1 .....	38
2.4.2 Folate receptor beta .....	40
2.4.3 Common lymphatic endothelial and vascular endothelial receptor-1.....	42
<b>3 Aims .....</b>	<b>44</b>
<b>4 Materials and Methods .....</b>	<b>45</b>
4.1 Tracer radiolabelling and characterization .....	46
4.1.1 <sup>68</sup> Ga-NOTA-Siglec-9.....	47
4.1.2 Al <sup>18</sup> F-NOTA-Siglec-9 .....	47
4.1.3 <sup>68</sup> Ga-DOTA-Siglec-9 (GMP) .....	48
4.1.4 <sup>68</sup> Ga-NOTA-Folate .....	48
4.1.5 <sup>89</sup> Zr-DFO-bexmarilimab .....	50
4.2 Radiometabolite analysis .....	51
4.3 Preclinical disease models .....	53
4.4 Clinical research subjects.....	54
4.5 PET study design .....	54
4.5.1 PET study of sterile skin inflammation in rats .....	55
4.5.2 First-in-man PET study of <sup>68</sup> Ga-DOTA-Siglec-9.....	55
4.5.3 PET study of atherosclerosis in mice.....	57
4.5.4 PET study of renal fibrosis in rabbits .....	58
4.6 Radiation dosimetry .....	60



<b>5</b>	<b>Results</b> .....	<b>61</b>
5.1	Radiolabelling and tracer characterization .....	61
5.2	Preclinical evaluation of <sup>68</sup> Ga- and Al <sup>18</sup> F-NOTA-Siglec-9 .....	63
	5.2.1 <i>In vivo</i> PET imaging.....	63
	5.2.2 <i>Ex vivo</i> biodistribution.....	63
5.3	Clinical evaluation of <sup>68</sup> Ga-DOTA-Siglec-9.....	65
	5.3.1 Safety and tolerability .....	65
	5.3.2 Radioactivity distribution and radiation dose .....	65
	5.3.3 Assessment of rheumatoid arthritis.....	66
	5.3.4 Metabolism and pharmacokinetics.....	66
5.4	Preclinical evaluation of <sup>68</sup> Ga-NOTA-Folate.....	68
	5.4.1 Assessment of atherosclerotic lesions .....	68
	5.4.2 <i>Ex vivo</i> biodistribution in mice.....	68
	5.4.3 <i>In vivo</i> distribution kinetics and dosimetry in rats .....	68
	5.4.4 <i>In vitro</i> binding affinity to FR-β .....	70
5.5	Preclinical evaluation of <sup>89</sup> Zr-DFO-bexmarilimab .....	70
	5.5.1 Characterisation of the rabbit UUO model .....	70
	5.5.2 <i>In vivo</i> stability and pharmacokinetics.....	71
	5.5.3 <i>In vivo</i> PET/CT imaging.....	72
	5.5.4 <i>Ex vivo</i> biodistribution and autoradiography.....	74
	5.5.5 Estimation of human dosimetry.....	75
<b>6</b>	<b>Discussion</b> .....	<b>76</b>
6.1	<sup>68</sup> Ga- and Al <sup>18</sup> F-NOTA-Siglec-9 in skin inflammation .....	76
6.2	First-in-man study of <sup>68</sup> Ga-DOTA-Siglec-9.....	77
6.3	<sup>68</sup> Ga-NOTA-Folate visualizes atherosclerotic plaques .....	78
6.4	Increased <sup>89</sup> Zr-DFO-bexmarilimab uptake in renal fibrosis.....	80
6.5	General study limitations .....	81
<b>7</b>	<b>Conclusions</b> .....	<b>83</b>
	<b>Acknowledgements</b> .....	<b>84</b>
	<b>References</b> .....	<b>87</b>
	<b>Supplementary material</b> .....	<b>103</b>
	<b>Original Publications</b> .....	<b>107</b>

# Abbreviations

28H1	Anti-FAP antibody
2-AMPPA-HB	2-aminomethylpiperidine-N,N'-diacetic acid-N'- <i>o</i> -hydroxybenzyl
anti-MMR-Nb	Anti-mannose receptor nanobody
AOC3	Amine oxidase, copper containing-3
APC	Allophycocyanin
ApoB <sup>100/100</sup>	Homozygous genotype expressing only apolipoprotein B100
BFC	Bifunctional chelator
CCR1	C-C motif chemokine receptor 2
CHO-FR <sup>-</sup>	Folate receptor-negative chinese hamster ovary cells
CHO-FR <sup>+</sup>	Folate receptor-positive chinese hamster ovary cells
CLEVER-1	Common lymphatic endothelial and vascular endothelial receptor
CN	Coordination number
CRiG	Complement receptor of the immunoglobulin family
CT	Computed tomography
CXCR4	C-X-X motif chemokine receptor 4
DFO	Desferrioxamine, also known as deferoxamine
DFO*	Octadentate desferrioxamine-analog
DFOcyclo*	DFO modified with a cyclic hydroxamate group
DFO-Gal3-F(ab') <sub>2</sub>	DFO-conjugated anti-galectin-3 F(ab') <sub>2</sub> antibody fragment
DFO-pPhe-NCS	p-phenylenediisothiocyanate-DFO (also knowns as p-DFO-Bz-NCS)
DFO-sqOEt	DFO-squaramide ester
DMSO	Dimethyl sulfoxide
DOTA	1,4,7,10-tetraazacyclododecane-1,4,7,10-tetraacetic acid
ECL1i	Extracellular loop-1 inverso
F(ab)	Antigen binding fragment
F(ab') <sub>2</sub>	Two antigen-binding F(ab) portions linked by disulfide bonds
FACS	Fluorescence assisted cell sorting
FAP	Fibroblast activation protein
FAPI	Fibroblast activation protein inhibitor
FDG	2-fluoro-2-deoxy- <i>D</i> -glucose
FET	Fluoroethyltriazole
FITC	Fluorescein isothiocyanate
FMCH	Fluoromethylcholine
FR-β	Folate receptor beta
FSC	Fusarinine C
GAL-3	Galectin-3
GMP	Good manufacturing practice
H&E	Hematoxylin and eosin

HBED-CC	N,N'-bis[2-hydroxy-5-(carboxyethyl)benzyl] ethylenediamine-N,N'-diacetic acid
HEPES	4-(2-hydroxyethyl)-1-piperazineethanesulfonic acid
HER-2	Human epidermal growth factor receptor-2
HOPO	Hydroxypyridone
HPLC	High-performance liquid chromatography
IgG	Immunoglobulin
iTLC	Instant thin layer chromatography
LDLR <sup>-/-</sup>	Homozygous low density lipoprotein knockout genotype
mAb	Monoclonal antibody
Mal-HSA	Maleylated human serum albumin
MI	Myocardial infarction
MRI	Magnetic resonance imaging
MSA	Mannosylated human serum albumin
NaOAc	Sodium acetate
NHS	N-hydroxysuccinimide
NODA	1,4,7-triazacyclononane-1,4-diacetic acid
NODAGA	1,4,7-triazacyclononane,1-glutaric acid-4,7-acetic acid
NOTA	1,4,7-triazacyclononane-1,4,7-triacetic acid
NOTA-OC	NOTA-Octreotide
PBS	Phosphate-buffered saline
p-DFO-Bz-NCS	p-Isothiocyanatobenzyl-desferoxiamine (also known as DFO-pPhe-NCS)
PEG	polyethylene glycol
PET	Positron emission tomography
PSMA	Prostate specific membrane antigen
RCP	Radiochemical purity
RCY	Decay-corrected radiochemical yield
RECSA	Restrained complexing agent
SAX	Strong anion exchange
scFv	Single-chain variable fragment
SCX	Strong cation exchange
SDS-PAGE	Sodium dodecyl sulphate polyacrylamide gel electrophoresis
Siglec-9	Sialic acid-binding immunoglobulin-like lectin 9
SPECT	Single photon emission computed tomography
SR-A1	Class A1 scavenger receptor
SSA	Somatostatin analogue
STABILIN-1	A protein encoded by the STAB1 gene
sVAP	Soluble VAP-1
TACN	1,4,7-triazacyclonone
TFA	Trifluoroacetic acid
TOC	Tyr <sup>3</sup> octreotide
TOCA	Tyr <sup>3</sup> octreotide analog
TRAP	Triazacyclononane-phosphinic acid chelator
TSPO	18 kDa translocator protein
UUO	Unilateral ureteral obstruction
VAP-1	Vascular adhesion protein-1
βAG	Beta-alanine-glycine linker

# List of Original Publications

This dissertation is based on the following original publications, which are referred to in the text by their Roman numerals:

- I **Olli Moisio**, Riikka Siitonen, Heidi Liljenbäck, Elli Suomela, Sirpa Jalkanen, Xiang-Guo Li, Anne Roivainen. Exploring Alternative Radiolabeling Strategies for Sialic Acid-Binding Immunoglobulin-Like Lectin 9 Peptide: [<sup>68</sup>Ga]Ga- and [<sup>18</sup>F]AlF-NOTA-Siglec-9. *Molecules*, 2018; 23 (2): 305.
- II Riikka Viitanen, **Olli Moisio**, Petteri Lankinen, Xiang-Guo Li, Mikko Koivumäki, Sami Suilamo, Tuula Tolvanen, Kirsi Taimen, Markku Mali, Ia Kohonen, Ilpo Koskivirta, Vesa Oikonen, Helena Virtanen, Kristiina Santalahti, Anu Autio, Antti Saraste, Laura Pirilä, Pirjo Nuutila, Juhani Knuuti, Sirpa Jalkanen, Anne Roivainen. First-in-Humans Study of <sup>68</sup>Ga-DOTA-Siglec-9, a PET Ligand Targeting Vascular Adhesion Protein 1. *Journal of Nuclear Medicine*, 2021; 62 (4): 577-583.
- III **Olli Moisio\***, Senthil Palani\*, Jenni Virta, Petri Elo, Heidi Liljenbäck, Tuula Tolvanen, Meeri Käkelä, Maxwell G. Miner, Erika Atencio Herre, Päivi Marjamäki, Tiit Örd, Merja Heinäniemi, Minna U. Kaikkonen, Fengyun Zhang, Madduri Srinivasarao, Juhani Knuuti, Philip S. Low, Antti Saraste, Xiang-Guo Li, Anne Roivainen. Radiosynthesis and preclinical evaluation of [<sup>68</sup>Ga]Ga-NOTA-folate for PET imaging of folate receptor β-positive macrophages. *Scientific Reports*, 2020; 10 (1): 13593.
- IV **Olli Moisio**, Jenni Virta, Emrah Yarkin, Heidi Liljenbäck, Senthil Palani, Riikka Viitanen, Maxwell G. Miner, Vesa Oikonen, Tuula Tolvanen, Danielle J. Vugts, Pekka Taimen, Xiang-Guo Li, Maija Hollmen, Sirpa Jalkanen, Anne Roivainen. Preclinical Evaluation of a Humanized Antibody Against Common Lymphatic Endothelial and Vascular Endothelial Receptor-1, <sup>89</sup>Zr-Desferrioxamine-Bexmarilimab, in a Rabbit Model of Renal Fibrosis. *Journal of Nuclear Medicine*, 2022; Published ahead of print: jnumed.122.264725.

The original publications have been reproduced with the permission of the copyright holders. \*Equal contribution.

# 1 Introduction

Positron emission tomography (PET) is a molecular imaging technique that generates functional physiological data at the molecular level, allowing physicians and researchers to follow and quantify biological processes non-invasively in living subjects. PET can diversely visualize blood flow, metabolic function, receptor density and other molecular pathways in both patients and experimental animals. Not only useful for clinical diagnostics, it's also an increasingly useful tool for basic research of physiological and molecular processes (Lancelot & Zimmer, 2010), as well as drug development and discovery (Donnelly, 2020). The broad functionality of PET is achieved via external, sensitive detection of intravenously injected or inhaled radiopharmaceuticals, also known as radiotracers or radioligands.

In the research area of inflammation, the radiotracer fluorine 18 ( $^{18}\text{F}$ ) labelled 2-deoxy-2-fluoro-*D*-glucose ( $[^{18}\text{F}]\text{FDG}$ ) has been employed in clinic for several indications involving inflammation, including atherosclerosis (J. H. F. Rudd et al., 2002), rheumatoid arthritis (Beckers et al., 2004) and certain infections (Alavi & Werner, 2017). Ongoing inflammatory response generates an increase in glucose metabolism, which is readily targeted by  $[^{18}\text{F}]\text{FDG}$ . Uptake of  $[^{18}\text{F}]\text{FDG}$  is however not specific to inflammation, and it cannot distinguish between other metabolically active cells which can lead to false positive findings. Further, high physiological uptake in the myocardium and brain can lead to difficulties in analysis (Pijl et al., 2021). Therefore, development of alternative radiotracers that target molecular processes more strongly correlated with inflammation is needed.

With this in mind, three well-established biological targets related to inflammation and immune response were selected for this study: vascular adhesion protein-1 (VAP-1), folate receptor beta (FR- $\beta$ ) and common lymphatic endothelial and vascular endothelial receptor-1 (CLEVER-1). These receptors are associated with leukocyte recruitment into inflamed tissues (Salmi & Jalkanen, 2019), activated macrophages in sites of inflammation (Xia et al., 2009), and immunosuppressive macrophages (Salmi et al., 2004), respectively. This thesis presents four studies (I-IV), which contain the radiosynthesis and *in vivo* evaluation of five different biomolecule-based radiopharmaceuticals that recognize their corresponding targets *in vivo* by PET imaging. The broad research topics of each study are outlined in Table 1.

**Table 1.** Details of the studies included in this thesis.

	<b>Radiopharmaceutical</b>	<b>Biological target</b>	<b><i>In vivo</i> evaluation</b>
Study I	<sup>68</sup> Ga-NOTA-Siglec-9 Al <sup>18</sup> F-NOTA-Siglec-9	VAP-1, leukocyte transmigration	Sterile skin inflammation in Sprague Dawley rats
Study II	<sup>68</sup> Ga-DOTA-Siglec-9	VAP-1, leukocyte transmigration	Safety study in healthy men, rheumatoid arthritis
Study III	<sup>68</sup> Ga-NOTA-Folate	FR-β, activated macrophages	Atherosclerotic plaques in LDLR <sup>-/-</sup> ApoB <sup>100/100</sup> mice
Study IV	<sup>89</sup> Zr-DFO-bexmarilimab	CLEVER-1, alternatively activated macrophages	Renal fibrosis in New Zealand White rabbits

The radiosynthetic strategies used to produce the radiotracers included in this work focus on radiometallic labelling, an increasingly relevant subset of radiochemistry especially used for labelling biomolecules (Jackson et al., 2020). The “pseudo-radiometallic” aluminium [<sup>18</sup>F]fluoride labeling method (Archibald & Allott, 2021) used in Study I provides an exemption to this theme. As a disclaimer, contrary to strict nomenclature, the bracketed notation of radionuclide content in radiotracer naming has been simplified for the table of contents and other presented tables to improve readability (e.g. [<sup>68</sup>Ga]Ga-DOTA is shortened to <sup>68</sup>Ga-DOTA)."

In the following chapter, a literature review is presented with a focus on the radiosynthetic strategies related to each study. Subsequently, brief reviews on current development of PET radiopharmaceuticals for imaging inflammatory conditions, as well as the three inflammation-related targets pursued in studies I-IV are included.

## 2 Review of the Literature

### 2.1 Positron emission tomography

The molecular imaging functionality of PET is realized via external, sensitive detection of radiotracers labelled with positron-emitting radionuclides. The radionuclides are introduced on the structure of a molecule, also often known as a ligand, that can selectively target specific cellular receptors or metabolic pathways in patients or research animals. When administered to the subject of study, the radioligand is distributed throughout the body and accumulates in certain tissues based on its specific biological and chemical properties. Accurate spatial detection of this accumulation is then achieved by appropriate utilization of the properties of positron emission. Upon decay of the parent nuclide, the generated positron travels for a short distance, losing energy in interactions with surrounding material until it finally collides with an electron. The two particles undergo annihilation, producing two gamma photons with the energy of 511 keV in accordance with the mass-energy equivalence depicted by Einstein's formula,  $E = mc^2$ . Convenient for PET, the photons are emitted in exactly opposite directions following the conservation of momentum. These photons are then coincidentally detected on opposing sides of a scintillator detector array surrounding the study subject (Figure 1).

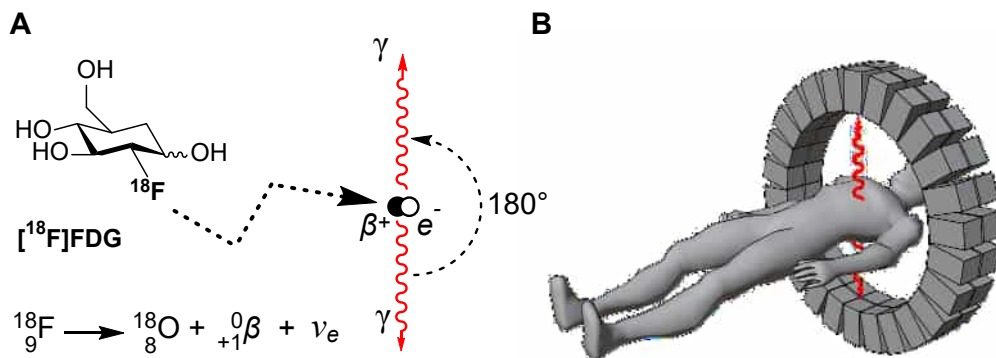


**Figure 1.** (A) After its generation from the decay of the fluorine-18 isotope in  $[^{18}\text{F}]\text{FDG}$ , a positron collides with electron producing two opposing 511 keV gamma photons, (B) which are coincidentally detected by a PET scanner detector array surrounding the patient.

By exploiting this so-called coincidence detection, PET significantly improves spatial resolution and sensitivity compared to the detection of individual gamma quants in single-photon emission computed tomography (SPECT) (Khalil et al., 2011).

## Multimodal imaging

On its own, PET provides molecular or functional information without a direct anatomical reference. Current standard practice in both clinical and preclinical imaging is the combined use of PET and computed tomography (PET/CT). When registered consecutively, CT provides anatomic context to PET, allowing for accurate determination of anatomical regions of interest (ROI), improving quantitative accuracy and diagnostic interpretation of PET images (Blodgett et al., 2007; Pichler et al., 2008). Another advantage of using PET/CT is attenuation correction. A significant fraction of gamma photons emitted from positron annihilation are naturally absorbed by surrounding tissue. This effect naturally reduces, or attenuates, the amount of detectable coincidence events. The magnitude of effect is dependent on tissue density and the anatomical depth at which the photons are generated. Density data provided by CT can be used to correct for this effect (Burger et al., 2002).

Alongside PET/CT, PET has been successfully combined with magnetic resonance imaging (MRI) (Judenhofer et al., 2008). PET/MRI provides better anatomical information of soft tissues, which is a distinct disadvantage of CT. Additionally, MRI allows simultaneous data collection in parallel with PET, which can be used to correct PET data for respiratory and cardiac motion (Munoz et al., 2021). Nevertheless, while the prevalence of PET/MRI is steadily increasing, PET/CT remains the primary hybrid imaging technique.

**Table 2.** Characteristic of PET and related imaging modalities.

Modality	Nature of information	Spatial resolution	References
PET	Functional and molecular	Clinical 4-6 mm Preclinical 1-2 mm	(Herschman, 2003; Muehlechner & Karp, 2006)
SPECT	Functional and molecular	Clinical 8-12 mm Preclinical < 1 mm	(Khalil et al., 2011; van Have et al., 2009)
CT	Anatomical	15-50 $\mu$ m	(Withers et al., 2021)
MRI	Anatomical, functional and molecular	~ 1 mm	(Grover et al., 2015)



## 2.2 Radiochemistry in PET

In PET, radiochemistry encompasses both the production, separation and purification of radionuclides and the radiolabeling methods used to incorporate those nuclides into the final radiotracer structure, as well as the harmonization of related nomenclature. (Coenen et al., 2017; Herth et al., 2021). The broad-ranging molecular imaging potential of PET is achieved by a diverse selection of radiopharmaceuticals ranging from classical small molecules (Vāvere & Scott, 2017) to peptides (Fani & Maecke, 2012; Reubi & Maecke, 2008), antibodies (Wei et al., 2020) and nanoparticles (Lamb & Holland, 2018).

**Table 3.** Physical properties of commonly used PET radionuclides (Conti & Eriksson, 2016; Laboratoire National Henri Becquerel).

Radionuclide	$t_{1/2}$	Branching ( $\beta^+$ , %)	$\beta^+$ decay product	$E_{\max}$ (MeV)	$R_{\text{mean}}$ (mm)	$R_{\max}$ (mm)
Carbon-11 ( $^{11}\text{C}$ )	20.4 min	99.8	$^{11}\text{B}$	0.96	1.2	4.2
Nitrogen-13 ( $^{13}\text{N}$ )	9.97 min	99.8	$^{13}\text{C}$	1.20	1.8	5.5
Oxygen-15 ( $^{15}\text{O}$ )	2.04 min	99.9	$^{15}\text{N}$	1.73	3.0	8.4
Fluorine-18 ( $^{18}\text{F}$ )	109.8 min	96.9	$^{18}\text{O}$	0.63	0.6	2.4
Copper-64 ( $^{64}\text{Cu}$ )	12.7 h	17.5	$^{64}\text{Ni}$	0.65	0.7	2.5
Gallium-68 ( $^{68}\text{Ga}$ )	67.8 min	88.9	$^{68}\text{Zn}$	1.90	3.5	9.2
Zirconium-89 ( $^{89}\text{Zr}$ )	78.4 h	22.7	$^{89}\text{Y}$	0.90	1.3	3.8
Iodine-124 ( $^{124}\text{I}$ )	100.1 h	11.7, 10.7	$^{124}\text{Te}$	1.54, 2.14	2.8, 4.4	7.1, 10.0

$E_{\max}$  = maximum positron energy,  $R_{\text{mean}}$  = mean positron range in water,  $R_{\max}$  = maximum positron range in water.

Demands of the physiological target, the molecular structure of the tracer as well as pharmacokinetic and diagnostic requirements all have an influence on the choice of radionuclide as well as the choice of radiolabelling methodology. As a general principle, the addition of the radionuclide should interfere with the biological properties of the ligand moiety of the tracer molecule as little as possible.

Commonly used PET radionuclides include carbon-11, nitrogen-13, oxygen-15, fluorine-18, gallium-68, copper-64, and zirconium-89 and iodine-124 as listed above in Table 3. For practicality, the physical half-life of the selected tracer should be long enough to allow sufficient time for production and purification of the radiopharmaceutical as well as imaging. Further, radioactive half-life should be in the

same range with biological half-life of the radioligand to allow for a sufficient imaging window while avoiding unnecessary radioactive dose to the patient. Likewise, the chemical structure and molecular inertness of the ligand molecule as well as the imaging target are among the factors to be considered in radiolabelling design. As an example, the complex and relatively large chemical structure of biomolecules such as peptides and antibodies typically do not allow for complex protecting- or leaving group strategies commonly required for classical covalent radiolabelling. In the following chapters, different radiolabelling strategies are briefly discussed with a special focus on radiometallic and chelation-based radiolabelling.

### Covalent versus radiometallic labelling strategies of biomolecules

The four standard covalently labelled radionuclides in PET include  $^{11}\text{C}$ ,  $^{13}\text{N}$ ,  $^{15}\text{O}$  and  $^{18}\text{F}$ . Typically, these nuclides are routinely produced in low-energy medical cyclotrons and covalently attached to the radiotracer molecule (Deng et al., 2019; Miller et al., 2008). With the exemption of  $^{18}\text{F}$ , these elements are abundant in biological organic molecules and natural isotopes of the same element can be replaced by the corresponding radioisotope without affecting biological function. In this regard,  $^{11}\text{C}$  has found broad use in PET, especially in imaging of neurological conditions (Goud et al., 2021). The use of  $^{13}\text{N}$  and  $^{15}\text{O}$  in PET has been mainly limited to functional imaging with  $[^{13}\text{N}]\text{NH}_3$  (Herzog et al., 2009),  $[^{15}\text{O}]\text{H}_2\text{O}$  (Fan et al., 2015) and  $[^{15}\text{O}]\text{O}_2$  (Fan et al., 2020), mainly because of their very short half-lives.

While the  $^{18}\text{F}$  isotope extremely rarely present in physiological molecules, resulting from its favourable properties for improving the biological behaviour of pharmaceutical molecules (Gillis et al., 2015; K. Müller et al., 2007) and the convenient half-life and low positron energy, it has become the workhorse radionuclide in PET. In the scope of biomolecules, especially peptides, several suitable labelling strategies have been developed. These include various prosthetic group strategies (Morris et al., 2019), fluoroglycosylation (Li et al., 2012; Namavari et al., 2009) and click-chemistry (J. P. Meyer et al., 2016; Figure 2 A). However, the chemical conditions required for  $^{18}\text{F}$ -labeling and the synthesis of required prosthetic groups often require the use of aprotic solvents and high temperatures, which can be problematic for relatively unstable biomolecule-based precursors and can lengthen synthesis time because of the necessary purification steps required. Indeed, despite rapid development of available synthesis strategies and superior imaging properties of the  $^{18}\text{F}$  radionuclide, covalent radiolabelling of peptides with  $^{18}\text{F}$  remains a challenge (Richter & Wuest, 2014).

Lead by the clinical success stories of  $^{68}\text{Ga}$ -labelled somatostatin analogues (SSAs)  $[^{68}\text{Ga}]\text{Ga-DOTA-NOC}$ ,  $[^{68}\text{Ga}]\text{Ga-DOTA-TOC}$ ,  $[^{68}\text{Ga}]\text{Ga-DOTA-TATE}$  (Fani et al., 2022) and  $^{68}\text{Ga}$ -labelled prostate specific antigen ligand  $[^{68}\text{Ga}]\text{Ga-PSMA}$  (Eiber et al., 2015), most peptides used in PET are labelled via radiometallic chelation, most

commonly with  $^{68}\text{Ga}$ . Radiometallic labelling allows for simple, often single step radiolabelling in mild, aqueous conditions that are well tolerated by biomolecules (Figure 2. B-C). Further, any resulting high-polarity impurities, typically unchelated radiometal, can be conveniently removed with simple cartridge purification.

In similar fashion, radiometallic labelling has become the primary radiolabelling strategy for monoclonal antibodies (mAbs), also known as immuno-PET. The long biological half-life of mAbs limits the viable radionuclides to the one's with longer physical half-lives, namely  $^{89}\text{Zr}$  ( $t_{1/2} = 78.4$  h) and  $^{124}\text{I}$  ( $t_{1/2} = 100$  h). Because of the favourable biological behaviour and radiosynthetic properties of the  $^{89}\text{Zr}$  radionuclide, it has recently gained favour over the covalently bound  $^{124}\text{I}$  (Yoon et al., 2020).

Various radiometallation strategies for biomolecules are reviewed in detail in Chapter 3.3: Radiometallic labelling, focusing on the radionuclides used in the studies included in this thesis:  $^{68}\text{Ga}$ ,  $^{18}\text{F}$  (in  $[\text{}^{18}\text{F}]\text{AlF}$ ) and  $^{89}\text{Zr}$ .

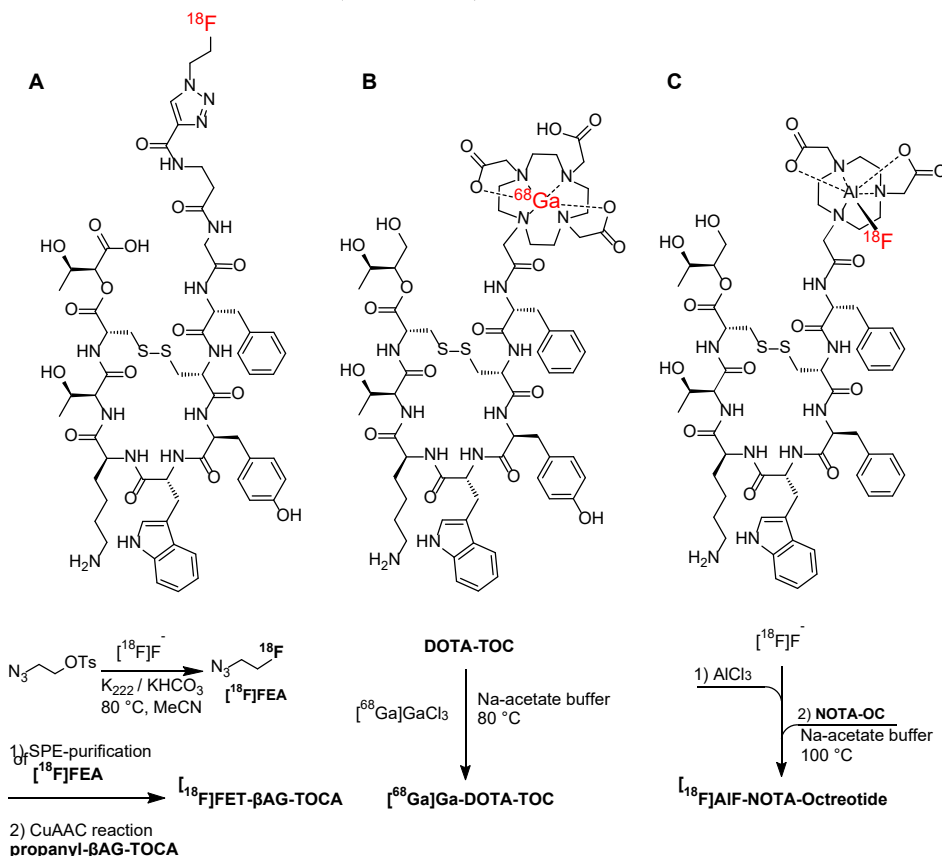


**Figure 2.** Examples of radiolabeled peptides in the somatostatin analogue (SSA) -group of radiopharmaceuticals, produced by **A**: covalent radiolabeling via click-chemistry (Allott et al., 2020), **B**: radiometallic labelling (Hofmann et al., 2001) and **C**: “pseudo-radiometallic” radiolabelling (Tshibangu et al., 2020).

## 2.3 Radiometallic labelling

Radiometallic labelling relies on coordination chemistry, where radiometal ions are non-covalently bound to electron-donating multidentate ligands, otherwise known as chelators (Dwyer & Mellor, 1964). In radiopharmaceuticals, the chelator is covalently attached to a targeting vector, often through a linker structure (Figure 3). For biomolecules, this typically requires the use of so-called bifunctional chelators (BFCs), which contain a chelating moiety and a reactive group capable of efficient covalent bond formation with corresponding functional groups on the targeting vector (Figure 4).

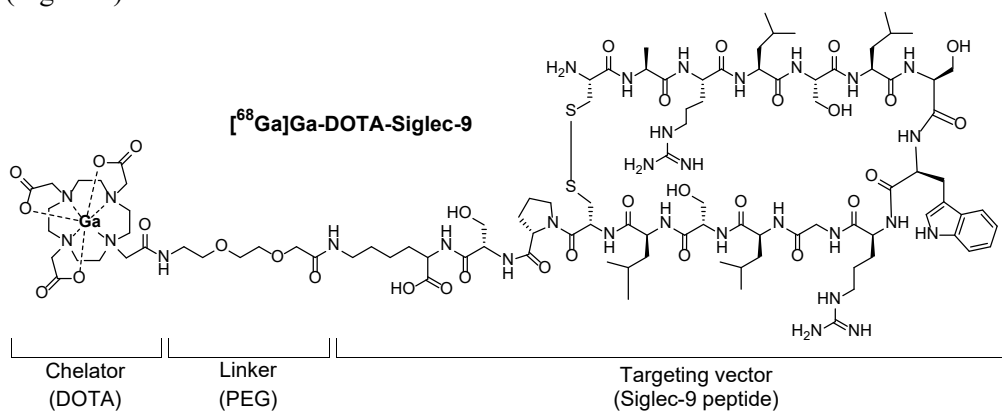


**Figure 3.** Chelator, linker and targeting vector structures presented on the radiotracer [<sup>68</sup>Ga]Ga-DOTA-Siglec-9 (Aalto et al., 2011).

Optimally, any purposefully selected chelator should cover some fundamental requirements: 1) The chelator should form stable and biologically inert complexes with the radionuclide, 2) Radiolabelling should be accessible at a temperature and pH suitable for the precursor molecule. 3) To achieve good specific activities in the presence of trace metals, the chelator should have some selectivity towards the required radiometal (Bartholomä, 2012; Price & Orvig, 2014). The secondary ability of the BFCs, the ability to conjugate to biomolecules also needs to be robust and biocompatible to allow for flexible attachment to the targeting biomolecule. Common bioconjugation techniques include functional groups such as N-hydroxysuccinimide-esters (NHS) and tetrafluorophenyl esters (TPS) for conjugating amines, isothiocyanates (NCS) for thiourea couplings and maleimides for thiol couplings (Bartholomä, 2012).

In general, the modular design of bifunctional chelators allows for theoretically boundless variation of different vectors to be chelated with different chelating agents. While options may be practically limitless, the choice of BFC can have a significant effect on radiotracer. Apart from having a clear impact on the radiolabelling chemistry,

changing the chelator can have a drastic impact on the biodistribution profile, even when the targeting vector structure remains identical (Blasi et al., 2014; Chomet et al., 2021; Y. S. Kim et al., 2008; Lin et al., 2013). It is also common that linker chemistry has an impact on pharmacokinetic properties of radiotracers. Changes in biodistribution can be manifested through changes in lipophilicity, receptor binding ability or metabolic stability of the radiotracer (Amouroux et al., 2015; Baranski et al., 2017; Kuo et al., 2018; Zhai et al., 2016).

The chelating moieties used in BFCs are broadly categorized into two types: macrocyclic and acyclic chelators. Regarding kinetic inertness of the radiometal coordination complex, macrocyclic chelators are generally more resistant to *in vivo* demetallation. The covalently constrained, relatively rigid cyclic structure of the macrocycle allows for pre-organized coordination sites, which in turn reduce entropic loss upon complex formation. This increased complex stability is called the “macrocyclic effect” (Melson, 1979). The downside to increased kinetic rigidity is that higher labelling temperatures and harsher reaction conditions are generally required for successful radiolabelling. Conversely, acyclic chelators are more kinetically labile, but allows radiolabelling in milder pH and in room temperature. Fast radiolabelling in mild conditions is crucial when labelling molecules that are sensitive to denaturing or aggregation. This is the case especially with monoclonal antibodies and their fragments.

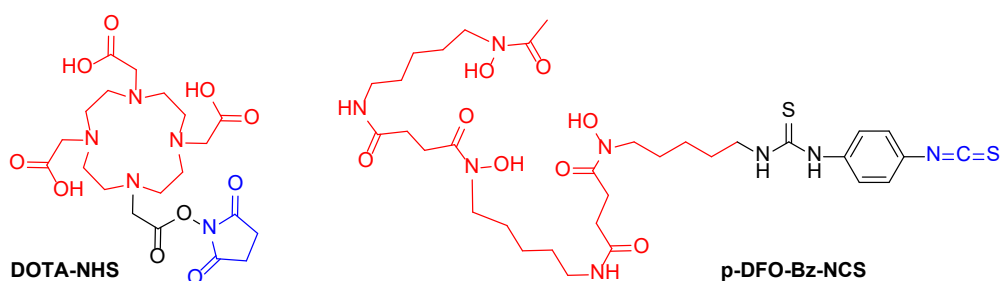


**Figure 4.** Examples of macrocyclic (DOTA) and acyclic (DFO) bifunctional chelators (BFCs) containing a chelating agent (red color) for radiometallation and a reactive moiety (blue color) for conjugation to a targeting vector.

For clarity, the chelators and BFCs presented in the upcoming chapters have been selected on the basis that they have been evaluated *in vivo* as BFC-biomolecule conjugates rather than as unconjugated chelators, unless otherwise stated.

### 2.3.1 Radiolabelling with gallium-68

The contribution of  $^{68}\text{Ga}$  to the development of the PET field can be considered significant (Velikyan, 2015).  $\text{Ga}^{68}$  has half-life of 67.8 minutes with mean and maximum positron energies of 0.84 and 1.9 MeV, respectively, resulting in a mean positron range of 1.05 mm in soft tissue (Sanchez-Crespo, 2013). In addition to convenient targeting ligand conjugation and radiolabelling through the BFC strategy, the appeal of  $^{68}\text{Ga}$ -labelled radiopharmaceuticals is often credited to the convenience and accessibility of  $^{68}\text{Ga}$  by using benchtop germanium-68/gallium68 ( $^{68}\text{Ge}/^{68}\text{Ga}$ )-generators. Further improving accessibility of  $^{68}\text{Ga}$ -PET, in the recent years there is a trend towards single-vial kit-based  $^{68}\text{Ga}$ -labelling. Existing commercial kits include SomaKit TOC<sup>®</sup> for [ $^{68}\text{Ga}$ ]Ga-DOTA-TOC and isoPROtrace11<sup>®</sup> and Illuccix<sup>®</sup> for [ $^{68}\text{Ga}$ ]Ga-PSMA-11 labelling and further efforts to develop novel “cold kits” for  $^{68}\text{Ga}$ -labelling are increasing (Lepareur, 2022).

#### Bifunctional chelators for $^{68}\text{Ga}$

The [ $^{68}\text{Ga}$ ]Ga<sup>3+</sup> ion has maximum coordination number of 6, and thus the most stable complexes with  $^{68}\text{Ga}$  are formed by hexadentate ligands. However, optimal denticity of the chosen is not always indicative of in vivo performance of the radiopharmaceutical. While 1,5,7-triazacyclononane (TACN)-based ligands are accepted as more stable and easier to radiolabel, the 1,4,7,10-tetraazacyclododecane-based, heptadentate (N<sub>4</sub>O<sub>3</sub>, CN 8) DOTA-chelator remains the prominent chelator seen in clinical  $^{68}\text{Ga}$ -radiopharmaceuticals (Breeman et al., 2011). Likewise, while pentadentate NOTA (N<sub>3</sub>O<sub>2</sub>, CN 5) is theoretically inferior to its hexadentate (N<sub>3</sub>O<sub>3</sub>, CN 6) cousin NODAGA, it can be seen in many radiotracers reaching clinical trials (Ebenhan et al., 2018; Skovgaard et al., 2017; Vilche et al., 2019; Wang et al., 2015). Interestingly, although NOTA is often stated as being strictly pentadentate, X-ray diffraction studies have shown coordination bond formation with either the amide nitrogen or amide oxygen on the amide-conjugated arm, depending on labelling pH, making the structure hexadentate (Figure 5, Shetty et al., 2010).

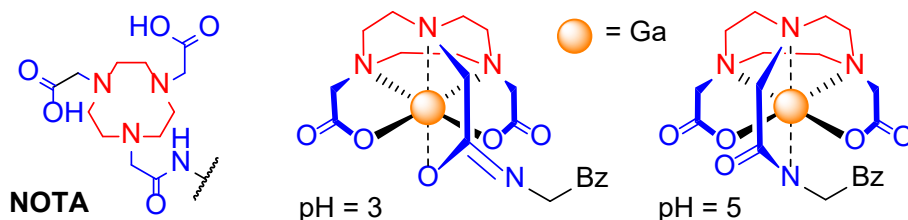


**Figure 5.** Hexadentate coordination of monoamine-conjugated Ga-NOTA-complexes formed at different reaction pH. Drawn based on X-ray crystal structures presented by Shetty et al.

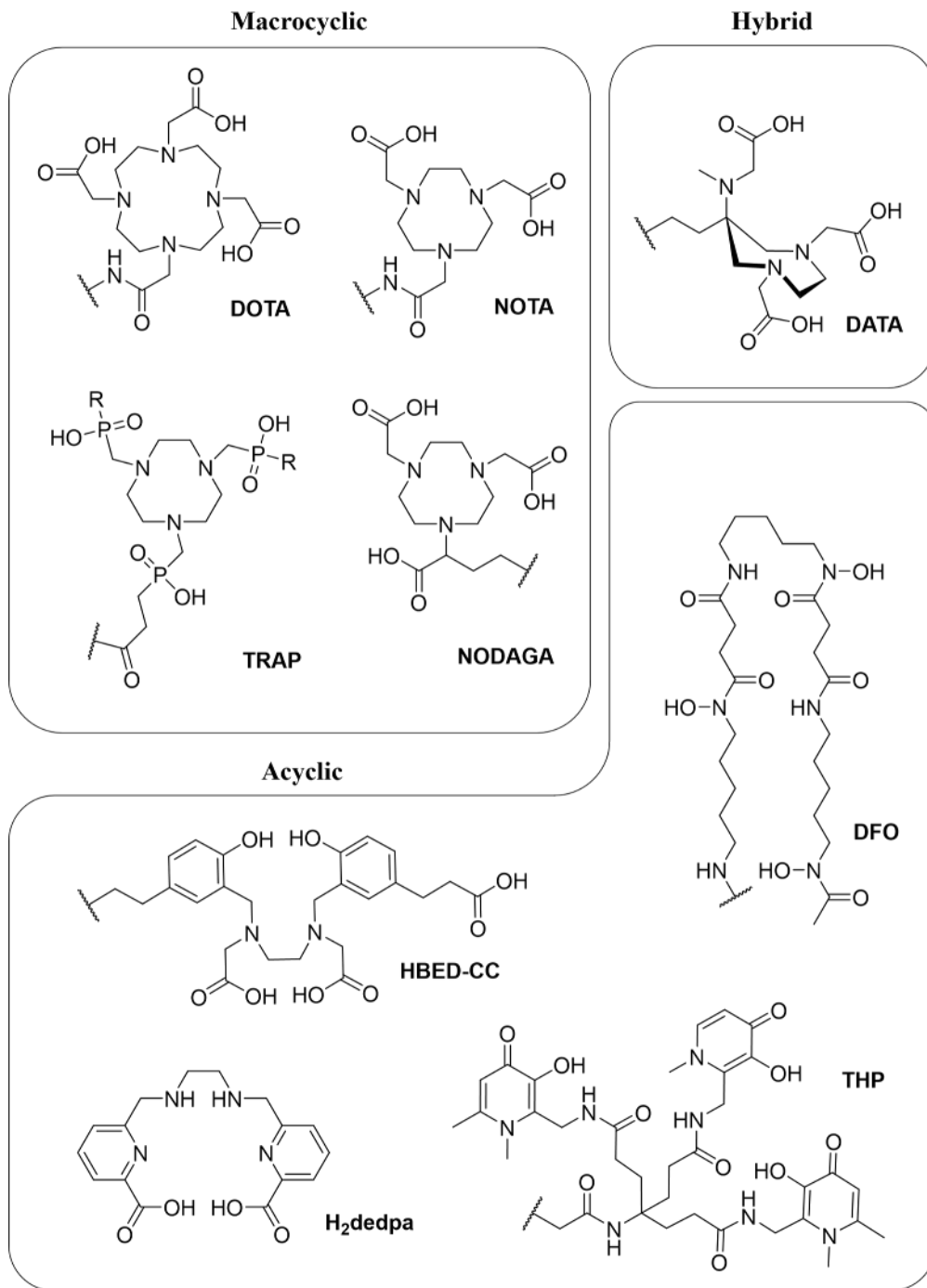


**Figure 6.** Examples of macrocyclic, acyclic and “hybrid” bifunctional chelators used in  $^{68}\text{Ga}$  labelled bioconjugates.

In the group of macrocyclic chelators, exceptional molar activities have been reached with triazacyclononane-phosphinate chelators (TRAP). Due to greatly increased selectivity towards gallium, extremely high molar activities of up to 5000 GBq/ $\mu\text{mol}$  were achieved with TRAP-(RGD)<sub>3</sub> peptide conjugates (Notni et al., 2011). It should be noted however, that increased molar activity does not necessarily lead to better contrast or target-to-background ratios in images (Šimeček et al., 2014). A radiotracer based on the TRAP-framework, [<sup>68</sup>Ga]Ga-Trivehexin has also shown promise in targeting integrin  $\alpha_v\beta_6$  in human trials (Quigley et al., 2022).

The “gold standard” of acyclic chelators of <sup>68</sup>Ga is HBED-CC (N,N'-bis [2-hydroxy-5-(carboxyethyl)benzyl] ethylenediamine-N,N'-diacetic acid), as seen in [<sup>68</sup>Ga]-PSMA-11 (Eder et al., 2014). The *in vivo* behaviour <sup>68</sup>Ga-PSMA-11 highlights the importance of observing the BFC-tracer conjugate as a complete unit: the aromatic moieties on HBED-CC improve the internalization and tumour uptake of the tracer conjugate, while simultaneously binding <sup>68</sup>Ga (Hennrich & Eder, 2021).

Acyclic hexadentate chelator desferrioxamine (DFO) has been conjugated to various peptides and evaluated preclinically with good *in vivo* results. Not surprisingly, <sup>68</sup>Ga-labelled DFO-PSMA showed lower tumour uptake compared to [<sup>68</sup>Ga]Ga-PSMA-11, as DFO does not impart the lipophilic and aromatic interactions that were found to improve PSMA internalization previously (Gourni et al., 2017). However, <sup>68</sup>Ga chelates of DFO have seen more promising *in vivo* results as a BFC in immuno-PET in labelling nanobodies, affibodies and single-chain variable fragments (scFv) (Rinne et al., 2021; Ueda et al., 2015; Vosjan et al., 2011). However, some concerns about the stability of the <sup>68</sup>Ga-DFO complex stability have been raised (Vosjan et al., 2011).

Another chelator imparting lipophilicity through aromatic moieties is the chelator H<sub>2</sub>dedpa (1,2-[[6-carboxypyridin-2-yl]methylamino]-ethane, (Boros et al., 2010) and variants, most prominently H<sub>2</sub>hox (1,2-[[6-hydroxyquinoline-2-yl]methylamino]-ethane, (X. Wang et al., 2019). While <sup>68</sup>Ga-chelating reported properties have been good, *in vivo* studies of this chelator conjugated to biomolecules in are few and with mixed result (Boros et al., 2012) so their performance as BFCs is yet to be proven.

Lastly, the acyclic THP-chelator (Tris(hydroxypyridinone)) and “hybrid” DATA chelator containing both cyclic and acyclic sections have been targets of interest particularly for their ability bind <sup>68</sup>Ga very quickly in room temperature and neutral pH. This results in excellent potential for “cold kit” labelling (Hofman et al., 2017; Sinnes et al., 2019). Notably, [<sup>68</sup>Ga]Ga-THP-PSMA was shown to have equivalent imaging performance to [<sup>68</sup>Ga]Ga-PSMA-HBED-CC while allowing for faster radiolabelling in milder conditions (Young et al., 2017). Like DFO, THP has shown some promise in scFv labelling with good coordination complex stability (Nawaz et al., 2017). While broader *in vivo* application of THP is still somewhat lacking, it may



prove to be a good option for labelling fragile ligands as well as in cases where an increase in lipophilicity is desirable.

### Production of $^{68}\text{Ga}$ for labelling

For  $^{68}\text{Ge}/^{68}\text{Ga}$  generators,  $^{68}\text{Ge}$  is produced from stable  $^{69}\text{Ga}$  through the nuclear reaction  $^{69}\text{Ga}(p, 2n)^{68}\text{Ge}$  in a high energy cyclotron. The produced  $^{68}\text{Ge}$  ( $t_{1/2} = 270.95$  d) is loaded on a solid support in a simple chromatographic borosilicate glass column within a self-contained, lead shielded benchtop device. The parent radionuclide ( $^{68}\text{Ge}$ ) decays into  $^{68}\text{Ga}$ , which can be selectively eluted from the column while  $^{68}\text{Ge}$  remains adsorbed to the solid support. This typically using a mildly acidic hydrochloric acid (HCl) eluent. The  $^{68}\text{Ga}$ -radioactivity contained in the generator follows secular equilibrium, where the maximum quantity of  $^{68}\text{Ga}$  activity is reached at a point where the decay rate of the daughter,  $^{68}\text{Ga}$ , matches the decay rate of the parent nuclide,  $^{68}\text{Ge}$  (IUPAC, *Compendium of Chemical Terminology*, 1997). In practical terms, > 91% of maximum available  $^{68}\text{Ga}$  radioactivity is recovered 4 hours from previous elution, allowing for multiple on-demand elutions on any given day.

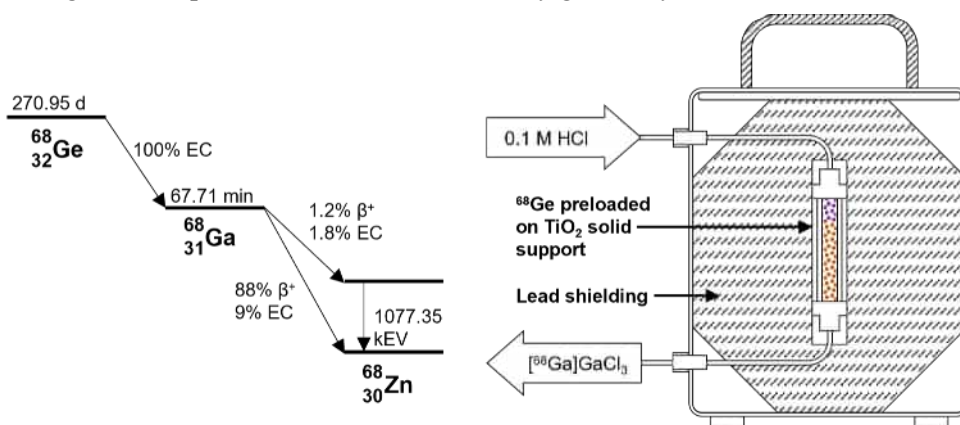


**Figure 7.** A decay scheme of the  $^{68}\text{Ge}/^{68}\text{Ga}$  system and an illustrative schematic of a conventional solid support  $^{68}\text{Ge}/^{68}\text{Ga}$  generator.

At present, several commercial  $^{68}\text{Ga}/^{68}\text{Ge}$  are readily available for preclinical research and clinical use, with many adhering to good manufacturing practice (GMP) principles. These include  $\text{TiO}_2$ -based GalliaPharm® (GMP) and IGG100® (non-GMP) from Eckert & Ziegler (Berlin, Germany), GalliAd® (GMP) from IRE Elit (Fleurus, Belgium) and the dodecyl gallate-modified  $\text{SiO}_2$ -based GeGant-generator (GMP) from ITG (Garching, Germany). Eluates from these generators can be used as is without processing, but the eluate can be purified or concentrated if necessary.

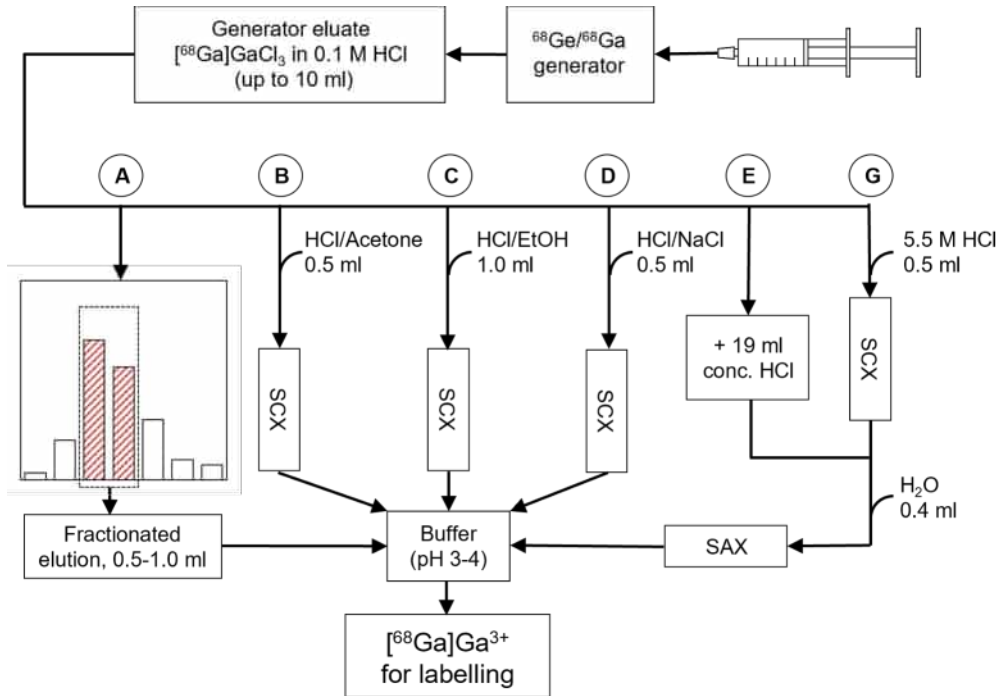


**Figure 8.** Scheme of current  $^{68}\text{Ge}/^{68}\text{Ga}$  generator eluate processing methods (A-F, Mueller et al., 2012, 2016). The eluate can be used for labelling by **A**: using the highest activity fractions from the complete eluate. Other options include pre-concentration with a strong cation exchange (SCX) resin eluted with **B**: 0.4% 0.05M HCl in acetone, **C**: 10% 0.9N HCl in Ethanol or **D**: 0.13 M HCl, 5 M NaCl in  $\text{H}_2\text{O}$ . Finally, a strong anion exchange (SAX) resin can be eluted with water after conversion to  $^{68}\text{GaCl}_4^-$  with **E**: concentrated HCl or **F**: an inline SCX column.

Various viable options for eluate pre-concentration have been proposed, as shown in Figure 8A a common and simple option is to use one or more fractions containing most of the eluted radioactivity. If pre-concentration is desired, several methods have been presented. These can be roughly divided into methods using strong cation exchange (Figure 8B-D, Baranski et al., 2017; Eppard et al., 2014; Mueller et al., 2016) and Strong anion exchange (Figure 8E., G. J. Meyer et al., 2004) or a combination of both (Figure 8G, Loktionova et al., 2011). It should be noted that with modern generators,  $^{68}\text{Ge}$ -breakthrough should remain very low throughout generator lifetime (Velikyan, 2015), and these methods are not strictly necessary for the sake of reducing impurities. Nevertheless, different pre-concentration methods have an undeniable effect on total radioactivity yield, purity and molar activity reached in radiolabelling (Seemann et al., 2015).

Equally, the choice of labelling buffer has an impact on labelling success. Typically, the buffering system is based on HEPES- (4-(2-hydroxyethyl)-1-

piperazineethanesulfonic acid) or sodium acetate (Velikyan, 2015). HEPES acts as weak complexing agent that imparts some protection against the formation of gallium hydroxides (Martins et al., 2013) and is preferred for its ability to produce higher molar activities, while the acetate buffer system can be a better option due to regulatory restraints on HEPES content in formulations for human use (Pfaff et al., 2018). In this context, molar activity is typically calculated as radioactivity per mole of tracer precursor (typically presented as MBq/nmol or GBq/ $\mu$ mol).

Generator produced  $^{68}\text{Ga}$  excels in convenience but has in recent years showed some lack in scalability. The undeniable clinical success of  $^{68}\text{Ga}$ -tracers like the SSA family of tracers and [ $^{68}\text{Ga}$ ]Ga-PSMA has greatly increased demand for  $^{68}\text{Ga}$  in recent years. The resulting shortage of  $^{68}\text{Ge}/^{68}\text{Ga}$  generators (Mueller et al., 2019) has motivated the development of alternative sources of  $^{68}\text{Ga}$ . Hence, several examples of application of medical cyclotron-produced  $^{68}\text{Ga}$  for labelling of the most frequently used  $^{68}\text{Ga}$ -radiotracers have been recently presented (Rodnick et al., 2022; Tieu et al., 2019).

### 2.3.2 Radiolabelling with aluminium-fluoride-18

Fluorine-18 has a physical half-life of 109.8 minutes with mean and maximum  $\beta^+$  energies of 0.25 and 0.84 MeV, respectively. This results in a mean  $\beta^+$  range of 0.27 mm in soft tissue compared to 1.05 mm for  $^{68}\text{Ga}$  (Sanchez-Crespo, 2013). While the decay characteristics of  $^{68}\text{Ga}$  are clearly sufficient for clinical PET imaging, its high positron energy may limit spatial resolution and decrease the accuracy of quantitative analysis of small physiological features in high-resolution PET imaging of small animals (Disselhorst et al., 2010; X. Liu & Laforest, 2009). This has motivated development of  $^{18}\text{F}$  labelling methods of peptides and other biomolecules (Richter & Wuest, 2014).

Fluoride forms a particularly strong ionic bond with aluminium (bond strength 670 kJ/mol). Coordination complexes of [ $^{18}\text{F}$ ]AlF are thermodynamically stable and can survive in physiological conditions (Bruce Martin, 1996). In a coordination complex with NOTA, the fluoride ion occupies one coordinative bond, leaving 5 to bind to the chelator. In practical terms, [ $^{18}\text{F}$ ]AlF can be used for radiolabelling biomolecules in a manner that closely resembles radiometallic labelling and can thus be described by the term “pseudo-radiometallic”.

Since the AlF labelling method was first presented (McBride et al., 2009), it has generated a considerable number of applications for radiolabelled peptide conjugates (Archibald & Allott, 2021). Refinements of the method include chelator development, automated radiosynthesis, GMP compliant labelling protocols. Moreover, several [ $^{18}\text{F}$ ]AlF-radiopharmaceuticals have reached clinical trials, hinting at good clinical translation of the AlF labelling strategy.

For AlF-labelling,  $[^{18}\text{F}]\text{F}^-$  is conventionally produced in a cyclotron with an  $^{18}\text{O}$ -water liquid target through the  $^{18}\text{O}(\text{p},\text{n})^{18}\text{F}$  nuclear reaction. The formation of  $[^{18}\text{F}]\text{AlF}$  from  $[^{18}\text{F}]\text{F}^-$  and  $\text{AlCl}_3$  is pH dependant, with the optimal pH range being 4-5, and chelation is in turn improved by the addition of organic co-solvents (D'Souza et al., 2011). Cyclotron generated fluoride can be used as is, but quaternary methyl ammonium (QMA) extraction is often done to remove possible metal ion impurities which may interfere with chelation. After formation of  $[^{18}\text{F}]\text{AlF}$  at room temperature for 2-3 minutes, tracer precursor can be added to the same reaction vessel for chelation. Thus, labelling is achievable in a one-pot manner closely resembling procedures for radiometallic labelling (Figure 9).

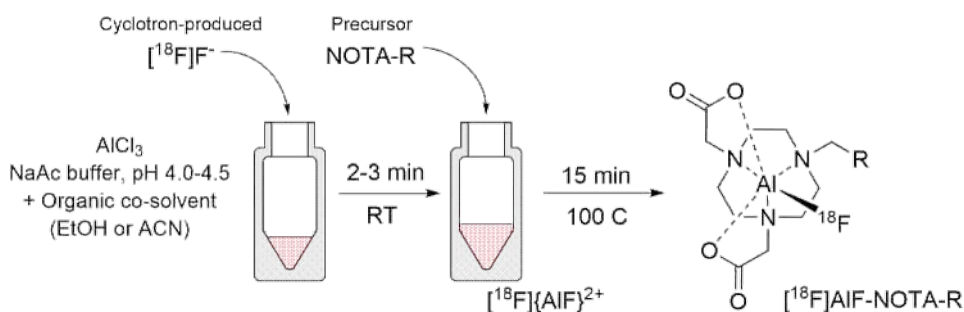


**Figure 9.** A generalized reaction scheme for  $[^{18}\text{F}]\text{AlF}$ -labelling of NOTA-conjugated tracers.

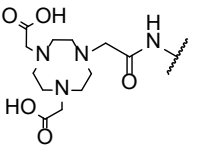
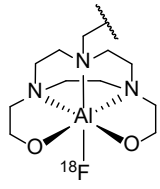
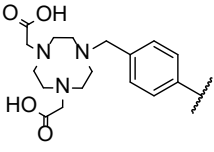
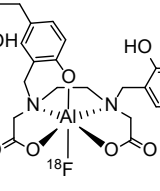
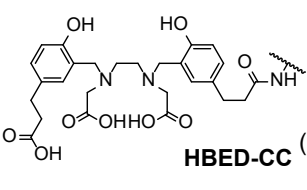
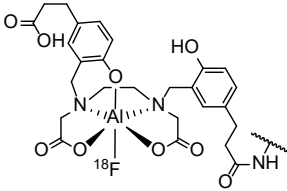
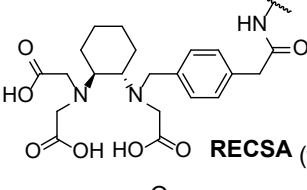
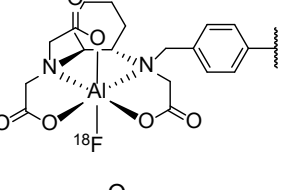
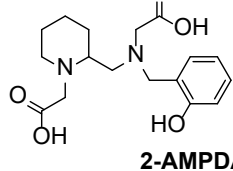
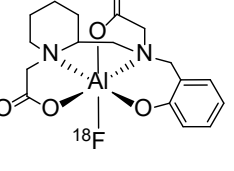
### Bifunctional chelators used for $[^{18}\text{F}]\text{AlF}$ -labelling

The greatest coordination complex stability for aluminium fluoride-18 is achieved by TACN-based bifunctional chelators with a  $\text{N}_3\text{O}_2$  (CN 5) donor structure: NODA and NOTA (when conjugated by one of its carboxylic acid arms). The NODAGA-chelator ( $\text{N}_3\text{O}_3$ , CN 6) also forms a stable complex with  $[^{18}\text{F}]\text{AlF}$ , but the free carboxylic arm competes for chelation, lowering radiochemical yield (D'Souza et al., 2011; Shetty et al., 2010). The NOTA-chelator is currently the most widely used in  $[^{18}\text{F}]\text{AlF}$  radiopharmaceuticals presented in literature and is efficiently labelled at temperatures in the 100 – 120 °C range (Archibald & Allott, 2021).

The elevated temperature combined with the possible organic co-solvents needed to chelate TACN-chelators place some requirements on the stability of the targeting vector-chelator conjugate, which has in turn motivated the development of acyclic chelators that may be chelated under milder conditions. Initial investigations by Cleeren et al. produced chelators that labelled easily but were eventually too unstable (Cleeren et al., 2016), by persistent effort they arrived at the acyclic chelator RECSA (restrained complexing agent) that enables  $[^{18}\text{F}]\text{AlF}$  chelation in RT with complex stability comparable to NODA (Cleeren et al., 2017). Notably, RECSA was conjugated to, and used for labelling of human serum albumin (radiochemical yield (RCY) of 35-

53 %), CRIG-targeting nanobody (RCY 52-63 %) and a HER2-targeting affibody (RCY 20 %  $\pm$  7) and evaluated in rats, mice and rhesus monkeys, respectively.

Another recently presented acyclic chelator showing room temperature labelling of [ $^{18}\text{F}$ ]AlF combined with sufficient stability in physiological conditions is 2-AMPTA-HB, based on the 2-aminomethylpiperidine (AMP) structure. The chelator showed good complex stability in both *in vitro* and *in vivo* (Russelli et al., 2020). It should be noted that the chelator has not to date been evaluated in complete radiotracer conjugate. The chemical structures of 2-AMPTA-HB and aforementioned chelators are presented below in Figure 10.

Chelator	[ $^{18}\text{F}$ ]AlF complex	Representative labelling conditions
 <p><b>NOTA (1)</b></p>		<p>[<math>^{18}\text{F}</math>]{AlF}<math>^{2+}</math> incubated with <b>1</b> in 0.1 M NaOAc (pH 4.0) at 100°C for 15 min. (Da Pieve et al., 2016)</p>
 <p><b>NODA (2)</b></p>		<p>[<math>^{18}\text{F}</math>]{AlF}<math>^{2+}</math> incubated with <b>2</b> in 0.1 M NaOAc (pH 4.0) at 100°C for 15 min. (Da Pieve et al., 2016)</p>
 <p><b>HBED-CC (3)</b></p>		<p>[<math>^{18}\text{F}</math>]{AlF}<math>^{2+}</math> incubated with <b>3</b> in 0.5M NaOAc (pH 4.2) at 50°C for 15 min. (Al-Momani et al., 2017)</p>
 <p><b>RECSA (4)</b></p>		<p>[<math>^{18}\text{F}</math>]{AlF}<math>^{2+}</math> incubated with <b>4</b> in 0.1 M NaOAc (pH 4.5) in RT for 12 min. (Cleeren et al., 2017)</p>
 <p><b>2-AMPDA-HB (5)</b></p>		<p>[<math>^{18}\text{F}</math>]{AlF}<math>^{2+}</math> incubated with <b>5</b> in 0.1 M NaOAc (pH 5.0) in RT for 12 min. (Russelli et al., 2020)</p>

**Figure 10.** Bifunctional chelators used for [ $^{18}\text{F}$ ]AlF-labelling. Revised from Archibald & Allott, 2021.

[ $^{18}\text{F}$ ]AIF has also been attached to the acyclic HBED-CC chelator in PSMA-11 (Malik et al., 2015). Interestingly, the hexadentate HBED-CC is clearly a suboptimal hexadentate chelator for [ $^{18}\text{F}$ ]AIF with notable instability in water in RT with a radiochemical purity (RCP) of only 64.5% just after purification, subsequently dropping to 52.7% after 2 hours (Lütje et al., 2019). Stability was improved by suspension in a 25 mM  $\text{NH}_4\text{OAc}$ , pH 6.9 buffer (98.5% to 94.7% RCP in 120 minutes). Despite the shortcoming of the HBED chelator, [ $^{18}\text{F}$ ]AIF-PSMA-11 has proceeded to clinical evaluation with good results, showing very similar imaging performance to current standard tracer, [ $^{68}\text{Ga}$ ]Ga-PSMA-11 (Pattison et al., 2022; Piron et al., 2019). Importantly, no significant bone uptake was observed.

In conclusion, [ $^{18}\text{F}$ ]AIF labelling methodology offers a viable and promising alternative to  $^{68}\text{Ga}$  for radiolabelling peptides and other biomolecules, especially in terms of improved resolution in small animal imaging and potentially better scalability in the clinical setting.

### 2.3.3 Radiolabelling with zirconium-89

Immuno-PET combines the remarkable target specificity of immunoglobulin (IgG) monoclonal antibodies (mAb), their engineered fragments and other peptide motifs. With the explosive growth of antibody-based new molecular entities as well as the success of existing mAb-based drugs (R. M. Lu et al., 2020), the interest in labelling antibodies for PET imaging has likewise increased dramatically. The long circulation time of conventional antibodies (from a few days to several weeks) puts them well out of reach for common short-lived radionuclides.

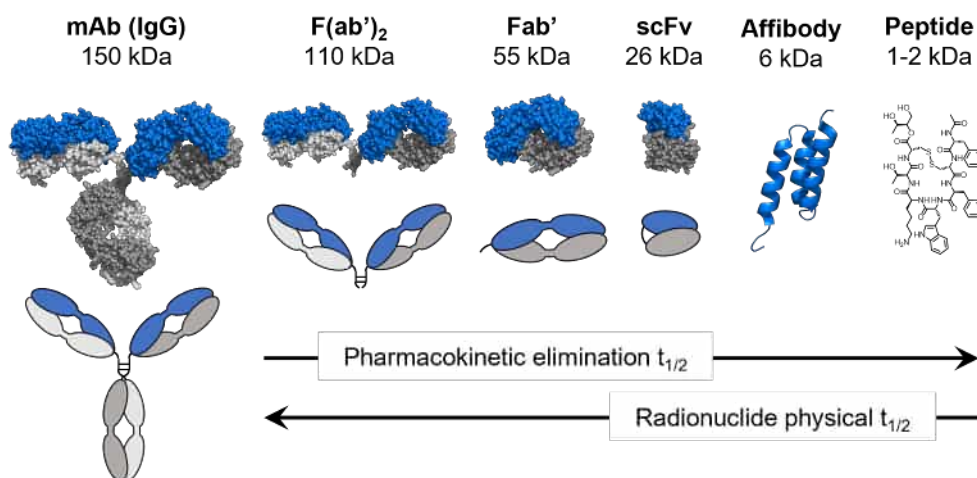


**Figure 11.** Different targeting proteins and engineered peptides used in immuno-PET and the relation between the pharmacokinetic elimination of the targeting motif versus the physical half-life required for the radionuclide. Structural images from PDB: 1IGT, Eigenbrot et al., 2010; 2KZJ, Lisa J. Harris et al., 1997)

Previously, mAbs have been labelled with  $^{64}\text{Cu}$  ( $t_{1/2} = 12.7$  h),  $^{86}\text{Y}$  ( $t_{1/2} = 12.7$  h) and  $^{124}\text{I}$  ( $t_{1/2} = 4.18$  d). However, these radionuclides each have limitations that disadvantage their suitability for clinical imaging. Practically,  $^{86}\text{Y}$  and  $^{64}\text{Cu}$  have too short half-lives. While  $^{124}\text{I}$  has a physical half-life matching the biological half-life of antibodies, its decay characteristics lead to relatively low spatial resolution. More importantly, its proclivity towards *in vivo* dehalogenation (Carrasquillo et al., 2011; Divgi et al., 2007) can lead to increased unspecific uptake in the thyroids (Zettlitz et al., 2017). For these reasons, there has been a recent surge of  $^{89}\text{Zr}$ -labelled antibodies presented in literature. Further,  $^{89}\text{Zr}$  is easier to produce through the  $^{89}\text{Y}(p,n)^{89}\text{Zr}$  reaction on a solid  $^{89}\text{Y}$  target and is safer to handle than the iodine alternative. The physical half-life of  $^{89}\text{Zr}$  (78.4 h or 3.27d) is also suitable for antibodies.

### Bifunctional chelators used for $^{89}\text{Zr}$ -labelling

The current standard for  $^{89}\text{Zr}$  labelling of mAbs is the BFC *p*-isothiocyanatobenzyl-desferrioxamine (p-DFO-Bz-NCS, also known as DFO-pPhe-NCS), that allows for conjugation of DFO to unspecific lysine residues on the antibody (Figure 12). Generally, a reproducible 1.5:1 ratio of chelator-to-antibody is achieved with a three-fold molar excess of chelator to antibody and the reaction completes almost quantitatively at room temperature at pH 9.0 (Perk et al., 2010). This allows for both bioconjugation and coordination complex formation in conditions well tolerated by antibodies.

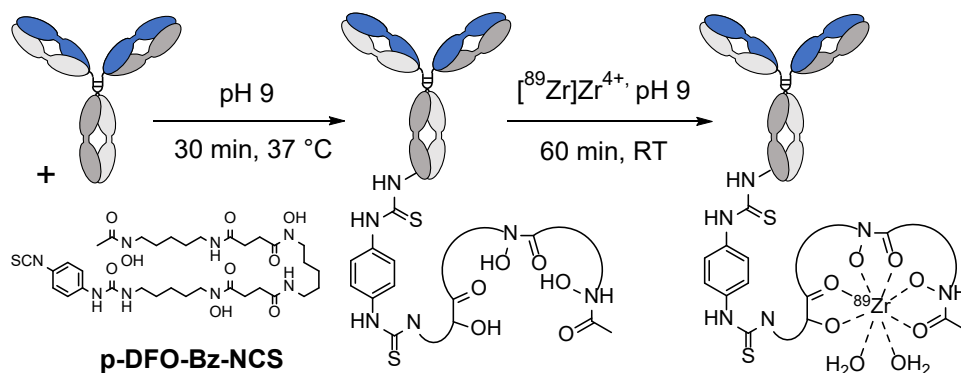


Figure 12. Representative radiolabeling protocol for  $^{89}\text{Zr}$ -labelling using the bifunctional chelator *p*-isothiocyanatobenzyl-desferrioxamine (p-DFO-Bz-NCS, Vosjan et al., 2010).

The  $\text{Zr}^{4+}$  anion is an oxophile, i.e. it prefers oxygen-based chelating moieties. In DFO, chelation is achieved by the oxygen species in repeating hydroxamate moieties. As a chelator, DFO leaves two coordination bonds open for water molecules to complete the coordination sphere to an octadentate configuration, which may lead to *in vivo*

demetallation. Like  $[^{68}\text{Ga}]^{3+}$  and  $[^{18}\text{F}]^-$ ,  $[^{89}\text{Zr}]\text{Zr}^{4+}$  readily accumulates into bones if let loose from the chelating structure (Abou et al., 2011), so this can be an issue especially in tracers targeting bone-related diseases (e.g. bone metastases). Increased bone uptake has been observed in preclinical studies, but interestingly the effect is not seen in clinical trials (Feiner et al., 2021).

Arising from the concerns raised by the suspected instability of the DFO-moiety, efforts to develop more optimized ligands have been presented. Foremost, lengthening the DFO-chelator by one hydroxamate-subunit completes the octadentate coordination preferred by  $\text{Zr}^{4+}$ . The chelator, coined DFO\* showed much improved *in vitro* stability (Patra et al., 2014) In a preclinical evaluation of  $[^{89}\text{Zr}]\text{Zr}$ -DFO- and  $[^{89}\text{Zr}]\text{Zr}$ -DFO\*-pPhe-NCS conjugated to trastuzumab in human gastric carcinoma (N87) xenograft mice, DFO\* showed comparable tumour uptake compared to DFO (47.7% %ID/g vs 35.5 %ID/g, respectively) with significantly lower bone uptake of 1.7 %ID/g vs 3.0 %ID/g (Vugts et al., 2017).

The downside of DFO\* is decreased solubility caused by the introduction of an additional alkyl chain on the DFO structure has spurred further chelator development. Showing similar  $^{89}\text{Zr}$ -complex stability to DFO\*, DFOcyclo\* was bifunctionalized with an isothiocyanate moiety and conjugated to trastuzumab. In SKOV-3 human ovarian carcinoma xenograft mice,  $[^{89}\text{Zr}]\text{Zr}$ -DFO-cyclo\*-trastuzumab showed similar tumour uptake combined with lower bone uptake, similar to the  $[^{89}\text{Zr}]\text{Zr}$ -DFO\*-pPhe-trastuzumab (Raavé et al., 2019). A structure with a similar purpose of increasing denticity, a squaramide ester (SqOEt) was introduced to DFO. Hexadentate conjugation was attributed to ligation to the oxygen species on the squaramide moiety. The structure, conjugated to trastuzumab, showed higher tumour to bone-ratios vs DFO-trastuzumab in a SKOV3 xenograft mouse model (S. E. Rudd et al., 2016). For some reason, bone uptake was not reported individually in the paper. When  $[^{89}\text{Zr}]\text{Zr}$ -DFO-SqOEt-trastuzumab was later compared *in vivo* to  $[^{89}\text{Zr}]\text{Zr}$ -DFO\*-SqOEt-trastuzumab, the latter showed much reduced bone-uptake in a BT-474 human breast cancer xenograft mouse model (Chomet et al., 2021). This raised some doubts about the participation of the squaramide-moiety to the Zr-coordination complex. In the same study,  $[^{89}\text{Zr}]\text{Zr}$ -DFO\*-pPhe-NCS and  $[^{89}\text{Zr}]\text{Zr}$ -DFO\*-SqOEt showed comparable biodistribution.

Considering that instability of the DFO-chelator has not translated into clinical  $[^{89}\text{Zr}]\text{Zr}$ -DFO-mAb-tracers, it remains to be seen if the increased complex stability of the DFO\*-chelator outweighs the lower solubility attributes in clinical translation. Nevertheless, the DFO\* may at minimum provide value in allowing imaging after significantly extended periods after injection, as shown by successful PET imaging of  $[^{89}\text{Zr}]\text{Zr}$ -DFO\*-mAb in rhesus monkey up to 30 days after injection (Berg et al., 2020).



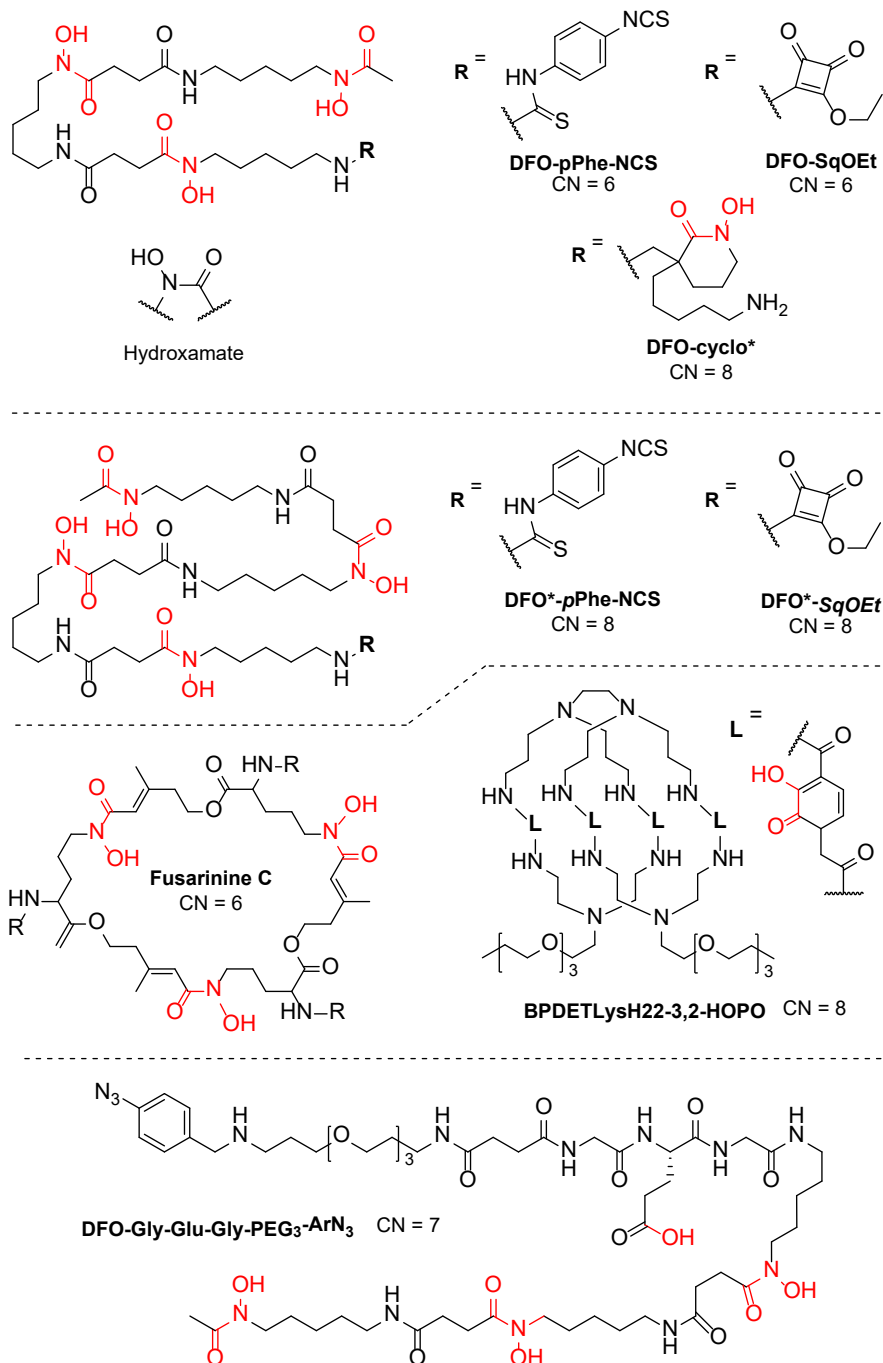


**Figure 13.** Bifunctional chelators presented in literature for <sup>89</sup>Zr labelling. Moieties that take part in complex formation are colored red.

In an alternative approach presented by Guillou and co-workers, the hexadentate coordination complex of DFO was extended into heptadentate coordination by introduction of coordination-capable carboxylic acid via a glycine-glutamine-glycine tripeptide linker. The resulting BFC DFO-Gly-Glu-Gly-PEG<sub>3</sub>-ArN<sub>3</sub> was conjugated to onartuzumab and the mAb conjugate showed lower bone in a mouse tumour xenograft model compared to a DFO-PEG<sub>3</sub>-onartuzumab used as a control, even though *in vitro* complex stability was not significantly improved versus the hexadentate control (Guillou et al., 2022). The presented BFC uses a photoactivated conjugation method for antibody conjugation which allows the production labelled antibody conjugate in one pot in 25 minutes, which is a notable improvement to the commonly used two-step protocols (Klingler & Holland, 2022).

In the acyclic chelator space, the chelators showing the most promise have been Fusarine C (FSC)- or hydroxypyridone (HOPO)-based. Zhai and co-workers presented a trimeric Arg-Gly-Asp (RGD) peptide conjugate of FSC, FSC(succ-RGD)<sup>3</sup>. The conjugate was evaluated *in vivo*, but unfortunately, the [<sup>89</sup>Zr]Zr-FSC(succ-RGD)<sup>3</sup> was only evaluated until 4h after injection, so conclusions on bone uptake at more relevant later time points could not be drawn. In a latter study, FSC was conjugated to epidermal growth factor receptor (EGFR) targeting affibody molecule ZEGRF:2377 in a head-to-head study versus DFO-ZEFRD:2377 (Summer et al., 2018). In this context, FSC showed no reduction in bone uptake 24 h post-injection compared to DFO. The FSC in the case was hexadentate, again hinting at the importance of the octadentate coordination.

Lastly, a macrocyclic chelator based on a 2-hydroxy-3-pyridone (2,3-HOPO)-moiety, BPDETLysH22-3,2-HOPO was conjugated to trastuzumab and evaluated in SKOV-3 xenograft mice (Tinianow et al., 2016). Unfortunately, despite having a octadentate structure, the HOPO-based tracer showed higher bone and liver uptakes compared to [<sup>89</sup>Zr]Zr-DFO-pPhe-trastuzumab.

Although not included in this preview due to the lack of *in vivo* evaluation data, numerous additional chelator candidates as well as BFC conjugating strategies for <sup>89</sup>Zr labelling have been presented in literature and this field of research is very active (Feiner et al., 2021). Still, DFO-pPhe-NCS remains the standard BFC for <sup>89</sup>Zr-labelling of antibodies. Notably, the DFO-moiety has enabled <sup>89</sup>Zr-labelling of molecules throughout the immune-PET spectrum, from antibodies to antibody fragments (Nagengast et al., 2011; Varasteh et al., 2021), scFv fragments (Alizadeh et al., 2018, 2021) and affibodies (Xu et al., 2020; Zhai et al., 2015).

## 2.4 PET imaging of inflammation

Inflammatory diseases plaguing modern man are numerous both in variety of conditions and number of people affected. These conditions include rheumatoid arthritis, atherosclerosis, myocarditis, inflammatory bowel disease and diabetes. Further, there is often an inflammatory component in certain cancers (Coussens & Werb, 2002; Greten & Grivnickov, 2019). Likewise, inflammation plays a role in various neurological disorders, such as multiple sclerosis, Alzheimer's disease and dementia (Jain et al., 2020). The commonness of these diseases particularly in modern western populations is a driving force for a large amount of medical research during recent decades. The onset of inflammation is followed by the release of pro-inflammatory mediators, increased permeation of leukocytes through the vascular endothelium, tissue damage and later, attempts to repair the damaged area. These phenomena offer a variety of potential targets for molecular imaging.

As mentioned previously, current nuclear medicine field of inflammation imaging heavily relies on the glucose analog [ $^{18}\text{F}$ ]FDG. The biggest limitation of [ $^{18}\text{F}$ ]FDG for inflammation is the lack of ability to clearly distinguish between physiological and pathological uptake, especially concerning areas of high physiological uptake, such as heart and brain. Likewise, physiological [ $^{18}\text{F}$ ]FDG uptake is sensitive to patient preparation prior to imaging (Pijl et al., 2021).

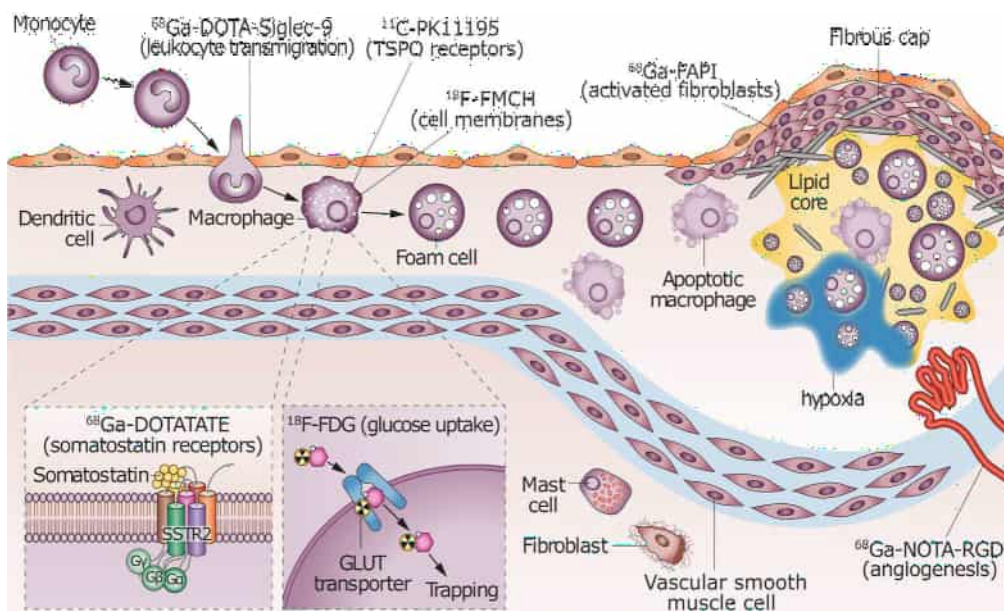


**Figure 14.** Illustration of some of the potential radiopharmaceuticals targeting various receptors related to inflammation in atherosclerosis. Adapted and reprinted with permission from MacMillan Publishers LTD (Tarkin et al., 2014).

**Table 4.** Overview of radiotracers and their targets presented for PET imaging of inflammation.

Target	PET radiotracer*	Target cell types or pathology targeted	Evaluated inflammatory conditions
Clinical and preclinical			
<b>CXCR4</b>	<sup>68</sup> Ga-pentixafor <sup>1-5</sup>	Monocytes, macrophages, T-cells	Atherosclerosis <sup>1,2</sup> , MI <sup>3</sup> , infection <sup>4-5</sup> .
<b>αvβ3-integrin</b>	<sup>18</sup> F-fluciclatide <sup>6,9</sup> <sup>18</sup> F-Galacto-RGD <sup>7</sup> <sup>68</sup> Ga-NODAGA-RGD <sup>8</sup> <sup>68</sup> Ga-PRGD2 <sup>10,11</sup>	Angiogenesis	Atherosclerosis <sup>6-8</sup> , MI <sup>9,10</sup> , arthritis <sup>11</sup>
<b>FAP</b>	<sup>68</sup> Ga-FAPI <sup>12-14,16</sup> <sup>89</sup> Zr-28H1 <sup>15</sup>	Activated fibroblasts	Atherosclerosis <sup>12</sup> , MI <sup>13,14</sup> Rheumatoid arthritis <sup>15,16</sup>
<b>SSTR</b>	<sup>68</sup> Ga-DOTA-TATE <sup>17,21</sup> <sup>68</sup> Ga-DOTA-TOC <sup>18,20</sup> <sup>68</sup> Ga-DOTA-NOC <sup>19</sup>	M1 macrophages	Atherosclerosis <sup>17</sup> , Sarcoidosis <sup>18,19</sup> , myocarditis <sup>20</sup> , MI <sup>20,21</sup>
<b>TSPO</b>	<sup>11</sup> C-PK11195 <sup>22,24,25</sup> <sup>18</sup> F-flutriciclamide <sup>23</sup>	Activated microglia and systemic monocytes	Atherosclerosis <sup>22,23</sup> vascular inflammation <sup>24</sup> rheumatoid arthritis <sup>25</sup>
Preclinical			
<b>CCR2</b>	<sup>68</sup> Ga-ECL1i <sup>26</sup> <sup>64</sup> Cu-ECL1i <sup>27,28</sup>	Inflammatory monocytes, T cells, dendritic cells	Cardiac injury <sup>26</sup> , lung inflammation <sup>27</sup> , pulmonary fibrosis <sup>28</sup>
<b>CD206</b>	<sup>18</sup> F-FDM <sup>29</sup> <sup>68</sup> Ga-NOTA-MSA <sup>30,32</sup> <sup>68</sup> Ga-NOTA-anti-MMR-Nb <sup>31,33</sup>	M2 Macrophages	Atherosclerosis <sup>29-31</sup> myocarditis <sup>32</sup> , MI <sup>33</sup>
<b>ChT</b>	<sup>18</sup> F-FMCH <sup>34</sup>	Macrophages	Atherosclerosis <sup>34</sup>
<b>SR-A1</b>	<sup>89</sup> Zr-Mal-HSA <sup>35</sup>	M1 Macrophages	Atherosclerosis <sup>35</sup>
<b>CD40</b>	<sup>89</sup> Zr-Anti-CD40 <sup>36</sup>	M1 macrophages, B lymphocytes, epithelial cells	Atherosclerosis <sup>36</sup>
<b>GAL3</b>	<sup>89</sup> Zr-DFO-Gal3-F(ab') <sub>2</sub> <sup>37</sup>	M2 macrophages	Atherosclerosis <sup>37</sup>

\*Example radiotracers, many of the targets have various additional tracers or tracer analogues in development. References: <sup>1</sup>(Hyafil et al., 2017), <sup>2</sup>(Kircher et al., 2020), <sup>3</sup>(Reiter et al., 2018), <sup>4</sup>(Bouter et al., 2018), <sup>5</sup>(Derlin et al., 2017), <sup>6</sup>(W. S. Jenkins et al., 2019), <sup>7</sup>(Beer et al., 2014), <sup>8</sup>(Dietz et al., 2021), <sup>9</sup>(W. S. A. Jenkins et al., 2017), <sup>10</sup>(Sun et al., 2014), <sup>11</sup>(Zhu et al., 2014), <sup>12</sup>(Wu et al., 2022), <sup>13</sup>(Varasteh, Mohanta, Robu, et al., 2019), <sup>14</sup>(Siebermair et al., 2021), <sup>15</sup>(Ge et al., 2022), <sup>16</sup>(Laverman et al., 2015), <sup>17</sup>(Tarkin et al., 2017), <sup>18</sup>(Nobashi et al., 2016), <sup>19</sup>(Gormsen et al., 2016), <sup>20</sup>(Lapa et al., 2015), <sup>21</sup>(Tarkin et al., 2019), <sup>22</sup>(Gaemperli et al., 2012), <sup>23</sup>(Hellberg et al., 2018; Thackeray et al., 2018) <sup>24</sup>(Lamare et al., 2011), <sup>25</sup>(Gent et al., 2015), <sup>26</sup>(Heo et al., 2019), <sup>27</sup>(Y. Liu et al., 2017), <sup>28</sup>(Brody et al., 2021), <sup>29</sup>(Tahara et al., 2014), <sup>30</sup>(E. J. Kim et al., 2016), <sup>31</sup>(Varasteh, Mohanta, Li, et al., 2019), <sup>32</sup>(Lee et al., 2017), <sup>33</sup>(Varasteh et al., 2022), <sup>34</sup>(Hellberg et al., 2016) <sup>35</sup>(Ahmed et al., 2020), <sup>36</sup>(Poels et al., 2022), <sup>37</sup>(Varasteh et al., 2021).

In the preclinical and early clinical stages, multiple targets and corresponding radiotracers have been presented. These include, and are not limited to, somatostatin receptor (SSTR), 18 kDa translocator protein (TSPO), C-X-X motif chemokine receptor 4 (CXCR4),  $\alpha_v\beta_3$ -integrin, fibroblast activation protein (FAP), C-C motif chemokine receptor 2 (CRR2), mannose receptor (CD206), choline transporters (ChT), class A1 scavenger receptor (SR-A1), the CD40 molecule and galectin-3 (GAL-3). These targets and corresponding PET radiotracers that have specifically been evaluated for imaging inflammation are presented in Table 4. Examples of radiopharmaceuticals used to target atherosclerosis are given in Figure 14. The targets related to the studies presented in this thesis, vascular adhesion protein-1 (VAP-1) and folate receptor  $\beta$  (FR- $\beta$ ) are excluded from the table and presented in their own chapters. Likewise, PET imaging of neuroinflammation has been excluded from this review to maintain relevance to thesis subprojects.

### Radiotracers targeting surface proteins of immune cells

Excluding [ $^{18}\text{F}$ ]FDG, among tracers already approved for routine clinical use, the somatostatin receptor targeting somatostatin analogue (SSA) tracers ([ $^{68}\text{Ga}$ ]Ga-DOTATATE, [ $^{68}\text{Ga}$ ]Ga-DOTATOC and [ $^{68}\text{Ga}$ ]Ga-DOTANOC have been explored for clinical imaging of inflammatory heart conditions, including atherosclerosis (Tarkin et al., 2017), sarcoidosis (Nobashi et al., 2016), myocarditis and myocardial infarction (Lapa et al., 2015) and other conditions with chronic inflammation, such as pulmonary fibrosis and rheumatoid arthritis (Anzola et al., 2019). SSTR is overexpressed on pro-inflammatory M1 macrophages and should be able to target these conditions (X. Li et al., 2013). Comparison studies between [ $^{18}\text{F}$ ]FDG and SSAs seem to have mostly favoured the former due to improved diagnostic performance (Gormsen et al., 2016; Tarkin et al., 2017). Notably, many of these studies were retrospective, with many patient cohorts originally intended for tumour imaging.

Another tracer in early clinical evaluation of inflammatory conditions is CXCR4-targeting [ $^{68}\text{Ga}$ ]Ga-Pentixafor. CXCR4 is diversely expressed on B and T lymphocytes, and macrophages in inflamed tissue (Tanios et al., 2015), providing a clear target for imaging. [ $^{68}\text{Ga}$ ]Ga-Pentixafor has been investigated in prospective clinical trials for imaging atherosclerosis, myocardial infarction and other cardiovascular diseases. Importantly, the tracer was able to identify more lesions than [ $^{18}\text{F}$ ]FDG (Kircher et al., 2020). The authors note that the underlying biological mechanisms and expression of CXCR4 in atherosclerosis are not completely known and warrant further investigation. Additionally, increased tracer uptake in infarcted areas have been observed in patients with myocardial infarction (MI) (Reiter et al., 2018).

While its main use is in neuroinflammation (Downer et al., 2020), TSPO-targeting tracers have been evaluated for some other inflammatory conditions, in which the

protein is overexpressed on macrophages and monocytes. Thus far published clinical studies have used [ $^{11}\text{C}$ ]PK11195, and the tracer was shown to visualize plaque inflammation in atherosclerosis and distinguish between symptomatic and asymptomatic plaques (Gaemperli et al., 2012). However, in a 2021 paper, Schollhammer and co-workers reported that newer TSPO tracers [ $^{11}\text{C}$ ]PBR28 and [ $^{18}\text{F}$ ]PBR06, did not detect vascular inflammation despite high affinity and specific binding to TSPO (Schollhammer et al., 2021). The authors surmise that uptake signal, may have been masked by residual plasma radioactivity induced by TSPO receptor expressed on plasma platelets and white cells.

In the preclinical phase, many novel tracers have been able to visualize inflammation *in vivo*. These include CCR2-targeting [ $^{68}\text{Ga}$ ]Ga and [ $^{64}\text{Cu}$ ]Cu-ECL1i, utilizing a 7-D-amino acid sequence nominated “extracellular loop 1 inverso” (ECL1i) targeting CCR2 on the surface of immune cells (Heo et al., 2019) and [ $^{18}\text{F}$ ]fluoromethylcholine ([ $^{18}\text{F}$ ]FMCH) targeting the increased choline kinase activity of macrophages (Hellberg et al., 2016).

Recently  $^{89}\text{Zr}$ -labelled tracers have been presented for imaging inflammation. The first of these is a maleic-acid decorated human serum albumin tracer [ $^{89}\text{Zr}$ ]Zr-Mal-HSA, targeting SR-A1 (Ahmed et al., 2020). Notably, SR-A1 has special relevance to atherosclerosis, as the receptor is associated with the intake of lipids into macrophages and the subsequent development into foam cells (de Winther et al., 2000). The second  $^{89}\text{Zr}$ -labelled tracer presented is [ $^{89}\text{Zr}$ ]Zr-Anti-CD40, a  $^{89}\text{Zr}$ -labelled anti-CD40 antibody, which was very recently successfully used to visualize atherosclerotic plaques in mice (Poels et al., 2022). CD40 is a known marker of M1 macrophages and has been linked to vulnerable plaques (Schönbeck & Libby, 2001).

## Radiotracers targeting alternatively activated macrophages

Relevant to study IV, a few novel radiotracers targeting so-called alternatively activated macrophages, also known as M2 macrophages have appeared in recent literature. While classically activated M1 macrophages are distinctly pro-inflammatory, M2 macrophages are immunoregulative and participate in wound healing and tissue repair (Orecchioni et al., 2019). Firstly, radiotracers targeting the mannose receptor CD206, a receptor predominantly expressed on M2 macrophages (Bouhleb et al., 2007), have been presented in preclinical studies.

2-Deoxy-2-[ $^{18}\text{F}$ ]fluoro-*D*-mannose ([ $^{18}\text{F}$ ]FDM) showed very similar uptake to [ $^{18}\text{F}$ ]FDG in atherosclerotic plaques (Tahara et al., 2014). The authors however reported low radiochemical yields (< 5%) and the tracer has not been present in literature since. [ $^{68}\text{Ga}$ ]Ga-NOTA-MSA, a  $^{68}\text{Ga}$ -labelled, neomannosylated human serum albumin tracer was presented and showed an increased uptake in the atherosclerotic abdominal aorta compared to healthy tissues, and importantly, higher

uptake compared to [ $^{18}\text{F}$ ]FDG (E. J. Kim et al., 2016). The tracer also showed potential in imaging myocarditis (Lee et al., 2017).

Following these, an anti-mannose receptor nanobody labelled with  $^{68}\text{Ga}$  ( $^{68}\text{Ga}$ ]Ga-NOTA-anti-MMR-Nb) was successfully used to visualize atherosclerotic plaques in mice (Varasteh, Mohanta, Li, et al., 2019) and later, myocardial infarction in rats (Varasteh et al., 2022). Importantly, the MI study confirmed co-localization of the mannose receptor and CD-68 on macrophages present at the infarction site. Both  $^{68}\text{Ga}$ ]Ga-NOTA MSA and  $^{68}\text{Ga}$ ]Ga-NOTA-anti-MMR-Nb showed low myocardial uptake compared to [ $^{18}\text{F}$ ]FDG.

In a recent study, [ $^{89}\text{Zr}$ ]Zr-DFO-Gal3-F(ab')<sub>2</sub>, a  $^{89}\text{Zr}$ -labelled antibody fragment target galectin-3 (GAL3, also known as macrophage-3 antigen, MAC3), was used to image M2 macrophages in ApoE-KO mice. The presence of M2 macrophages in atherosclerotic lesions with increased tracer uptake was verified via CD68 and Gal3 immunohistochemistry and preferential binding the Gal3-F(ab')<sub>2</sub> to M2 macrophages was observed *in vitro* (Varasteh et al., 2021).

### Radiotracers targeting integrins

Alpha-v-beta integrin mediates cell adhesion and plays a role in angiogenesis, through which new blood vessels are generated from existing vasculature in sites of inflammation and tissue repair. Tracers containing the tripeptide Arg-Gly-Asp (RGD) motif that binds to integrin  $\alpha_v\beta_3$  are quite numerous, with 5 different tracer variants showing up in recent clinical evaluations for PET imaging of cardiovascular disease (Dietz et al., 2022). As the ground-breaking clinical RGD tracer,  $^{18}\text{F}$ -galacto-RGD showed significantly heightened uptake in atherosclerotic plaques in human arteries (Beer et al., 2014).

Around the same time, a competing tracer  $^{68}\text{Ga}$ ]Ga-PRGD2, containing a NOTA chelator conjugated to an RGD-dimer, showed increased uptake in myocardial infarction and stroke patients (Sun et al., 2014) and tracer also visualized increased expression of  $\alpha_v\beta_3$  rheumatoid arthritis (Zhu et al., 2014). More recently, the tracer [ $^{18}\text{F}$ ]fluciclatide showed increased uptake in patients with recent myocardial infarction, with uptake correlating with functional recovery at patient follow-up (W. S. A. Jenkins et al., 2017). Further, the tracer visualized  $\alpha_v\beta_3$  in human atherosclerotic plaques and was able to differentiate between unstable and stable plaques based on tracer uptake (W. S. Jenkins et al., 2019). In the most recent clinical finding in this area,  $^{68}\text{Ga}$ -NODAGA-RGD was also showed increased uptake in atherosclerotic plaques, in a retrospective study of 44 patients assessed originally for tumoral angiogenesis.

In the preclinical and oncological fields, various additional RGD-based tracers with different labelling chemistries, linker configuration and multimericity of the RGD

motif are being constantly introduced, which makes this family of radiotracers interesting from a radiochemical point of view (Notni et al., 2013).

## Radiotracers targeting fibroblast activation protein- $\alpha$

The fibroblast activation protein inhibitor (FAPI) family of novel radiotracers holds a lot of promise towards cancer and inflammation imaging. Widely touted as something that may potentially replace the gold standard [ $^{18}\text{F}$ ]FDG in many malignancies (Calais & Mona, 2021; Guglielmo & Guerra, 2021; Hicks et al., 2021), FAPI tracers currently hold a lot of expectations and interest. While clinical trials have primarily focused on tumour imaging, FAPIs hold a lot of promise for inflammation imaging, as fibroblast activity is a common component in many inflammatory conditions. Like previously mentioned integrin-targeted tracers, the FAPI family of tracers is a highly contested field of research with several potential candidates in evaluation (Lindner et al., 2021).

In the clinic, DOTA-conjugated  $^{68}\text{Ga}$ -FAPI-04 has thus far been the FAPI of choice for clinical trials of inflammation and it has been evaluated in atherosclerosis (Wu et al., 2022), myocardial infarction (Varasteh, Mohanta, Robu, et al., 2019) and immunoglobulin 4-related disease (IgG4-RD, Luo et al., 2021), with promising results. Clinical research on inflammation imaging with FAPIs is still at a very early stage and further investigations are indeed warranted to validate these early findings.

Notably, the most prominent FAPI candidates use a (4-quinolinolyl)glyciny-2-cyanopyrrolidine-based small molecule as the targeting molecule. Although small molecules have typically been labelled covalently with the  $^{18}\text{F}$ - and  $^{11}\text{C}$ -radionuclides, the FAPI field is dominated by chelator-based  $^{68}\text{Ga}$ -labelling and the most successful  $^{18}\text{F}$ -labelled variants have been achieved through the radiometal-like  $\text{Al}^{18}\text{F}$ -labelling (Kou et al., 2021; Naka et al., 2021; S. Wang et al., 2021), highlighting the value and potential of the BFC-approach for radiolabelling.

### 2.4.1 Vascular adhesion protein-1

Vascular adhesion protein-1 (VAP-1), also known as primary amine oxidase-3 (AOC3), functions as a part of an adhesion cascade which leads to the transfer of circulatory leukocytes through the vascular endothelium into tissues undergoing inflammation (Salmi & Jalkanen, 2019). More precisely, VAP-1 functions as both an adhesion molecule and an enzyme, with the primary amine oxidase activity enabling the adhesion, rolling and transmigration of leukocytes during the cascade (Jalkanen et al., 2007; Koskinen et al., 2004). In physiological conditions, VAP-1 is stored in intracellular storage vesicles. Importantly, at the onset of inflammation, the protein is translocated to the endothelial cell surface at the site of inflammation (Jaakkola et al., 2000; Salmi et al., 1993). This characteristic of VAP-1 makes it a convenient target, as



the protein remains hidden in normal tissues and readily accessible from circulation in tissues undergoing inflammation.

Sialic acid-binding Ig-like lectin 9 (SIGLEC-9) has been identified as a natural ligand for VAP-1. Further, a cyclic peptide portion of SIGLEC-9 containing amino acid residues 283-297 (amino acid sequence “CARLSLSWRGLTLCPS” was recognized as the VAP-1 binding motif (Aalto et al., 2011). Thus far, the radiotracer [ $^{68}\text{Ga}$ ]Ga-DOTA-Siglec-9, containing the CARLSLSWRGLTLCPS binding motif linked to a DOTA chelator through a (PEG)<sub>2</sub> amide linker is the most studied VAP-1 targeting tracer. Inflammatory conditions that have been successfully visualized by the tracer in animal studies include sterile skin inflammation (Aalto et al., 2011), peri-implant tissue response and staphylococcal infection (Ahtinen et al., 2014), synovitis (Virtanen et al., 2015), atherosclerosis (Virtanen et al., 2017), acute respiratory distress syndrome (Retamal et al., 2016), borrelia-induced arthritis (Siitonen et al., 2017) and osteomyelitis and soft tissue infection (Jødal et al., 2019).

Alongside the evaluation of [ $^{68}\text{Ga}$ ]Ga-DOTA-Siglec-9, alternative labelling strategies have been pursued, firstly labelling the peptide using 5-deoxy-5- [ $^{18}\text{F}$ ]fluororibose conjugation to produce [ $^{18}\text{F}$ ]FDR-Siglec-9 (Li et al., 2013). The tracer was found to have comparable imaging performance as well as dosimetry to [ $^{68}\text{Ga}$ ]Ga-DOTA-Siglec-9. However, the relatively lengthy labelling route outweighed possible benefits of the alternative methods regarding the development of fully automated synthesis for routine clinical use. Secondly, another alternative labelling method using the [ $^{18}\text{F}$ ]AIF-strategy is presented as part of this thesis work (Study I, Moision et al., 2018). The molecular structures of these tracers are presented in Figure 15.

[ $^{68}\text{Ga}$ ]Ga-DOTA-Siglec-9 has nevertheless prevailed, and spurred by its success in preclinical trials, steps towards clinical studies with [ $^{68}\text{Ga}$ ]Ga-DOTA-Siglec-9 were taken: a GMP-grade synthesis for [ $^{68}\text{Ga}$ ]Ga-DOTA-Siglec-9 was developed (Käkelä et al., 2018) and the safety of the tracer molecule was subsequently evaluated in rats (Chrusciel et al., 2019). Results from the first-in-human study of [ $^{68}\text{Ga}$ ]Ga-DOTA-Siglec-9 are presented as part of this thesis in study II (Viitanen et al., 2021).

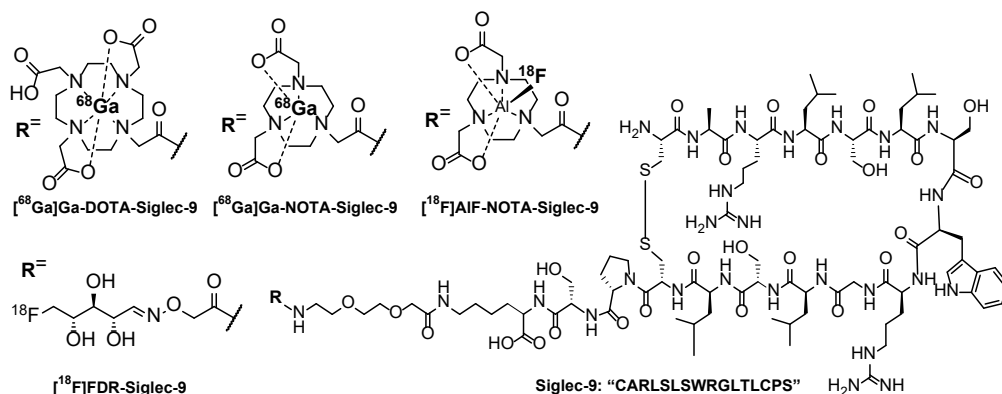


**Figure 15.** Molecular structures of VAP-1 targeting, Siglec-9 radiotracers. Folate receptor beta

## 2.4.2 Folate receptor beta

Folate receptor beta (FR- $\beta$ ) is a membrane bound surface protein overexpressed on macrophages. While originally proposed as a marker for classically activated, pro-inflammatory M1 macrophages present in atherosclerosis (Xia et al., 2009), further studies have however indicated that the receptor can be also expressed in macrophages expressing M2 phenotype markers in some physiological environments (Tsuneyoshi et al., 2012). Folate receptors, as the name suggests, bind folate and its derivatives and enable their delivery across the cell membrane (Wibowo et al., 2013). Thus, the small natural biomolecule folate (vitamin B<sub>9</sub>) offers a convenient scaffold on which several PET radioligands have been developed. While additional folate-based tracers have certainly been presented in literature, the selection of PET radiotracers presented in this review (Figure 16) was done based on published evaluation of *in vivo* imaging of inflammation.

[<sup>18</sup>F]Fluoro-PEG-Folate was the first FR- $\beta$  targeting PET tracer evaluated in inflammatory disease. The tracer showed increased uptake in inflamed joints vs healthy joints in *Bordetella pertussis* antigen-induced arthritis in rats (Gent et al., 2013). Following [<sup>18</sup>F]Fluoro-PEG-Folate, another covalently <sup>18</sup>F-labelled tracer, [<sup>18</sup>F]AzaFOL produced likewise good results in a mouse model of atherosclerosis (A. Müller et al., 2014) and an experimental mouse model of interstitial lung disease (Schniering et al., 2019). In any case, both [<sup>18</sup>F]fluoro-PEG-Folate and [<sup>18</sup>F]AzaFOL have proceeded into clinical trials (Gnesin et al., 2020; Verweij et al., 2020). Relevant to this review, the former was evaluated in rheumatoid arthritis and compared to [<sup>11</sup>C]PK11195, with the former showing superior target to background ratio. Further, [<sup>18</sup>F]fluoro-PEG-Folate seemed to correspond better with clinical outcomes (Verweij et al., 2020).

$[^{18}\text{F}]\text{AIF-NOTA-Folate}$  is another FR-targeting targeting radiotracer that has been successfully used to visualize FR- $\beta$  expressed on macrophages in animal models of atherosclerosis (Silvola et al., 2018) and autoimmune myocarditis (Jahandideh et al., 2020). Notably, the folate tracer showed improvement over  $[^{18}\text{F}]\text{FDG}$  in imaging atherosclerosis especially due to the absence of myocardial uptake while also producing an improved plaque-to-healthy vessel wall-ratio of uptake. In autoimmune myocarditis induced by porcine cardiac myosin injections in rats, tissue section staining confirmed the expression of FR- $\beta$  primarily in M1-polarized macrophages and co-localization with  $[^{18}\text{F}]\text{AIF-NOTA-Folate}$  uptake.

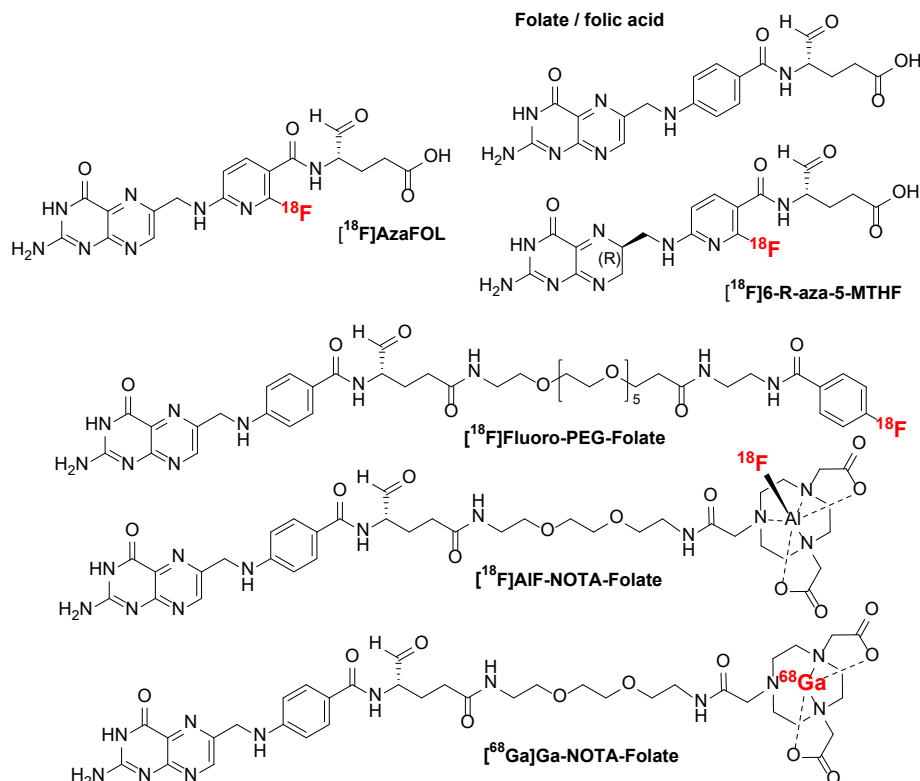


**Figure 16.** Molecular structures of folate receptor-targeting radiotracers.

Another comparative study in atherosclerotic mice with  $[^{18}\text{F}]\text{FDG}$  and the  $^{68}\text{Ga}$ -labelled variant of the NOTA-Folate tracer,  $[^{68}\text{Ga}]\text{-NOTA-Folate}$  has also been conducted (Moisio et al., 2020), and is presented as part of this thesis (study III).

### 2.4.3 Common lymphatic endothelial and vascular endothelial receptor-1

Common lymphatic endothelial and vascular endothelial receptor-1 (CLEVER-1, also known as Stabilin-1 and FEEL-1), is a multifunctional scavenger receptor (Figure 17.) clearly expressed on anti-inflammatory, alternatively activated M2 macrophages (Kzhyshkowska et al., 2006; Palani et al., 2011). Further, the molecule is presented, as the name suggests on the lymphatic and vascular endothelium. In human tissues, CLEVER-1 is natively expressed on the noncontinuous endothelial cells (ECs) in spleen, liver, adrenal cortex and lymph nodes (Goerdts et al., 1991; Hansen et al., 2005; Martens et al., 2006).

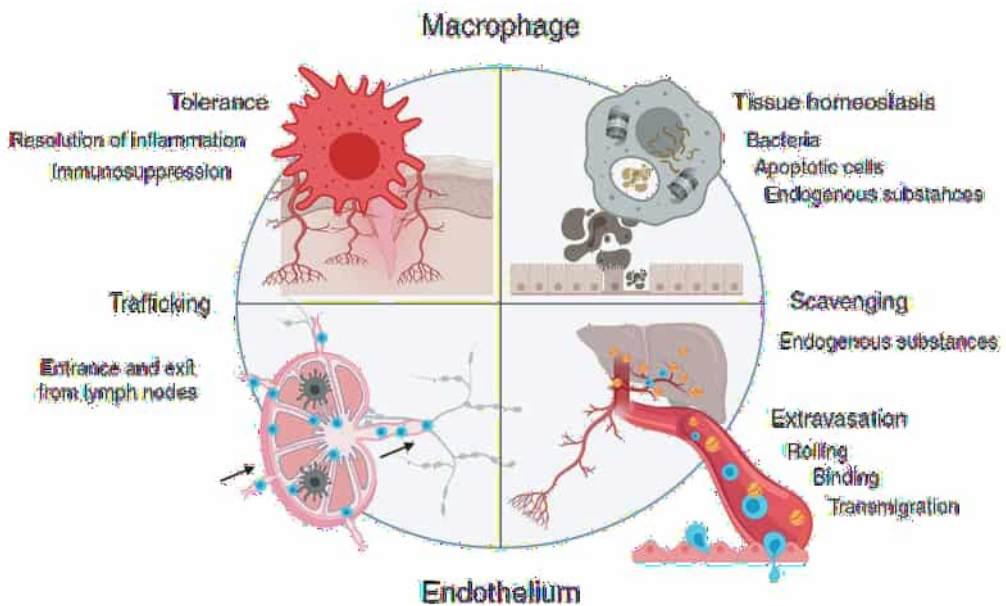


**Figure 17.** Scavenging and trafficking are shared functions for both macrophage and endothelial cell CLEVER-1. Although macrophage CLEVER-1 is an important scavenger, it also mediates macrophage binding to the endothelium and CLEVER-1 on the endothelium. Reprinted with permission (Hollmén et al. 2020).

A humanized anti-CLEVER-1 antibody bexmarilimab has been developed for immunotherapy of various cancers and has recently shown promising results in clinical trials (Virtakoivu et al., 2021). While the main research focus of CLEVER-1 remains in tumor-associated macrophages and immuno-oncology (Hollmén et al., 2020), it has been shown to regulate the transmigration of lymphocytes within the lymphatic system and from blood circulation into inflamed tissues through the vascular endothelium (Karikoski et al., 2009). It also mediates tissue homeostasis and prevents the formation

of fibrosis in liver injury (Rantakari et al., 2016). Rantakari and coworkers showed that CLEVER-1 plays a protective role against excessive fibrosis in response to oxidative stress through the scavenging of modified LDLs. The uptake of LDLs was also found to reduce profibrogenic chemokine CCL3 secretion, resulting in reduced fibrosis and promotion of healing.

It has also been previously shown that CLEVER-1 expression on macrophages and various subtypes of endothelial cells is increased during both tumorigenesis and chronic inflammation (Kzhyshkowska et al., 2006). Thus, we propose that CLEVER-1 may also be a very relevant marker M2 macrophages and monocyte transmigration, suitable for observing tissue repair and healing responses in inflammatory diseases. Notably, the humanized antibody bexmarilimab can also recognize rabbit CLEVER-1 because of favourable homology, allowing evaluation of its pharmacokinetics and biodistribution in rabbit. The results for preclinical evaluation of zirconium-89 labelled bexmarilimab are presented in study IV.

## 3 Aims

The goal of this work was to develop new PET radiopharmaceuticals to visualize inflammation and inflammation-related phenomena. We focused on three well-established biological targets: VAP-1, expressed on the endothelial cell surface in areas undergoing inflammation; FR- $\beta$ , expressed on the surface of activated macrophages; and CLEVER-1, expressed on the surface of M2 macrophages and endothelial cells. Accordingly, 5 different radiopharmaceuticals were prepared and evaluated in relevant preclinical disease models or human volunteers.

Specifically, the objectives were:

- 1) To explore alternative radiolabelling strategies for the VAP-1-targeting Siglec-9 peptide by using the NOTA-chelator to produce [ $^{68}\text{Ga}$ ]Ga- and [ $^{18}\text{F}$ ]AlF-NOTA-Siglec-9 and compare their PET imaging performance in rats with sterile skin inflammation (Study I).
- 2) To evaluate the safety, pharmacokinetics, and tentative imaging performance of [ $^{68}\text{Ga}$ ]Ga-DOTA-Siglec-9 in a first-in-human trial with healthy volunteers and a patient with rheumatoid arthritis (Study II).
- 3) To assess radiolabelling, *in vitro* and *in vivo* properties of FR- $\beta$  -targeting [ $^{68}\text{Ga}$ ]Ga-NOTA-Folate in a mouse model of atherosclerosis and compare its performance to [ $^{18}\text{F}$ ]FDG (Study III).
- 4) To establish the radiolabelling and evaluate *in vivo* biodistribution of [ $^{89}\text{Zr}$ ]Zr-DFO-bexmarilimab, a  $^{89}\text{Zr}$ -labeled monoclonal anti-CLEVER-1 antibody, in healthy rabbits and a rabbit model of renal interstitial fibrosis (Study IV).

## 4 Materials and Methods

**Table 5.** Overview of experiments and analyses conducted in each study.

Study / modality	Radiotracer	Animal model / study subjects	Additional experiments and analyses
<b>Study I</b> PET (Preclinical)	<sup>68</sup> Ga-NOTA-Siglec-9 Al <sup>18</sup> F-NOTA-Siglec-9	Turpentine-induced skin inflammation in Sprague Dawley rats	<ul style="list-style-type: none"> <li>✓ Distribution coefficient (LogD).</li> <li>✓ <i>Ex vivo</i> biodistribution</li> </ul>
<b>Study II</b> PET/CT (Clinical)	<sup>68</sup> Ga-DOTA-Siglec-9	Healthy volunteers and a patient with rheumatoid arthritis	<ul style="list-style-type: none"> <li>✓ Radiometabolite analysis.</li> <li>✓ Radiation dosimetry.</li> <li>✓ [<sup>18</sup>F]FDG scan of arthritis.</li> </ul>
<b>Study III</b> PET/CT (Preclinical)	<sup>68</sup> Ga-NOTA-Folate	Atherosclerosis in LDLR <sup>-/-</sup> ApoB <sup>100/100</sup> mice fed with a high-fat diet compared to healthy controls; Healthy Sprague Dawley rats.	<ul style="list-style-type: none"> <li>✓ Distribution coefficient (LogD).</li> <li>✓ <i>In vitro</i> FR-β binding.</li> <li>✓ Radiometabolite analysis.</li> <li>✓ <i>Ex vivo</i> biodistribution.</li> <li>✓ <i>Ex vivo</i> ARG.</li> <li>✓ H&amp;E staining and Mac3 IHC of aortic sections.</li> <li>✓ Estimation of human radiation dose.</li> </ul>
<b>Study IV</b> PET/CT (Preclinical)	<sup>89</sup> Zr-DFO-bexmarlimab	Renal fibrosis in New Zealand White rabbits as induced by the unilateral ureteral obstruction (UUO) surgery compared to healthy controls	<ul style="list-style-type: none"> <li>✓ Estimation of immunoreactivity</li> <li>✓ Renal perfusion [<sup>15</sup>O]H<sub>2</sub>O.</li> <li>✓ Radiometabolite analysis.</li> <li>✓ Pharmacokinetic analysis.</li> <li>✓ <i>Ex vivo</i> biodistribution.</li> <li>✓ <i>Ex vivo</i> ARG, H&amp;E, Sirius Red, and CLEVER-1 IHC of kidney sections.</li> <li>✓ Estimation of human radiation dose.</li> </ul>

Abbreviations: ARG - autoradiography, H&E - hematoxylin and eosin, Mac3 - Macrophage-3 antigen, IHC - immunohistochemistry, LDLR<sup>-/-</sup> - low density lipoprotein knockout, ApoB<sup>100/100</sup> - expressing only apolipoprotein-B.

## 4.1 Tracer radiolabelling and characterization

### General radiolabelling materials and methods

[<sup>68</sup>Ga]GaCl<sub>3</sub> was obtained from an IGG-100 <sup>68</sup>Ge/<sup>68</sup>Ga generator for non-GMP labelling and a Gallipharm generator for GMP labelling by elution with 0.1 M hydrochloric acid (HCl). Both generators were acquired from Eckert & Ziegler (Valencia, CA, USA). [<sup>18</sup>F]Fluoride was produced from <sup>18</sup>O-enriched water with an MGC-20 cyclotron (Efremov Scientific Institute of Electrophysical Apparatus, Leningrad, USSR) via the <sup>18</sup>O(p,n)<sup>18</sup>F nuclear reaction. Traceselect water (Honeywell, Morristown, NJ, USA) was used to produce buffers and solutions for radiosynthesis. NAP- and PD-columns (Cytiva, Chicago, IL, USA) and commonly used chemicals were purchased from Sigma-Aldrich/Merck (Darmstadt, Germany). The radio-HPLC used for determination of radiochemical purity consisted of LaChrom Instruments HPLC system (Hitachi, Tokyo, Japan) and a Radiomatic 150TR flow-through radioisotope detector (Perkin Elmer, Waltham, MA, USA) unless stated otherwise. Radiosyntheses were conducted by non-GMP protocols unless stated otherwise. Solution percentages are reported as v/v.

Radiochemical characteristics of radiolabelled compounds were determined according to current consensus nomenclature (Coenen et al., 2017) as follows: radiochemical yield (RCY) was determined as end-of-synthesis activity divided by starting activity multiplied 100 %, with activities decay-corrected to the same timepoint. In this work, molar activity was calculated as measured activity per mole of precursor (MBq/nmol or GBq/μmol). For mAb radiolabelling specific activity was used instead, calculated as measured activity per mg of precursor (MBq/mg). The limit for product release for radiochemical purity was ≥95% unless specified otherwise. If necessary, precursor concentrations were determined either from HPLC-ultraviolet chromatograms or on a nanodrop UV-spectrophotometer (Thermo Fischer Scientific, Waltham, MA, USA).

### Production of [<sup>15</sup>O]H<sub>2</sub>O

Radiowater used in Study IV was produced from [<sup>14</sup>N]nitrogen with the nuclear reaction <sup>14</sup>N(d,n)<sup>15</sup>O and transformed into [<sup>15</sup>O]H<sub>2</sub>O in its gas form on a Pt-catalyst at 700 °C in the presence of H<sub>2</sub> (Sipilä et al., 2001). Gaseous [<sup>15</sup>O]H<sub>2</sub>O was directed into a radiowater generator (Hidex, Turku, Finland) for formulation into physiological saline and dosing into study subjects.



#### 4.1.1 $^{68}\text{Ga}$ -NOTA-Siglec-9

##### *Radiolabelling*

2 mL of [ $^{68}\text{Ga}$ ]GaCl<sub>3</sub> in 0.1 M HCl from the highest activity generator elution fraction was split into two 1.5 mL microcentrifuge tubes preloaded with sodium acetate (NaOAc, 18 mg). Reaction pH was adjusted to 3-4 by addition of 47  $\mu\text{L}$  of 2 M HCl to each vial. 10 nmol of NOTA-Siglec-9 dissolved in water (10  $\mu\text{L}$ , 1 mM) was added to each vial, followed by incubation for 15 minutes at 60 °C. The reaction vials were cooled and solutions from both vials were combined onto a NAP-25 size exclusion column and eluted with phosphate buffered saline (PBS, pH 7.6) to afford [ $^{68}\text{Ga}$ ]Ga-NOTA-Siglec-9 in 2.5 mL PBS. The NOTA-Siglec-9 precursor was acquired from Peptide Specialty Laboratories (Heidelberg, Germany) as a custom synthesis.

##### *Radiochemical purity*

Radiochemical purity was determined with HPLC with the following protocol: Jupiter C18 column (5  $\mu\text{m}$ , , 300  $\text{Å}$ , 150  $\times$  4.60 mm; Phenomenex, Torrance, CA, USA); flow rate = 1 mL/min; wavelength  $\lambda$  = 220 nm; solvent A = 0.1% trifluoroacetic acid (TFA) in water; solvent B = 0.1% TFA in acetonitrile (ACN); gradient: 18% B during 0-2 min; from 18% B to 60% B during 2-11 min; from 60% B to 18% B during 11-15 min; 18% B during 15-20 min.

##### *Distribution coefficient (LogD)*

The distribution coefficient (LogD) was measured by adding a small aliquot of labelled tracer into a mixture of PBS (pH 7.6) and 1-octanol (1:1). The solution was mixed thoroughly for 5 min at room temperature. After separation of phases by centrifugation (12,000  $\times$  g, 6 min), aliquots of each phase layer were taken for  $\gamma$ -counting to determine LogD. The test was repeated three times. LogD was calculated as log base 10 of the value from the activity concentration in octanol divided by activity concentration in PBS.

#### 4.1.2 $\text{Al}^{18}\text{F}$ -NOTA-Siglec-9

##### *Radiolabelling*

[ $^{18}\text{F}$ ]Fluoride (42  $\mu\text{L}$  in physiological saline) was transferred to a reaction vial preloaded with 76  $\mu\text{L}$  CH<sub>3</sub>CN and 21  $\mu\text{L}$  AlCl<sub>3</sub> (2 mM in 1.0 M NaOAc, pH 4.0), followed by incubation at RT for 3 minutes. 18  $\mu\text{L}$  propylene glycol and 52.5 nmol NOTA-Siglec-9 dissolved in water (26  $\mu\text{L}$ , 2.02 mM) were added to the reaction vial and the mixture was incubated at 100 °C for 15 minutes. The reaction mixture was cooled to 35 °C and loaded onto an Oasis 30 mg HLB cartridge (Waters, Milford, MA, USA). The cartridge was washed with 7 mL of water and consequently eluted with 0.5 mL of 0.05% formic acid in ethanol directly onto a NAP-5 size exclusion column. The NAP column was eluted with PBS, affording [ $^{18}\text{F}$ ]AlF-NOTA-Siglec-9 in 1 mL PBS.

### *Radiochemical purity and distribution coefficient (LogD)*

Radiochemical purity (RCP) and logD were determined using the protocols described for [<sup>68</sup>Ga]Ga-NOTA-Siglec-9 in Chapter 4.1.1.

### 4.1.3 <sup>68</sup>Ga-DOTA-Siglec-9 (GMP)

#### *Radiolabelling*

Radiosynthesis was performed using a previously described method (Käkelä et al., 2018) with a fully automated synthesis device (Modular Lab PharmTracer; Eckert & Ziegler, Valencia, CA, USA). <sup>68</sup>Ga was eluted from with 6 mL 0.1 M HCl through a strata-XC cation exchange cartridge (Phenomenex, Torrance, CA, USA). [<sup>68</sup>Ga]GaCl<sub>3</sub> was released from the cartridge via elution with 0.8 mL acidified acetone (containing 3.25% 0.02 M HCl) into a reaction vial preloaded with 12 nmol DOTA-Siglec-9 dissolved in water (30 µg, 60 µL) and 2.0 mL of 0.2 M NaOAc buffer (pH 4.0), followed by incubation at 65 °C for 6 minutes. After incubation, the reaction mixture was diluted with 4 mL of physiological saline and loaded onto a SepPak Light C18 cartridge (Waters, Millford, MA, USA). The cartridge was washed with 2 x 8 mL of physiological saline and eluted with 1.3 mL of 70 % ethanol through a nonpyrogenic 0.22 µm filter into a sterile product vial. The product was formulated in physiological saline, affording GMP-grade [<sup>68</sup>Ga]Ga-DOTA-Siglec-9 in a final volume of 10 mL. The GMP-grade DOTA-Siglec-9 precursor was acquired from ABX Advanced Biomedical Compounds (Radeberg, Germany).

#### *Radiochemical purity*

Radiochemical purity was determined with HPLC with the following protocol: Kinetex C18 column (2.6 µm, 100 Å, 75 × 4.6 mm; Phenomenex, Torrance, CA, USA); flow rate = 1 mL/min; wavelength λ = 220 nm; solvent A = 0.16% TFA in water; solvent B = 0.16% TFA in ACN; gradient: from 18% B to 50% B during 0-12 min. The radio-HPLC system consisted of a LC-20A Prominence HPLC System (Shimadzu, Kyoto, Japan) and a Flow-Count radiodetector (Bioscan, Washington, DC, USA). The stability of GMP-grade [<sup>68</sup>Ga]Ga-DOTA-Siglec-9 in its end formulation was tested at RT and analysed using the HPLC protocol described above. The limit for product release radiochemical purity was ≥ 91%.

### 4.1.4 <sup>68</sup>Ga-NOTA-Folate

#### *Radiolabelling*

0.5 mL of [<sup>68</sup>Ga]GaCl<sub>3</sub> in 0.1 M HCl from the highest activity generator fraction was transferred into a reaction vial preloaded with 60 mg HEPES dissolved in 50 µL water. 10 nmol of NOTA-Folate dissolved in water (20 µL, 0.5 mM) was added to the reaction mixture and incubated for 10 minutes at 80 °C. After incubation, the

reaction mixture was cooled and brought to a pH of  $\sim 6.5$  by addition of 55  $\mu\text{L}$  1.0 M sodium hydroxide (NaOH). The produced  $[^{68}\text{Ga}]\text{Ga-NOTA-Folate}$  was used as is without further purification. Alternatively, when using an aged generator or to satisfy an otherwise increased radioactivity demand, the reaction can be done in double volume with a 1.0 mL fraction of  $[^{68}\text{Ga}]\text{GaCl}_3$  eluate. In this case, the volumes and amounts of HEPES, NOTA-Folate precursor and NaOH are also be doubled. The NOTA-Folate precursor was synthesized using previously described methods (Chen et al., 2016) at Professor Philip Low's lab, Purdue University, USA.

### *Radiochemical purity*

Radiochemical purity was determined by HPLC with the following protocol: Jupiter Proteo C18 Column (4 $\mu\text{m}$ , 90  $\text{\AA}$ , 250  $\times$  4.6 mm; Phenomenex, Torrance, CA, USA); flow rate = 1 mL/min; wavelength  $\lambda = 220$  nm; solvent A = 0.1% TFA in water, solvent B = 0.1% TFA in ACN; gradient: from 3% B to 35% B during 0-14 minutes B; from 35% B to 3% B during 14-15 minutes.

Alternatively, radiochemical purity could be determined by instant thin-layer chromatography (iTLC). A 1.0  $\mu\text{L}$  sample of end product was applied to an iTLC-SG strip (Agilent, Santa Clara, CA, USA) and developed with 50 mM citric acid. Unbound  $^{68}\text{Ga}$  migrated up with the mobile phase with a retention factor ( $R_f$ ) of 0.8–1.0, while radiolabelled compound remains at the application point ( $R_f = 0$ ). To measure the unbound and tracer-bound  $^{68}\text{Ga}$  fractions, the strip was cut into two pieces at  $R_f \sim 0.4$  and the pieces measured for radioactivity to calculate RCP.

### *Distribution coefficient (LogD)*

LogD was determined using the protocols in Chapter 4.1.1.

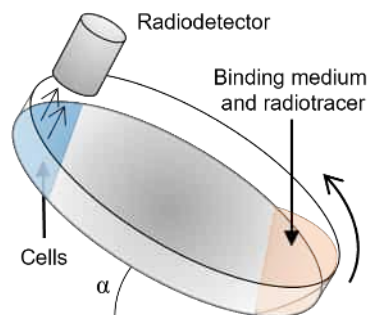
### *FR- $\beta$ binding affinity*

The equilibrium dissociation constant ( $K_D$ ) of  $[^{68}\text{Ga}]\text{Ga-NOTA-Folate}$  towards FR- $\beta$  was determined by analysing radiotracer binding to FR- $\beta$ -positive chinese hamster ovary (CHO-FR- $\beta^+$ ) cells on a LigandTracer Yellow instrument (Ridgeview Instruments AB, Uppsala, Sweden; Figure 18). The CHO cells were cultured on one side of a 92 mm petri dish in a tilted position in Gibco growth medium (Thermo Fisher Scientific, Waltham, MA, USA) supplemented with 10% fetal bovine serum (FBS; Biowest, Nuaille, France) at 37  $^\circ\text{C}$  in a  $\text{CO}_2$  atmosphere. CHO-FR- $\beta^-$  cells were used as a control and the opposite, empty side of the tilted petri dish was used to determine the background signal.

Before the binding experiment, the growth medium was replaced with binding medium (10% fetal bovine serum in Dulbeccos's PBS) followed by incubation at 37  $^\circ\text{C}$  for 30 minutes to starve the cells of Folate.  $[^{68}\text{Ga}]\text{Ga-NOTA-Folate}$  was added stepwise to achieve a concentration range of 1 to 80 nM, followed by replacement with fresh binding medium to determine  $K_D$ . Target region activities (counts per second, CPS) were corrected for background signal and radioactive decay.

Background correction and the  $K_D$  value were calculated using TraceDrawer software (Ridgeview Instruments AB, Uppsala, Sweden).

**Figure 18.** Simplified schematic of the binding assay on the LigandTracer instrument. Radioactivity of the cell region and an empty background region are measured in turns for 30 seconds with a 5 second delay before measurement. This is achieved by rotation of a tilted petri dish. Consecutive rotations and measurements generate a background-normalized radioactivity curve over time.



The presence or absence of FR- $\beta$  on the CHO cells was validated with fluorescence assisted cell sorting (FACS) with both fluorescein isothiocyanate (FITC)-conjugated anti-human FR-  $\beta^+$  mAb (m909; from prof. Philip Low lab) and allophycocyanin (APC)-conjugated anti-human FR-  $\beta^+$  mAb (IgG2a; Biologend, San Diego, CA, USA) and corresponding isotype controls (IgG-FITC and IgG2a; Biologend). Paraformaldehyde-fixed cells were analysed on a Fortessa FACS device (BD, Franklin Lakes, NJ, USA) and Flowing software (Turku Bioscience Cell Imaging and Cytometry Core, Turku, Finland).

#### 4.1.5 $^{89}\text{Zr}$ -DFO-bexmarilimab

##### *DFO-conjugation*

A stock solution of bexmarilimab was reconstituted to a concentration of 3 mg/mL in 1 mL of 1.0 M sodium bicarbonate buffer (pH 9) by ultrafiltration with an Amicon Ultra 60 kDa spin filter (Millipore, Burlington, MA, USA). Subsequently, 10  $\mu\text{L}$  of 5 mM DFO-Bz-NCS (Chematec, Dijon, France) in dimethyl sulfoxide (DMSO) was added and the mixture incubated at 37  $^\circ\text{C}$  for 30 minutes. After incubation, the reaction mixture was loaded onto a PD-10 size exclusion column and eluted with a formulation buffer (10 mM L-histidine/HCl pH 6.0, 20 mM methionine, 280 mM sucrose and 0.02% polysorbate 20 in water) to afford DFO-bexmarilimab in a 1.5 mL final volume. bexmarilimab in stock solution (25 mg/mL mAb in 10 mM L-histidine/HCl pH 6.0, 20 mM L-methionine, 280 mM trehalose and 0.02% polysorbate 20 in water) was acquired from Faron Pharmaceuticals (Turku, Finland).

##### *Radiolabelling*

100  $\mu\text{L}$  of [ $^{89}\text{Zr}$ ]Zr-oxalate (40-45 MBq; BV Cyclotron VU, Amsterdam, The Netherlands) in 1.0 M oxalic acid was combined with 45  $\mu\text{L}$  of 2.0 M  $\text{Na}_2\text{CO}_3$ , 500  $\mu\text{L}$  of 0.5 M HEPES buffer (pH 7.2; Invitrogen, Waltham, MA, USA) and 355  $\mu\text{L}$  of DFO-bexmarilimab in formulation buffer. The resulting mixture was incubated at

RT for 60 minutes and subsequently loaded onto a PD-10 column and eluted with abovementioned buffer to afford [ $^{89}\text{Zr}$ ]Zr-DFO-bexmarilimab in 1.5 – 2.0 mL final volume.

### *Radiochemical purity*

Radiochemical purity was verified with ultrafiltration and sodium dodecyl sulphate polyacrylamide gel electrophoresis (SDS-PAGE). For the ultrafiltration, a small aliquot of end product was added on a Microcon 60 kDa spin filter (Millipore, Burlington, MA, USA) preloaded with 5% DMSO in water and centrifuged for 6 minutes at  $14,000 \times g$  followed by two more washes and subsequent centrifugation of 100  $\mu\text{L}$  5% DMSO in PBS. The filter and filtrate were separately measured for radioactivity. The assay was performed in triplicate and radiochemical purity was determined as radioactivity of the filter divided by total radioactivity and multiplied by 100%.

Native SDS-PAGE was used as a parallel quality control method capable of determining the existence of possible aggregates or larger mAb fragments. The assay was done using precast non-denaturing 4-20% Tris-glycine gels on a Miniprotean PAGE system (Bio-Rad, Hercules, CA, USA). Gels were loaded with a small aliquot of end product in Laemlli sample buffer and run with a constant 250 V voltage. After completing the run, the gels were rinsed with water. A phosphor imaging plate (Fujifilm, Tokyo, Japan) was then exposed to the radioactive gel placed in between to sheets of cling film. Developed plates were scanned on a BAS-5000 analyser (Fujifilm). The produced autoradiograms were analysed on AIDA image analyser (Elysia-Raytest, Straubenhardt, Germany) to determine RCP.

### *Immunoreactivity*

CLEVER-1 affinity of the DFO-bexmarilimab conjugate and [ $^{89}\text{Zr}$ ]Zr-DFO-bexmarilimab (after radioactive decay) were assessed by flow cytometry using the unmodified bexmarilimab antibody as a control. CLEVER-1<sup>+</sup> acute myelogenous leukemia cells (KG-1, CCL-246; ATCC, Manassas, VA, USA) were plated  $0.5 \times 10^6$  cells per well in 96-well plate (Sarstedt, Nümbrecht, Germany) and stained with varying concentrations of bexmarilimab, DFO-bexmarilimab or [ $^{89}\text{Zr}$ ]Zr-DFO-bexmarilimab after radioactive decay. Resulting signals were normalized with an irrelevant isotype control mAb ((S241/L248E)-Alexa Fluor 647; Abzena, Cambridge, UK). Fixed samples were run with an LSRFortessa cell analyzer (Becton Dickinson, Franklin Lakes, NJ, USA) and analyzed with FlowJo10 software (Becton Dickinson).

## 4.2 Radiometabolite analysis

Radiometabolite analysis of plasma samples was conducted using methodologies corresponding to the chemical and physiological characteristics of each

radiopharmaceutical. Plasma for metabolite analysis was stored on ice until analysis and the system used for radio-HPLC analysis consisted of a LaChrom Instruments HPLC system (Hitachi, Tokyo, Japan) and a Radiomatic 150TR flow-through radioisotope detector (Perkin Elmer, Waltham, MA, USA). Individual methods for radiometabolite analysis for each radiotracer are described herein. NOTA-chelated Siglec-9 tracers (Study I) were not analysed for radiometabolites.

#### ***Analysis of [<sup>68</sup>Ga]Ga-DOTA-Siglec-9 radiometabolites***

600 µL of human plasma was vigorously mixed with 600 µL of sulfosalicylic acid to precipitate plasma proteins. Protein-free plasma fractions were obtained by centrifugation at 14 000 g for 3 minutes. The resulting protein-free supernatant was stored on ice until radio-HPLC analysis using the following protocol: semi-preparative Kinetex C18 column (5 µm, 300 Å, 150 × 10 mm; Phenomenex, Torrance, CA, USA); flow rate = 5 mL/min; wavelength λ = 220 nm; solvent A = 0.16% TFA in water; solvent B = 0.16% TFA in ACN; gradient: from 0% B to 50% B during 0-11 min, from 50% B to 100% B during 11-12 min, 100% B during 12-14 min, from 100% B to 0% B during 14-15 min. Analyte volumes of up to 1 mL were used. Protein precipitation of plasma was performed immediately after separation for blood. Standard samples were prepared by addition of a small aliquot of [<sup>68</sup>Ga]Ga-DOTA-Siglec-9 on non-radioactive protein-free human plasma supernatant. The stability of the standard in sulfosalicylic acid-precipitated plasma (stored in ice) was confirmed for up to 5 hours after centrifugation.

#### ***Analysis of [<sup>68</sup>Ga]Ga-NOTA-Folate radiometabolites.***

Mouse or plasma was vigorously mixed with a 1:1 (v/v) volume of 10% sulfosalicylic acid to precipitate plasma proteins, followed by centrifugation at 14000 × g for 2 minutes. The supernatant was analysed using radio-HPLC with the following protocol: semipreparative Jupiter Proteo C18 column (5 µm, 90Å, 250 × 10 mm (Phenomenex, Torrance, CA,USA); flow rate = 5 mL/min; solvent A = 0.1% TFA in water; solvent B = 0.1% TFA in ACN; gradient, 0–11 min from 3% B to 25% B, 11–12 min from 25% B to 100% B, 12–14 min 100% B. Standard samples were prepared by addition of a small aliquot of [<sup>68</sup>Ga]Ga-NOTA-Folate on non-radioactive protein-free rat plasma supernatant.

#### ***Analysis of [<sup>89</sup>Zr]Zr-DFO-bexmarilimab radiometabolites***

Small aliquots of rabbit plasma were applied to native SDS-PAGE to determine the intact [<sup>89</sup>Zr]Zr-DFO-bexmarilimab and metabolite radioactivity fractions of total plasma radioactivity. The assay was conducted as described in Chapter 4.1.5. [<sup>89</sup>Zr]Zr-DFO-bexmarilimab in formulation buffer (stored in 4 °C) was used as a reference.

## 4.3 Preclinical disease models

Approval for animal experiments was granted by the national Project Authorization Board and were carried out in accordance with the European Union directive on the production of animals used for scientific purposes (directive 2010/EU/63).

### Sterile skin inflammation in rats

Male Sprague Daley rats (Central Animal Laboratory, University of Turku, Finland) were subcutaneously injected with 50  $\mu$ L turpentine oil (Sigma Aldrich/Merck, Darmstadt, Germany) into the right foreleg shoulder area. Inflammation in the area was allowed to develop for 24 h prior to PET/imaging. The left shoulder was used as control. In total, 15 rats ( $360 \pm 61$  g) with sterile skin inflammation were studied.

### Atherosclerosis in mice

Atherosclerosis was induced in low-density lipoprotein receptor-deficient mice expressing only apolipoprotein B100 (LDLR<sup>-/-</sup>ApoB<sup>100/100</sup>, strain #003000; Jackson Laboratory, Bar Harbor, ME, USA), which were fed with a high-fat diet containing 21.2 % fat and 0.2% total cholesterol by weight (TD.88137; Envigo, Madison, WI, USA) starting at age of 2 months and continued for 3 to 5 months. C57BL/6JRj mice (Central animal laboratory, University of Turku, Finland) fed a regular diet were used as healthy controls. In total, 17 LDLR<sup>-/-</sup>ApoB<sup>100/100</sup> mice ( $34.7 \pm 5.5$  g) and six healthy control mice ( $29.7 \pm 1.9$  g) were studied.

In addition to the mice, 6 healthy Sprague Dawley rats ( $135.9 \pm 17.1$  g; Central Animal Laboratory, University of Turku, Finland) were used in supplementary experiments.

### Renal fibrosis in rabbits

Renal fibrosis was induced in adult female New Zealand White rabbits (Lidköping kaninfarm, Sweden; Charles River Labs, France; or Envigo, UK) by the unilateral ureteral obstruction (UUO) surgery, where the left ureter was tied off with a non-absorbable suture through a lateral paramedian incision. After surgery, the rabbits were returned to the pen and dosed with 5 mg/kg of enrofloxacin (Bayer, Leverkusen, Germany) and 0.02 mg/kg buprenorphine (RB Pharmaceuticals, Chennai, India) for analgesia during the three days following the surgery. In total, 7 UUO-operated rabbits ( $2054 \pm 198$  g) and 6 healthy control rabbits ( $2203 \pm 158$  g) were studied.

## 4.4 Clinical research subjects

Clinical study protocols for Study II were approved by the Joint Ethics Committee of the University of Turku and Turku University hospital, as well as the Finnish Medicines agency (FIMEA) and the study was registered on ClinicalTrials.Gov (NCT03755245). All participants provided written, informed consent prior to participating in the PET studies. Absence of significant medical, neurologic, and psychiatric history, as well as history of alcohol and drug abuse, were assessed with questionnaires. In addition, a medical history review, routine blood tests, electrocardiography, and a physical exam were performed for each subject. The study was conducted in 6 healthy male volunteers (age  $37 \pm 9$  years) and a male patient (age 29) with newly diagnosed and untreated rheumatoid arthritis (RA). Disease activity in the RA patient was assessed clinically at screening, 4 weeks before the PET studies.

## 4.5 PET study design

### General materials and methods

PET images were analysed by defining and quantifying tracer uptake in appropriate regions of interest (ROI) with Carimas software (Turku PET Centre, Turku, Finland) unless stated otherwise. Radioactivity data, as quantified by PET-imaging or gamma counting, was corrected for radioactive decay to the time of radiotracer injection and presented as standardized uptake values (SUV) unless stated otherwise. SUV was calculated as tissue radioactivity concentration (kBq/g or kBq/mL) and corrected for injected radioactivity dose and animal body weight. Injected radioactivity doses were corrected for residual activities of the dosing syringe and cannula. Results are presented as mean  $\pm$  standard deviation (SD).

Whole blood samples were collected in lithium heparin tubes (Vacuette; Greiner Bio-One, Kremsmünster, Austria, for clinical samples and Microtainer; BD, Franklin Lakes, USA, for preclinical samples). Plasma was separated by centrifugation at  $2100 \times g$  for 5 minutes at 4 °C. Gamma counting of blood, plasma and tissue samples was done on 1480 Wizard (Perkin Elmer, Waltham, MA, USA) or Triathler  $\gamma$ -counters (Hidex, Turku, Finland).

Autoradiography was performed with BAS-TR phosphor imaging plates (Fujifilm, Tokyo, Japan) and a BAS 5000 plate reader (Fujifilm). Histological and immunohistochemically stained tissue sections were scanned with a Panoramic 1000 slide scanner (3DHistotech, Budapest, Hungary).

Statistical significance between data groups was determined with independent samples t-test, unless stated otherwise.



#### 4.5.1 PET study of sterile skin inflammation in rats

##### *PET/CT imaging and ex vivo analysis*

Sprague Dawley rats ( $n = 15$ ) with turpentine-induced sterile skin inflammation were anesthetized with isoflurane and intravenously injected via a tail vein with [ $^{68}\text{Ga}$ ]Ga-NOTA-Siglec-9 or [ $^{18}\text{F}$ ]AlF-NOTA-Siglec-9 with an average injection activity of  $17.7 \pm 3.4$  MBq, followed by 60-minute dynamic PET imaging (timeframes  $6 \times 10$  s,  $4 \times 60$  s,  $5 \times 300$  s, and  $3 \times 600$  s) and *ex vivo* tissue gamma counting (Figure 19). For rats injected with [ $^{68}\text{Ga}$ ]Ga-NOTA-Siglec-9, 4 were subjected to a PET scan and *ex vivo* analysis and 4 additional rats to only *ex vivo* analysis after sacrifice at 60 minutes post-injection. In the case of [ $^{18}\text{F}$ ]AlF-NOTA-Siglec-9, 4 rats were likewise imaged and analysed *ex vivo*, with 3 additional rats again undergoing only *ex vivo* analysis.

Immediately after injection, a 60-minute dynamic PET scan was performed on a High-Resolution Research Tomograph (Siemens, Knoxville, TN, USA). After imaging, the rats were promptly sacrificed and various tissues, most importantly inflamed skin from the right foreleg (inflamed area), skin from the left foreleg (control area) and healthy muscle from the left hind leg were separated, weighed, and measured by gamma counting. PET image data was quantified by defining ROIs on inflamed area, control area, heart, kidneys, liver, and urinary bladder and presented as SUV time-activity curves (TACs). Additionally, plasma protein binding was determined from blood samples collected at sacrifice by acetonitrile precipitation using a previously described protocol (Jensen et al., 2017).

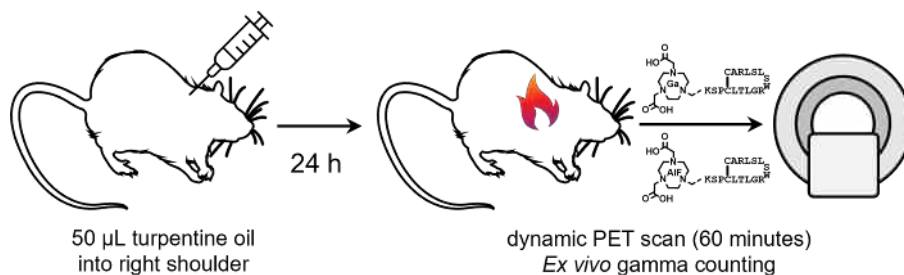


**Figure 19.** PET-imaging of turpentine oil-induced skin inflammation using  $^{68}\text{Ga}$ - and  $^{18}\text{F}$  labelled NOTA-Siglec-9.

#### 4.5.2 First-in-man PET study of $^{68}\text{Ga}$ -DOTA-Siglec-9

##### *PET/CT imaging*

Initially, healthy men ( $n = 6$ ) were studied to determine the whole-body distribution kinetics and radiation dosimetry of intravenously administered [ $^{68}\text{Ga}$ ]Ga-DOTA-Siglec-9. Study subjects were prepared for imaging by inserting catheters into

contralateral antecubital veins for radiotracer injection and blood sampling, respectively. [ $^{68}\text{Ga}$ ]Ga-DOTA-Siglec-9 in saline formulation ( $162 \pm 4$  MBq,  $4.2 \pm 0.9$  mL,  $13.6 \pm 3.0$   $\mu\text{g}$ ) was injected and whole-body PET scanning (Discovery 690 whole-body PET/CT scanner; GE Healthcare, Chicago, IL, USA). PET scans covering the head to mid-thigh area were started at 1, 10, 20, and 40 minutes post-injection, followed by whole-body (head to toes) scans at 100 and 200 minutes post-injection. Volumes of interest (VOI) covering either the whole organ or representative volumes were defined using Hermes software (Hermes Medical Solutions, Stockholm, Sweden). Time-activity information was produced from brain, bone (cortical and trabecular), heart contents (left ventricle), heart wall, kidneys, liver, lungs, muscle, pancreas, red bone marrow, salivary glands, spleen, and urinary bladder.

### ***Assessment of arthritis***

Subsequently, a patient with rheumatoid arthritis was scanned on two consecutive days. On the first day, with preceded by 6 h of fasting, a whole-body FDG PET/CT scan was performed 46 minutes after injection with 198 MBq of [ $^{18}\text{F}$ ]FDG. An immobilization system was used for the hands and wrists to ensure matching positions on the next PET/CT scan. On the second day, the patient was administered 175 MBq of [ $^{68}\text{Ga}$ ]Ga-DOTA-Siglec-9 and a 30-minute dynamic PET/CT scan was performed on the hands, followed by a whole-body PET scan (head to toes). VOIs were defined from the area of 3 inflamed finger joints: proximal interphalangeal joints 2 and 3 and the distal interphalangeal joint 3 on the right hand. TACs were produced [ $^{68}\text{Ga}$ ]Ga-DOTA-Siglec-9 and the SUVs of [ $^{68}\text{Ga}$ ]Ga-DOTA-Siglec-9 and [ $^{18}\text{F}$ ]FDG were compared.

### ***Blood analysis and pharmacokinetics***

During PET/CT imaging, venous blood samples were collected at 2, 3, 5, 7, 10, 15, 20, 30, 60, 90, 180, and 240 minutes after [ $^{68}\text{Ga}$ ]Ga-DOTA-Siglec-9 injection. Whole blood and plasma were weighed, and gamma counted to afford blood pool and plasma TACs. Plasma samples from each timepoint were analysed for intact [ $^{68}\text{Ga}$ ]Ga-DOTA-Siglec-9 and radiometabolite activity fractions as well as plasma protein binding using protocols described in Chapter 4.2. The quantity of soluble VAP-1 (sVAP-1) was analysed from plasma samples taken prior to PET imaging using a previously developed, in-house assay (Aalto et al., 2014). Clinical chemistry analyses were performed on blood and urine samples before and after PET/CT.

Pharmacokinetic parameters for total radioactivity and intact tracer were obtained using monoexponential fitting of the tail and were adjusted for injected radioactivity dose.

### 4.5.3 PET study of atherosclerosis in mice

#### PET/CT imaging and *ex vivo* analysis of atherosclerotic mice

LDLR<sup>-/-</sup>ApoB<sup>100/100</sup> mice (n = 3) with atherosclerosis were intravenously injected with [<sup>18</sup>F]FDG (14.4 ± 0.2 MBq) through the tail vein and subjected to a dynamic 60-minute PET scan on an Inveon small animal PET/CT scanner (Siemens, München, Germany followed by a contrast-enhanced CT scan (100 µL eXIATM160XL; Binitio biomedical, Ottawa, Ontario, Canada). On the following day, the same mice received [<sup>68</sup>Ga]Ga-NOTA-Folate (20.1 ± 1.0 MBq) injections and were imaged under the same conditions with PET and contrast-enhanced CT. PET image ROIs were defined for the myocardium using CT as an anatomical reference. After imaging, the mice were sacrificed, and plasma samples collected at the time of sacrifice (n = 3) were analysed for radiometabolites according to the protocol described in Chapter 4.2.

#### *Autoradiography, histology and immunohistochemistry*

After sacrifice, the aortic arch was excised and processed 20 µm and 8 µm sections as previously described (Silvola et al., 2018). 20 µm sections were promptly exposed to phosphor imaging plates for 3-4 hours before scanning. After scanning, the slides were stained with hematoxylin and eosin (H&E). To allow comparison of ARG uptake between tracers, aortas from 3 additional LDLR<sup>-/-</sup>ApoB<sup>100/100</sup> mice injected with [<sup>18</sup>F]FDG and sacrificed at 60 minutes post-injection were processed as described. The H&E images were used as histological reference to quantify radioactivity uptake from autoradiograms of atherosclerotic plaques and healthy vessel wall on Tina 2.1 software (Raytest, Straubenhardt, Germany). Results were corrected for injected dose, animal weight, exposure time and radioactive decay and expressed as photostimulated fluorescence per area (PSL/mm<sup>2</sup>).

To evaluate colocalization of activated macrophages on atherosclerotic plaques and areas of [<sup>68</sup>Ga]Ga-Folate uptake, 8 µm sections were subjected to macrophage-3 differentiation antigen (Mac-3) staining. The sections were incubated with anti-mouse Mac-3 (1:1000; BD, Franklin Lakes, NJ, USA) and subsequently developed using 3,3'-diaminobenzidine (Bright-DAN, BS04-110; WellMed, Duiven, The Netherlands) and scanned on the slide scanner.

#### *Ex vivo biodistribution*

A separate group of LDLR<sup>-/-</sup>ApoB<sup>100/100</sup> mice (n = 8) and healthy controls (n = 6) were injected with [<sup>68</sup>Ga]Ga-NOTA-Folate (11.3 ± 0.8 MBq). The LDLR<sup>-/-</sup>ApoB<sup>100/100</sup> mice were split into two groups of equal number (n = 4 + 4) and injected with either [<sup>68</sup>Ga]Ga-NOTA-Folate only, or a 100:1 (n/n) co-injection of folate glucosamine and [<sup>68</sup>Ga]Ga-NOTA-Folate for a blocking study. The mice were

sacrificed 60 minutes post-injection and various tissues were excised and gamma counted.

### PET/CT study of healthy rats

To evaluate distribution kinetics in healthy rats, dynamic whole-body PET/CT scans with  $^{68}\text{Ga}$ -NOTA-Folate ( $10.3 \pm 0.4$  MBq) were performed in Healthy Sprague Dawley rats ( $n = 6$ ). 3 rats received injections of [ $^{68}\text{Ga}$ ]Ga-NOTA-Folate only and 3 rats received a 100:1 ( $n/n$ ) co-injection of folate glucosamine. Using CT as an analytical reference, PET image analysis was performed by defining ROIs on the main organs. TACs from the rats injected with only [ $^{68}\text{Ga}$ ]Ga-NOTA-Folate were used to extrapolate human dosimetry. Additionally, plasma samples ( $n = 3$ ) collected at the time of sacrifice were collected and analysed according to the metabolite analysis protocol described in Chapter 4.2.

### 4.5.4 PET study of renal fibrosis in rabbits

UUO-operated and healthy New Zealand White rabbits were prepared for imaging by insertion of two cannulas into two contralateral ear veins for radiotracer dosing and blood sampling, respectively. A Discovery 690 human PET/CT scanner (GE Healthcare, Chigago, IL, USA) was used for imaging.

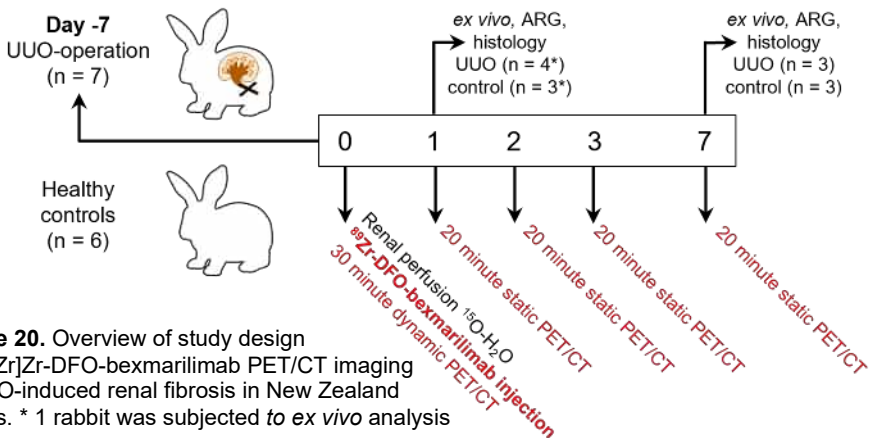


**Figure 20.** Overview of study design for [ $^{89}\text{Zr}$ ]Zr-DFO-bexmarilimab PET/CT imaging of UUO-induced renal fibrosis in New Zealand rabbits. \* 1 rabbit was subjected to ex vivo analysis only.

#### Renal perfusion imaging with $^{15}\text{O}$ -radiowater

Preceding [ $^{89}\text{Zr}$ ]Zr-DFO-bexmarilimab injection, a  $^{15}\text{O}$ -radiowater scan to estimate renal perfusion was performed: 20 MBq of [ $^{15}\text{O}$ ]H $_2$ O was injected via the ear cannula, followed by a 6-minute dynamic PET scan (timeframes:  $15 \times 4$  s,  $4 \times 10$  s,  $4 \times 20$  s,  $3 \times 60$  s). Renal perfusion was estimated by fitting a single tissue

compartmental model to the regional radioactivity concentration curves. Image-derived arterial blood curve from the suprarenal abdominal aorta was used as model input function. The non-linear sum-of-least squares method was used to estimate perfusion (mL blood / mL tissue / min).

### *PET/CT imaging*

Briefly after  $^{15}\text{O}$ -decay, [ $^{89}\text{Zr}$ ]Zr-DFO-bexmarilimab ( $\sim 0.1$  mg/kg,  $7.2 \pm 2.5$  MBq [mean  $\pm$  SD], range 4.4–10.2 MBq,  $3.5 \pm 1.3$  MBq/kg) was injected, and a 30 minute dynamic PET/CT scan ( $4 \times 15$  seconds,  $4 \times 30$  s,  $2 \times 60$  s,  $2 \times 600$  s) was performed, followed by static whole body scans (20 minutes) at 24 hours (1 day), 48 hours (2 days), 72 hours (3 days) and 168 hours (7 days) after injection. ROIs were defined for the whole kidney, renal cortex, liver, spleen and heart left ventricle (LV) using CT as anatomical reference. Additionally, bone (pubic bone) and bone marrow (ilium) ROIs from were defined on healthy rabbit images for dosimetric evaluation.

### *Blood analysis and plasma pharmacokinetics*

Alongside PET/CT imaging, blood samples were collected from an ear vein at 1, 5, 10, 30 min, 1 h, 2 h, 3 h, 4 h post injection on the imaging day, followed by additional samples taken at 1, 2, 3 and 7 days post injection. Samples were analysed for blood and plasma radioactivity as well as [ $^{89}\text{Zr}$ ]Zr-DFO-bexmarilimab radiometabolites as described in Chapter 4.2. Plasma pharmacokinetic parameters (e.g. initial distribution volume ( $V_i$ ), and total clearance ( $Cl_T$ )) were calculated with in-house software (Turku PET Centre) using blood radioactivity concentrations corrected with the fraction of intact [ $^{89}\text{Zr}$ ]Zr-DFO-bexmarilimab in plasma over time for the calculation of pharmacokinetic parameters. The calculation of the parameters is based on the radioactivity concentration at time zero ( $C_0$ ) and area under the curve from zero time to infinity ( $AUC_{0-\infty}$ ), which were determined by fitting a three-term exponential function to the intact tracer fraction-corrected radioactivity-concentration curves.  $V_i$  was calculated as Injected dose/ $C_0$ .  $Cl_T$  was calculated as injected dose/ $AUC$ .

### *Ex vivo biodistribution and autoradiography*

Rabbits were sacrificed at 24 hours (UUO  $n = 4$ , healthy  $n = 3$ ) and 7 days (UUO  $n = 3$ , healthy  $n = 3$ ) post-injection by an overdose of pentobarbital (Mebunat; Orion Pharma, Espoo, Finland) and cardiac puncture. Tissues of interest were promptly excised, weighed and gamma counted. Samples of UUO-operated, contralateral (CL; the un-operated kidney of UUO rabbits) and healthy rabbit kidneys were frozen with dry ice-cooled isopentane in Tissue-Tek (Sakura, Tokyo, Japan) and cut in  $20 \mu\text{m}$  and  $8 \mu\text{m}$  slices, that were promptly thaw-mounted on microscope slides. The  $20 \mu\text{m}$  cryosections and exposed to a phosphor imaging plate for approximately 3 days before scanning. After scanning, the slides were stained with H&E. Using the H&E images as histological reference, uptake in the renal

cortex and medulla areas were quantified from kidney autoradiograms with Carimas software (Turku PET Centre). ARG data was normalized for injected dose, animal weight, and imaging plate exposure time and radioactive decay and presented as PSL/mm<sup>2</sup>. Additionally, 8 µm frozen sections of UUO- and healthy rabbit spleen were prepared for immunohistochemistry, as well as supplementary formalin-fixed, paraffin-embedded 6 µm UUO, CL, and healthy kidney sections, which were later stained with picosirius red to evaluate kidney damage and the development of fibrosis.

### *Immunohistochemistry*

8 µm frozen kidney sections were stained with anti-CLEVER-1 peroxidase staining. (clone 3-372; InVivo Biotech, Hennigsdorf, Germany). The slides were briefly fixed with acetone, blocked with horse serum and incubated at 4°C in a humidified space with 10 µg/mL of 3-372 mAb or an isotype control (irrelevant mouse IgG1 control antibody). The peroxidase signal was developed using the Vectastain Elite ABC kit (Vector Laboratories, Newark, CA, USA) and Liquid Chromogen DAB-substrate (DAKO; Agilent, Santa Clara, CA, USA).

## 4.6 Radiation dosimetry

### *Dosimetry from clinical data.*

Absorbed doses were calculated as suggested in the schema by the committee on medical internal radiation dose of radioactivity of the society of nuclear medicine (MIRD; Bolch et al., 2009). PET/CT-derived time-activity data of source organs was modelled using the sums of exponentials to estimate area-under-curve (AUC) to determine residence times (normalized number of disintegrations displayed in hours) for the source organs. Urinary clearance and biologic half-life were estimated using measurements of urinary void and a voiding interval of 3.5 h was used to calculate urinary bladder wall residence times. Absorbed doses (µGy/MBq) and equivalent doses (µSv/MBq) were calculated from these residence times by the OLINDA/EXM 2.0 software (Hermes Medical Solutions, Stockholm, Sweden) using a 70 kg adult male reference model (Stabin & Siegel, 2018).

### *Estimation of human dosimetry from preclinical data*

Rabbit or rat organ residence times were calculated as described above were converted into corresponding human values with a correction factor derived from average organ weights ( $W_{\text{organ}}$ ) and total body weights ( $W_{\text{TB}}$ ):  $(W_{\text{TB,animal}}/W_{\text{organ,animal}}) \times (W_{\text{organ,human}}/W_{\text{TB,human}})$ . Similar to the above protocol, the body-weight-corrected residence times were inserted to OLINDA/EXM 2.1 using a 70 kg adult male as the reference model (unless stated otherwise) to afford estimated absorbed doses and equivalent dose in humans.

## 5 Results

### 5.1 Radiolabelling and tracer characterization

#### [<sup>68</sup>Ga]Ga- and [<sup>18</sup>F]AIF-NOTA-Siglec-9

The NOTA-chelated Siglec-9 variants [<sup>68</sup>Ga]Ga- and [<sup>18</sup>F]AIF-NOTA-Siglec-9 were produced with 64 % and 39 % RCY, respectively. Radiochemical purities were comparable with averages >98 % for both tracers. Complete radiochemical properties are displayed in Table 6. Notably, the Al<sup>18</sup>F-labelling took 30 minutes longer than <sup>68</sup>Ga-labelling, however, it should be noted that due to the greater start-of-synthesis radioactivity used for <sup>18</sup>F-labelling, the radiosynthesis was done on a remotely controlled device while <sup>68</sup>Ga labelling was done in manual fashion, so the total synthesis times cannot be directly compared.

**Table 6.** Properties of [<sup>68</sup>Ga]Ga- and [<sup>18</sup>F]AIF-NOTA-Siglec-9

	<sup>68</sup> Ga-NOTA-Siglec-9	Al <sup>18</sup> F-NOTA-Siglec-9
<b>Yield (% , n = 3)</b>	53 ± 2 AY; 64 ± 1 RCY	26 ± 3 AY; 39 ± 1 RCY
<b>Radiochemical purity (% , n = 3)</b>	98.5 ± 0.2	98.2 ± 1.4
<b>Molar activity (MBq/nmol , n = 3)</b>	5.0 ± 0.2	8.8 ± 0.9
<b>Total synthesis time (min)</b>	30	60
<b>LogD (n = 3)</b>	-3.2 ± 0.3	-2.3 ± 0.1

Abbreviations: AY – activity yield (non-decay corrected), RCY – radiochemical yield (decay corrected).

#### GMP-grade [<sup>68</sup>Ga]Ga-DOTA-Siglec-9

GMP-compliant radiosynthesis of [<sup>68</sup>Ga]Ga-DOTA-Siglec-9 during Study II was found repeatable with radiochemical purities of 96.0 % ± 1.0 and 97.7 % ± 0.6, as determined by HPLC and iTLC, respectively (n = 3). RCY of 89,7 % ± 2 was reached

with  $43 \pm 8.0$  molar activity % ( $n = 3$ ). The tracer was found stable in end product formulation for 2 hours (later timepoints were not tested).

### $^{68}\text{Ga}$ -NOTA-Folate

$[^{68}\text{Ga}]\text{Ga}$ -NOTA-Folate folate was produced with RCP of  $96.6 \% \pm 2.7$  and  $21.8 \pm 6.9$  MBq/nmol molar activity ( $n = 13$ ). Notably, these results present yields and molar activities achieved over the lifetime of a  $^{68}\text{Ge}/^{68}\text{Ga}$  generator. For example, molar activities of up to 33 MBq/nmol could be reached on a fresh generator, dropping down to 15 MBq/nmol on a generator nearing the end of its 1-year shelf life. The tracer shows high hydrophilicity, with a LogD value of  $-3.28 \pm 0.33$  ( $n = 3$ ).

### $^{89}\text{Zr}$ -DFO-bexmarilimab

The  $^{89}\text{Zr}$ -labelled anti-CLEVER-1 antibody was prepared with high yield and radiochemical yield. In representative batches ( $n = 4$ ),  $[^{89}\text{Zr}]\text{Zr}$ -DFO-bexmarilimab was obtained with RCY of  $78.2 \% \pm 4.2$ , specific radioactivity of  $76.1 \pm 5.1$  MBq/mg and 14.9 MBq/mL radioactivity concentration at the end-of-synthesis. Radiochemical purity was  $99.1 \% \pm 0.3$  as measured by spin filtering and  $\sim 100\%$  as measured by polyacrylamide gel electrophoresis. Immunoreactivity after DFO-conjugation showed  $87.5 \% \pm 2.2$  binding (measured as median fluorescence intensity, FI) compared to unmodified mAb at the lowest measured concentration (1  $\mu\text{g}/\text{mL}$ ; Figure 21B). Immunoreactivity was likewise retained on a batch of  $[^{89}\text{Zr}]\text{Zr}$ -DFO-bexmarilimab re-applied to flow cytometry after radioactive decay (stored in 20 °C for 4 weeks).

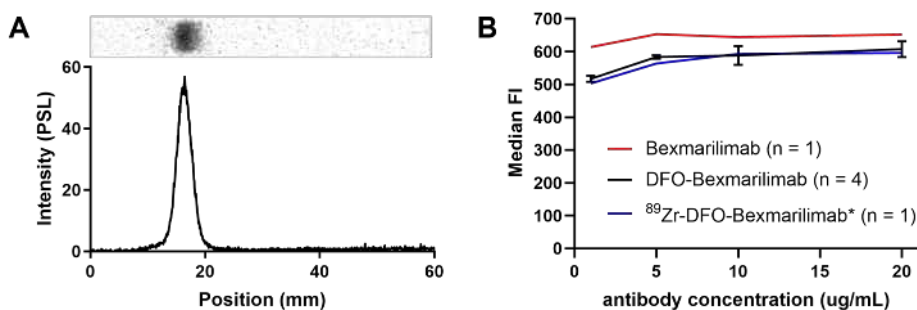


**Figure 21. A:** A representative autoradiogram of SDS-PAGE quality control. **B:** Flow cytometry analysis of DFO-conjugated mAb and  $[^{89}\text{Zr}]\text{Zr}$ -DFO-bexmarilimab. \*measured after radioactive decay.



## 5.2 Preclinical evaluation of $^{68}\text{Ga}$ - and $\text{Al}^{18}\text{F}$ -NOTA-Siglec-9

### 5.2.1 *In vivo* PET imaging

Dynamic PET imaging showed clear uptake of both tracers in the inflamed right shoulder area. The image quality of the two tracers was comparable (Figure 22). For both tracers the majority of radioactivity was excreted through the kidney into urine. Likewise, moderately high uptake was observed in the liver, which is characteristic to other Siglec-9 ligands observed previously. Time activity curves (Figure 23) revealed some differences, with  $^{18}\text{F}$ Al-NOTA-Siglec-9 showing slightly lower uptake in the kidney and higher in the urine, but these differences were not statistically significant.

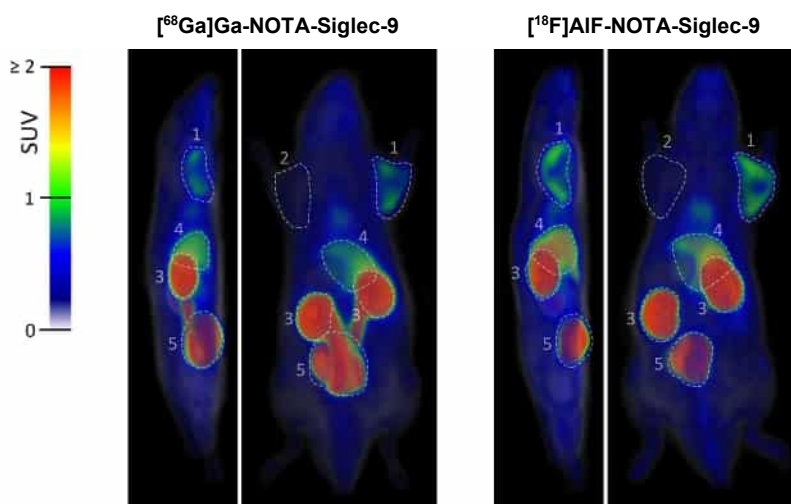


**Figure 22.** A: Sagittal (left panels) and coronal (right panels) maximum intensity projection PET images of  $^{68}\text{Ga}$  and  $^{18}\text{F}$ AlF-NOTA-Siglec-9 biodistribution in rats. The images were averaged from 10 to 60 minute timeframes and normalized to the same SUV. Highlighted ROIs: 1) Inflamed area, 2) control area, 3) kidneys, 4) liver, 5) urinary bladder.

### 5.2.2 *Ex vivo* biodistribution

SUVs acquired by *ex vivo* gamma counting of excised tissues ( $n = 7$ ) were in line with PET image data. Radioactivity of the inflamed area compared to the control area was elevated in both tracers, with  $^{68}\text{Ga}$  showing SUV of  $0.52 \pm 0.12$  in the inflamed area (skin/muscle from the right foreleg shoulder) and  $0.28 \pm 0.09$  in the control area (left hind leg shoulder),  $P = 0.002$ . Respective SUVs for  $^{18}\text{F}$ AlF-NOTA-Siglec-9 were  $0.58 \pm 0.15$  and  $0.28 \pm 0.06$ ,  $P$

< 0.001. Inflamed area-to-control area uptake ratios of  $1.8 \pm 0.3$  for  $[^{68}\text{Ga}]\text{Ga}$ - and  $2.1 \pm 0.2$  for  $[^{18}\text{F}]\text{AIF-NOTA-Siglec-9}$ . Inflamed tissue to muscle ratios were  $10.2 \pm 2.4$  and  $10.4 \pm 1.4$ , respectively. In other tissues, uptake was clearly highest in the kidneys, followed by the liver. Importantly, bone uptake was low for both tracers, at  $0.06 \pm 0.04$  and  $0.06 \pm 0.1$  SUV, respectively, indicating absence of demetallation or defluorination.

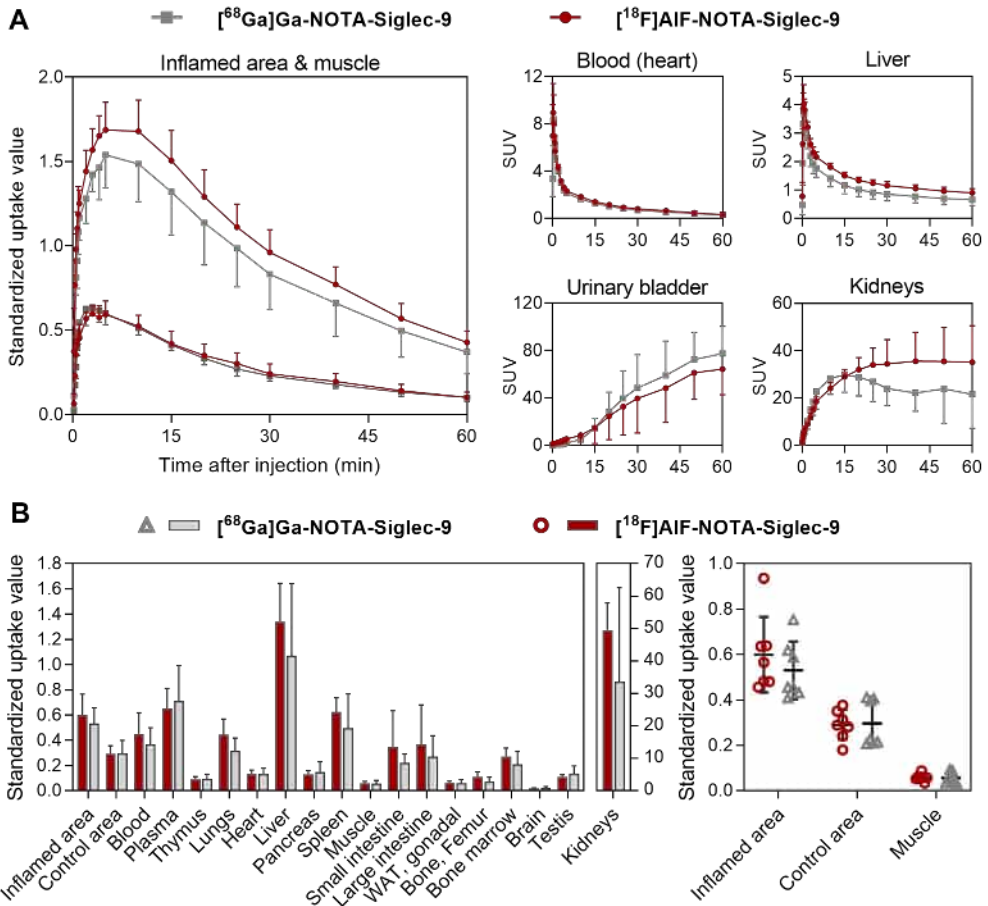


**Figure 23. A)** PET image-derived time-activity curves for  $[^{68}\text{Ga}]\text{Ga}$ - and  $[^{18}\text{F}]\text{AIF-NOTA-Siglec-9}$  ( $n = 4$ ). **B)** Standardized uptake values acquired 60 min post-injection by *ex vivo*  $\gamma$ -counting of excised tissues ( $n = 7$ ). Inflamed area, control area and healthy muscle values are displayed separately.

## 5.3 Clinical evaluation of $^{68}\text{Ga}$ -DOTA-Siglec-9

### 5.3.1 Safety and tolerability

Intravenously injected [ $^{68}\text{Ga}$ ]Ga-NOTA-Siglec-9 was well tolerated in all subjects with no adverse or clinically detectable pharmacologic effects detected at the given dose ( $13.6 \pm 3.0 \mu\text{g}$ ). No changes in vital signs or in the results of clinical chemistry analyses or electrocardiograms were observed. One healthy subject experienced nausea and developed a headache at the end of PET/CT imaging, but upon investigation it was established that the subject had been fasting without water for a long period of time, contrary to instructions.

### 5.3.2 Radioactivity distribution and radiation dose

Whole body PET/CT scan of healthy volunteers showed rapid excretion of [ $^{68}\text{Ga}$ ]Ga-NOTA-Siglec-9 activity through the kidneys into the urinary bladder, where the peak uptake of total injected radioactivity was detected. In general, uptake was consistent across patients, discounting healthy subject, who showed a higher activity in urinary bladder content, reaching a SUV of 242. Out of source organs, the largest residence times were measured in the bladder wall ( $0.33 \pm 0.04 \text{ h}$ ). The average biologic half-life of [ $^{68}\text{Ga}$ ]Ga-DOTA-Siglec-9 (total radioactivity) was  $191 \pm 33 \text{ min}$ .

Not surprisingly, the organs with the highest estimates for absorbed dose were reported in the urinary bladder wall ( $383.2 \pm 48.5 \text{ mGy/MBq}$ ) and kidneys ( $54.4 \pm 14.9 \text{ mGy/MBq}$ ). The mean effective dose, as defined by the International Commission on Radiological Protection (ICPR publication 103) was  $0.022 \text{ mSv/MBq}$ . Based on this data, the estimated radiation dose from 150 MBq of injected [ $^{68}\text{Ga}$ ]Ga-DOTA-Siglec-9 would be  $3.3 \text{ mSv}$ .

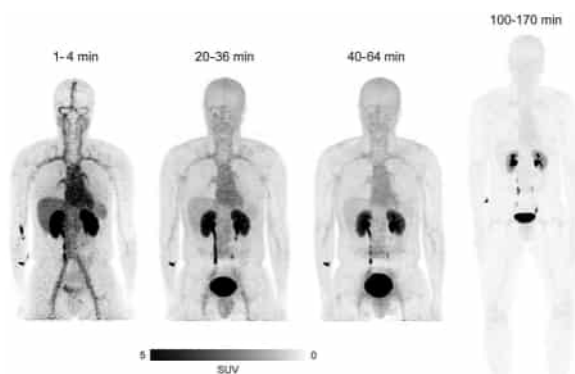


**Figure 24.** Coronal PET images of a healthy volunteer after intravenous injection of [ $^{68}\text{Ga}$ ]Ga-NOTA-Siglec-9. Reprinted with permission (Viitanen et. al. 2020).

### 5.3.3 Assessment of rheumatoid arthritis

A patient with rheumatoid arthritis with a disease activity score of 3.3 in 28 joints, accompanied by tenderness and swelling in 5 joints was included as the 7<sup>th</sup> clinical study subject. Clinical chemistry at time of assessment (4 weeks before imaging) showed positive for rheumatoid factor, anticitrullinated peptide antibodies at >340 U/mL, erythrocyte sedimentation rate at 5 mm/h and C-reactive protein at <1 mg/L. High uptake of both [<sup>18</sup>F]FDG and [<sup>68</sup>Ga]Ga-DOTA-Siglec-9 on were observed on the 2<sup>nd</sup> and 3<sup>rd</sup> proximal interphalangeal joints (PIP2 and PIP3) and the 3<sup>rd</sup> distal interphalangeal joint (DIP3). SUVs in these joints were 1.05, 0.92, and 0.70 for [<sup>68</sup>Ga]Ga-DOTA-Siglec-9 and 1.46, 1.22, and 1.08 for [<sup>18</sup>F]FDG, respectively.



**Figure 25.** [<sup>68</sup>Ga]Ga-DOTA-Siglec-9 and [<sup>18</sup>F]FDG PET/CT images of a RA patient. The PIP2, PIP3 and DIP3 joints have been denoted by arrows. Modified and reprinted with permission (Viitanen et. al. 2020).

### 5.3.4 Metabolism and pharmacokinetics

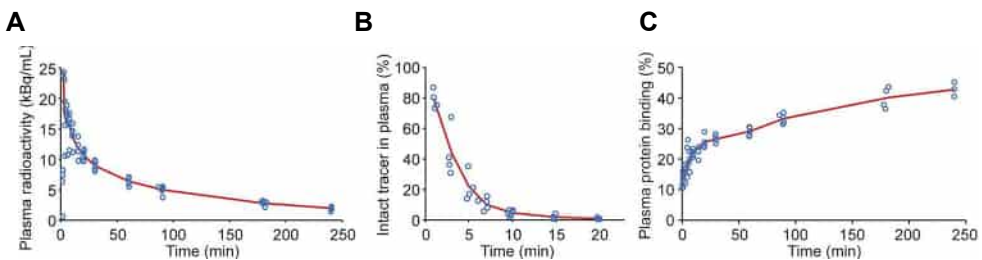


**Figure 26.** A) Total radioactivity concentration, B) the fraction of intact tracer of total radioactivity and C) plasma protein binding as determined from venous blood sampling. Reprinted with permission (Viitanen et. al. 2020).

Upon injection, concentration of radioactivity in venous samples declined rapidly (Figure 26A), and radio-HPLC analysis showed a definitive increase in radiometabolites emerging at early timepoints after injection. The radioactivity

fraction of intact [ $^{68}\text{Ga}$ ]Ga-DOTA-Siglec-9 rapidly declined to  $79.2 \pm 5.3$  % at 1 minutes post-injection, with  $4.3 \pm 1.6$  % remaining after 10 minutes (Figure 26B). Over time, only two major radiometabolite peaks (M-1,  $R_t = 3.2 \pm 0.1$ ; M-2,  $R_t = 4.6 \pm 0.1$  min) endured and only one peak from the metabolite M-2 (identification based on retention time) was detected in urine samples. A detailed representative compilation of metabolite data is presented in Figure 27. Protein binding of radioactivity ranged from 13.3 % briefly after injection to 42.7 % at 240 minutes (Figure 26C).

Pharmacokinetic calculations afforded a mean plasma half-life of total radioactivity of 106.9 minutes with a total clearance value of  $0.18 \pm 0.01$  mL/min. Resulting from the fast metabolic activity of the tracer, the total clearance value for intact [ $^{68}\text{Ga}$ ]Ga-DOTA-Siglec-9 was significantly higher at  $3.3 \pm 1.1$  mL/min.

### Concentration of soluble VAP-1 in circulation

Concentrations and enzymatic activity of soluble VAP-1 (sVAP-1) were measured on the day of [ $^{68}\text{Ga}$ ]Ga-DOTA-Siglec-9 imaging from 4 healthy subjects. Soluble VAP-1 concentrations were found to be  $874.0 \pm 139.9$  ng/mL and enzymatic activity was determined to be  $10.9 \pm 2.2$  nmol/L/h. Blood radioactivity did not correlate with sVAP-1 ( $r = -0.58$ ,  $P = 0.42$ ) concentration or enzymatic activity ( $r = -0.88$ ,  $P = 0.12$ ).

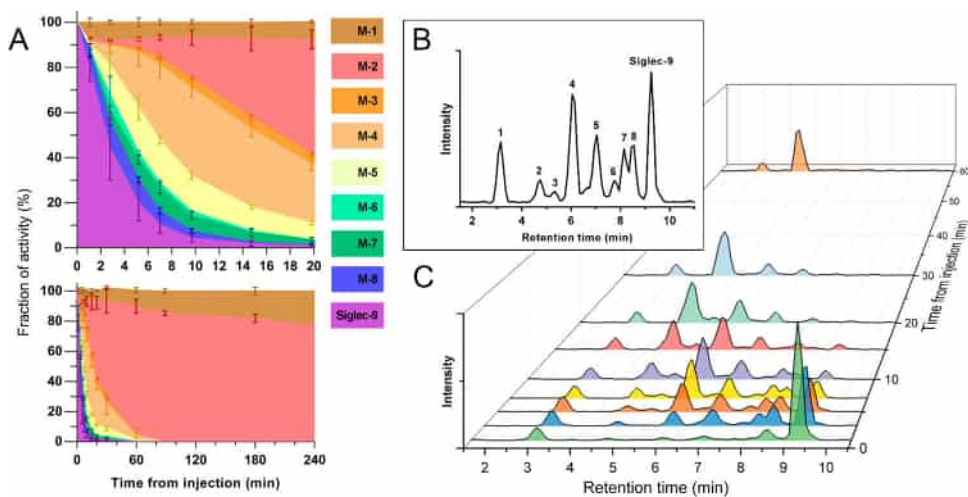


**Figure 27.** **A)** Stacked area plots for average intact [ $^{68}\text{Ga}$ ]Ga-DOTA-Siglec-9 (purple color) fraction and metabolite peak fractions (1-8, other colors) as measured by radio-HPLC. **B)** Representative HPLC chromatogram with metabolite numbers acquired 5 minutes post-injection. **C)** 3D plot for metabolite HPLC chromatograms acquired from a single patient. The retention time of [ $^{68}\text{Ga}$ ]Ga-DOTA-Siglec-9 was  $9.3 \pm 0.1$  min.

## 5.4 Preclinical evaluation of $^{68}\text{Ga}$ -NOTA-Folate

### 5.4.1 Assessment of atherosclerotic lesions

In PET/CT studies of  $\text{LDLR}^{-/-}\text{ApoB}^{100/100}$  mice,  $^{68}\text{Ga}$ ]-Ga-NOTA-Folate displayed significantly lower background myocardial uptake compared to  $^{18}\text{F}$ ]-FDG (SUVs of  $0.43 \pm 0.06$  vs  $10.6 \pm 1.88$ ,  $P = 0.001$ ; Figure 28A&B). Further, autoradiograms of excised aortas showed co-localized uptake with a statistically significant difference in plaque-to-healthy wall uptake ratio in benefit of the folate tracer. Plaque-to-healthy wall ratios were  $2.44 \pm 0.15$  for  $^{68}\text{Ga}$ ]-Ga-NOTA-Folate and  $1.93 \pm 0.22$  for  $^{18}\text{F}$ ]-FDG, respectively ( $P = 0.005$ ; Figure 28C&D). Uptake of both tracers was co-localized in Mac-3-positive macrophage-rich atherosclerotic plaques.

### 5.4.2 *Ex vivo* biodistribution in mice

*Ex vivo* gamma counting analysis of excised tissues collected at 60 minutes post-injection showed higher uptake in the atherosclerotic mouse aorta (SUV  $0.75 \pm 0.12$ ) compared to aortas excised from healthy controls (SUV  $0.41 \pm 0.10$ ,  $P = 0.004$ ). Further, the radioactivity concentration of the atherosclerotic was around three times the background radioactivity in blood (SUV  $0.23 \pm 0.09$ ).

In the remainder of the body, highest radioactivity uptake in both atherosclerotic (SUV  $22.30 \pm 3.28$ ) and healthy mice (SUV  $20.27 \pm 5.48$ ,  $P=0.49$ ) was found in the kidneys, an organ natively expressing FR- $\beta$  (Parker et al., 2005). Kidney uptake was significantly reduced in the folate glucosamine blocking group (SUV  $2.65 \pm 1.80$ ,  $P < 0.001$ ). In the healthy control group, an increased uptake was seen in the lymph nodes (SUV  $4.07 \pm 0.73$ ) compared to the diseased group (SUV  $1.37 \pm 0.57$ ,  $P < 0.001$ ). The blocking group also showed a reduction in uptake (SUV  $0.14 \pm 0.02$ ,  $P = 0.02$ ). In addition to the aorta, kidneys, and lymph nodes, uptake was also decreased significantly ( $P < 0.005$ ) by blocking in the heart, brain, lungs, muscle, pancreas, and stomach. Complete *ex vivo* biodistribution results are presented in supplementary Table 1 (p. 105). The intact radiotracer fraction in  $\text{LDLR}^{-/-}\text{ApoB}^{100/100}$  mouse plasma samples was measured at  $63.5 \% \pm 1.2$  of total plasma radioactivity.

### 5.4.3 *In vivo* distribution kinetics and dosimetry in rats

Like in mice,  $^{68}\text{Ga}$ ]-Ga-NOTA-Folate underwent fast renal excretion, with highest activities observed in kidney, urine, salivary glands, liver, and spleen. Blocking with folate glucosamine clearly lowered uptake in many of these high-uptake tissues, while in turn increasing urine uptake. Plasma metabolite analysis at 60 minutes post-

injection showed intact tracer fractions of  $71.8 \% \pm 1.5$  in healthy rats, and  $88 \% \pm 0.7$  in the blocking group ( $P < 0.001$ ).

Estimates of human dosimetry gave the highest equivalent dose in the kidneys (0.1420 mSv/MBq), with other tissues showing considerably low absorbed doses. The estimated human effective dose (in a 73 kg man) was 0.0105 mSv/MBq.

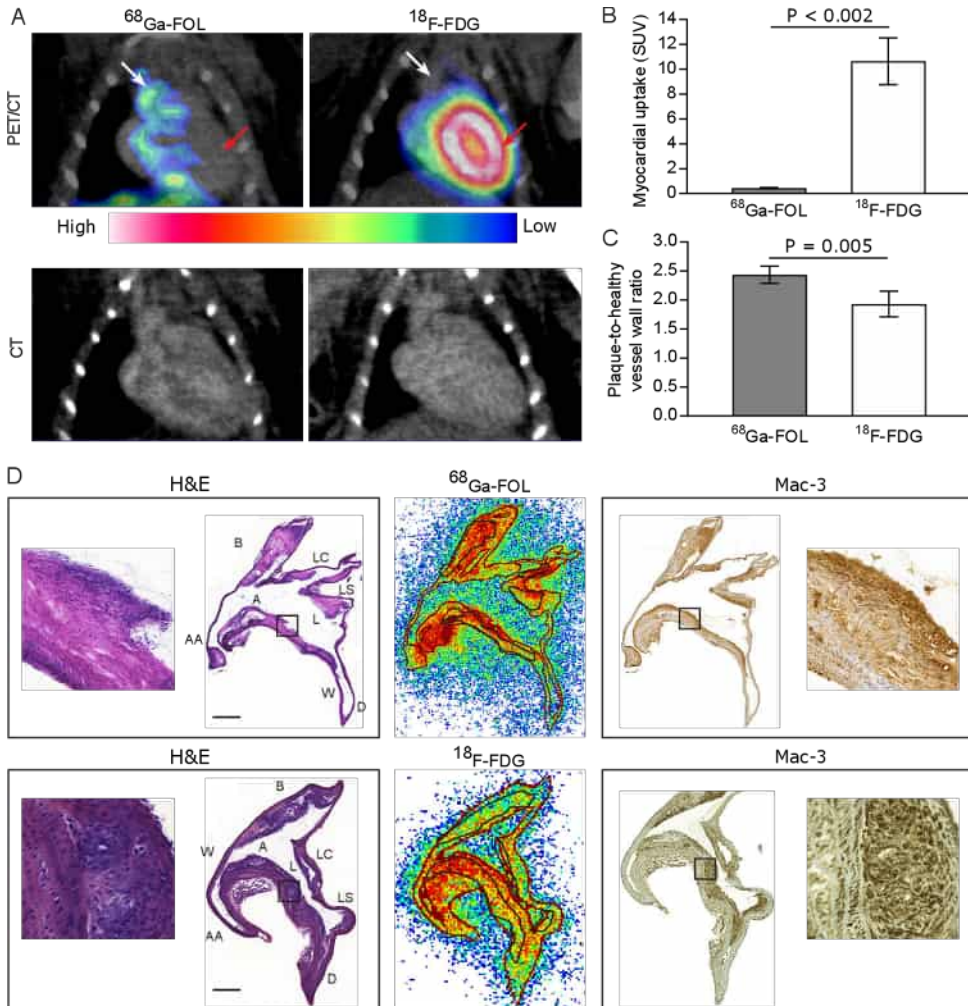


**Figure 28. A)** Coronal PET/CT images of the atherosclerotic heart images with [ $^{68}\text{Ga}$ ]Ga-NOTA-Folate and [ $^{18}\text{F}$ ]FDG **B)** Quantification of myocardial uptake from PET data. **C)** Quantification of ARG data showing a significant difference between the tracers. **D)** representative H&E staining, ARG and Mac-3 IHC in consecutive aortic sections of the same heart. Black rectangles indication representative plaque regions which are shown magnified. Scale bar = 0.5 mm. Abbreviations: A = arch; AA = ascending aorta; B = brachiocephalic artery; D = descending thoracic aorta; L = lesion; LC = left common carotid artery; LS = left subclavian artery; W = wall. Modified and reprinted with permission (Moisio et al., 2020).

#### 5.4.4 *In vitro* binding affinity to FR- $\beta$

Applying [ $^{68}\text{Ga}$ ]Ga-NOTA-Folate to a LigandTracer binding assay with FR- $\beta^+$  Chinese hamster ovary cells produced a  $K_D$  of  $5.1 \pm 1.1$  nM ( $n = 3$ ). No clear accumulation was observed in CHO-FR- $\beta^-$  cells (Figure 29).

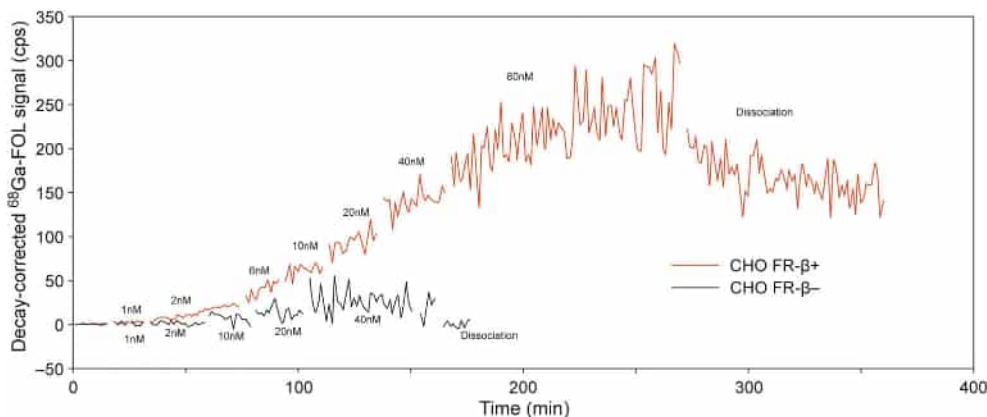


**Figure 29.** Representative real-time, background corrected binding affinity data generated by [ $^{68}\text{Ga}$ ]Ga-NOTA-Folate in a LigandTracer assay of CHO-FR- $\beta^+$  and CHO-FR- $\beta^-$  cells. Modified and reprinted with permission (Moiso et. al. 2020).

## 5.5 Preclinical evaluation of $^{89}\text{Zr}$ -DFO-bexmarilimab

### 5.5.1 Characterisation of the rabbit UO model

Visual and histological inspection of UO-operated kidney demonstrated obvious damage resulting from the blockage of urine flow to the urinary bladder. Coincidentally, the contralateral (CL) right kidney appeared unaffected. Renal perfusion, as determined by [ $^{15}\text{O}$ ]H $_2$ O PET prior to [ $^{89}\text{Zr}$ ]Zr-DFO-bexmarilimab injection, was significantly reduced especially in the UO renal cortex compared to CL and healthy kidneys (Figure 30A). Specifically, compared to the average perfusion of the healthy renal cortex, perfusion was reduced by  $72\% \pm 13$  ( $P < 0.001$ ,  $n = 6$ ) in the UO kidney and  $22\% \pm 2$  ( $P = 0.14$ ,  $n = 6$ ) in the CL kidney cortex. Likewise, the volume of the UO kidney, as determined from CT images, increased significantly due to the operation, while CL and healthy kidney volumes remained comparable (Figure 30B).

Histopathological analysis of H&E-stained kidney sections showed dilated renal tubules, focal injury to epithelial cells and varying histological features indicating inflammation. Pictosirius red showed tubulointerstitial fibrosis in the renal cortex of the UO kidney. Contralateral kidneys from the same rabbits or healthy rabbit kidneys showed no histological abnormalities. Anti-CLEVER-1



immunohistochemical analysis revealed CLEVER-1 positive macrophages in the UUO kidneys, which were not present in the contralateral or healthy kidneys (Figure 30C). H&E and IHC stainings from 7- and 14-day timepoints were comparable (supplementary Figure 1, p.107). A persistent light brown background signal was observed in CL and healthy kidney IHC staining. Anti-CLEVER-1 staining was also performed on kidneys as well as the spleen at 7-days and 14-days after UUO operation, with no discernible differences detected between the two timepoints. A clear anti-CLEVER-1 immunohistochemical signal was detected on the spleen endothelium and resident macrophages.

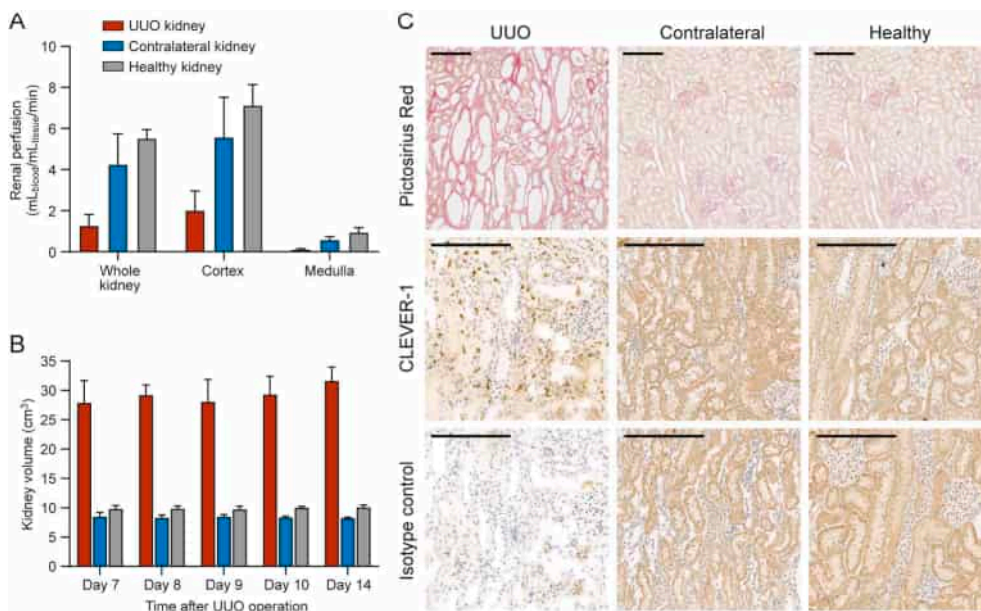


**Figure 30.** **A)** Renal perfusion determined using [<sup>15</sup>O]H<sub>2</sub>O PET/CT at 7 days after UUO operation. UUO and CL n = 6, healthy n = 5. **B)** Kidney volumes for UUO, CL and healthy rabbit kidneys based on CT scans (n = 3). **C)** Representative picrosirius red, anti-CLEVER-1 IHC and isotype control IHC staining from the renal cortex area. Scale bar = 200  $\mu$ m.

### 5.5.2 *In vivo* stability and pharmacokinetics

[<sup>89</sup>Zr]Zr-DFO-bexmarilimab showed relatively rapid clearance from circulation (Figure 31A) with a total radioactivity CL<sub>T</sub> of 10.4  $\pm$  2.1 mL/h (n = 3) in UUO rabbits and 17.4  $\pm$  2.1 mL/h (n = 3, P = 0.03) in healthy rabbits. SDS-PAGE analysis displayed likewise relatively rapid *in vivo* radiometabolism. In UUO rabbits (n = 3), the radioactivity fraction of intact [<sup>89</sup>Zr]Zr-DFO-bexmarilimab decreased from 97.0 %  $\pm$  1.2 of total plasma radioactivity at 4 hours after tracer injection to 33.2 %  $\pm$  3.4 at 3 days post-injection. Almost no intact tracer was shown at the 7-day timepoint, however, we note that plasma radioactivity was too low for accurate measurement.

Healthy rabbit plasma (n = 3) showed  $96.2 \% \pm 0.1$  and  $15.6 \% \pm 4.3$  intact tracer fractions at the same timepoints (Figure 31B). Corrected for intact tracer, the plasma total clearance rates for UUO and healthy rabbits were  $20.4 \pm 1.5$  mL/h and  $35.4 \pm 1.0$  mL/h, respectively ( $P < 0.001$ ). Blood to plasma ratio of radioactivity was determined at an average of did not change appreciably over the 7-day period of imaging.

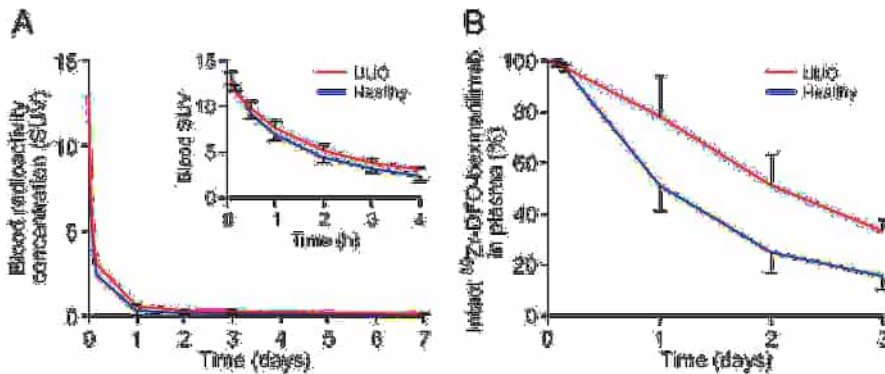


**Figure 31.** **A)** Blood radioactivity concentration (SUV) as measured from venous samples. **B)** Intact tracer fractions of total radioactivity in plasma at different timepoints after injection.

### 5.5.3 *In vivo* PET/CT imaging

In PET/CT images, [ $^{89}\text{Zr}$ ]Zr-DFO-bexmarilimab showed high uptake in both the spleen and liver in both UUO and healthy rabbits over the course of the imaging window of 7 days. At 24 hours post-injection, despite impaired renal perfusion a significantly higher accumulation of radioactivity was observed in the UUO kidney renal cortex compared to the renal cortex of CL and healthy kidneys (Figure 31A&B). A smaller but likewise statistically significant difference was also observed between the CL and healthy renal cortex. When the results were normalized for perfusion (on the premise that radiotracer availability in the tissue is also proportionally hindered) these differences were further pronounced (Figure 32C). In the remainder of the body, elevated tracer uptake was seen in the liver and spleen (Figure 33A&B).

On subsequent days (2, 3 and 7 days post-injection) the activity concentration in the UUO kidney cortex remained practically unchanged, while an increase of uptake overtime was seen in the healthy and contralateral kidneys, with CL cortex uptake surpassing that of the UUO at the 7 days timepoint (Figure 32D). PET images also visualized increased uptake in the bones or bone marrow, especially in the UUO rabbit. Further, some residual uptake was visualized at the intestines, highest at 24 h post-injection and diminishing at later timepoints in both UUO and healthy groups.

Representative sequential PET maximum intensity projection from each day after injection are presented in supplementary Figure 1 (p. 107).

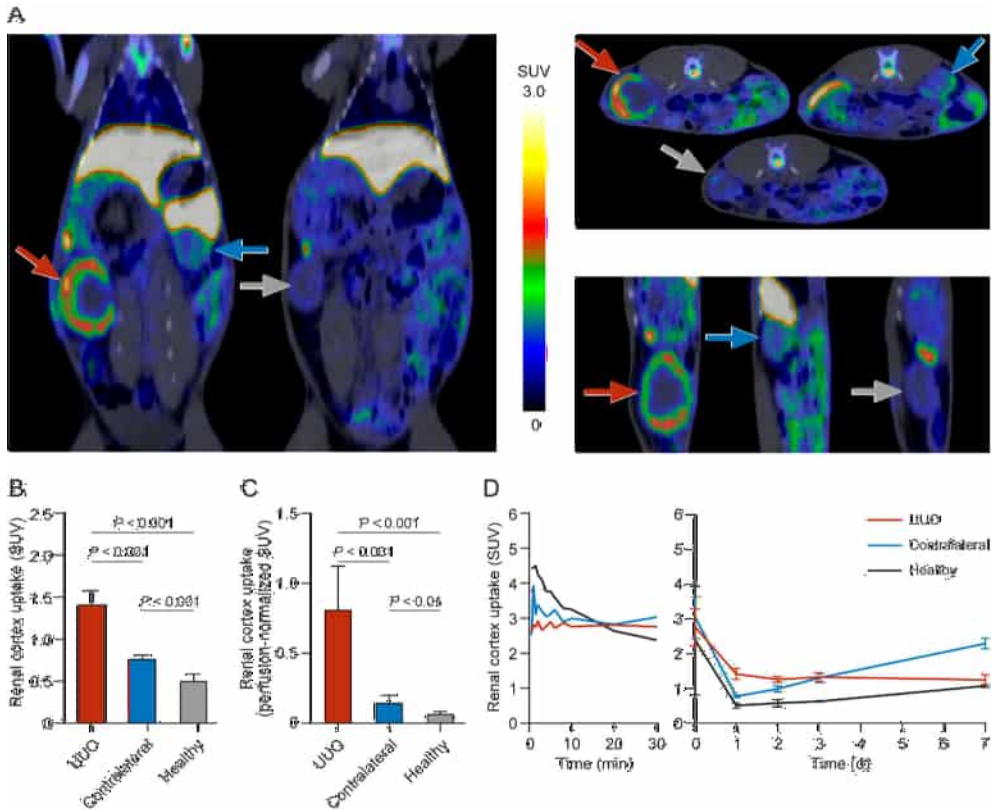


**Figure 32.** **A)** Representative PET/CT images of two rabbits 24 hours after single intravenous injection of [ $^{89}\text{Zr}$ ]Zr-bexmarilimab. Red arrow denotes UJO-operated kidney, blue arrow contralateral kidney, and grey arrow healthy kidney. **B)** Renal cortex SUV at 24h post-injection. **C)** SUV values normalized with renal perfusion. **D)** SUV time-activity curves of renal cortex uptake.

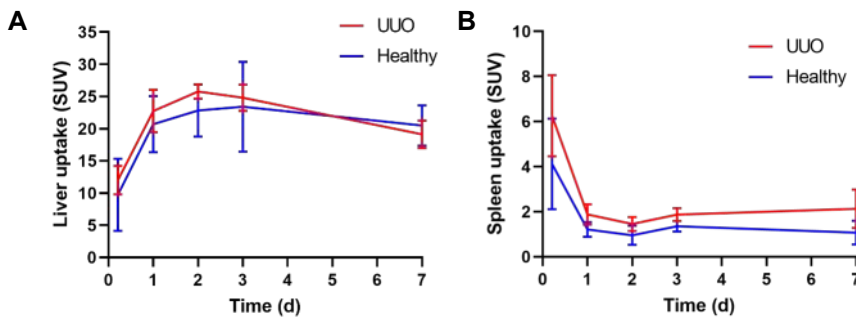


**Figure 33.** SUV time-activity curves for liver (**A**) and spleen (**B**).

### 5.5.4 *Ex vivo* biodistribution and autoradiography

The distribution of uptake observed in PET/CT images was further confirmed by *ex vivo* gamma counting of tissues collected at 24 hours and 7 days post-injection. At 24 hours after [<sup>89</sup>Zr]Zr-DFO-bexmarilimab UUO kidney gamma counting results (SUV  $1.93 \pm 0.05$ ) were significantly higher than the CL (SUV  $1.01 \pm 0.05$ ,  $P < 0.001$ ) and healthy kidneys ( $1.00 \pm 0.11$ ,  $P < 0.001$ ). In the UUO rabbit, bone uptake was quantified at  $0.40 \pm 0.08$  and  $0.81 \pm 11$  at 24 hour and 7 days after injection, respectively. The respective SUV values for the bone marrow were significantly higher at  $1.51 \pm 0.09$  and  $2.39 \pm 0.18$ . Intestinal uptake was shown to be mostly in feces, with empty intestine showing low SUV compared to feces. Complete *ex vivo* biodistribution results are displayed in Supplementary Table 2 (p. 106).

*Ex vivo* autoradiography of kidney sections were in line with PET/CT findings. Additionally, UUO kidney uptake was observed both in the cortex and medulla, while CL and healthy kidneys displayed uptake primarily in the cortex and very little activity (Figure 34).

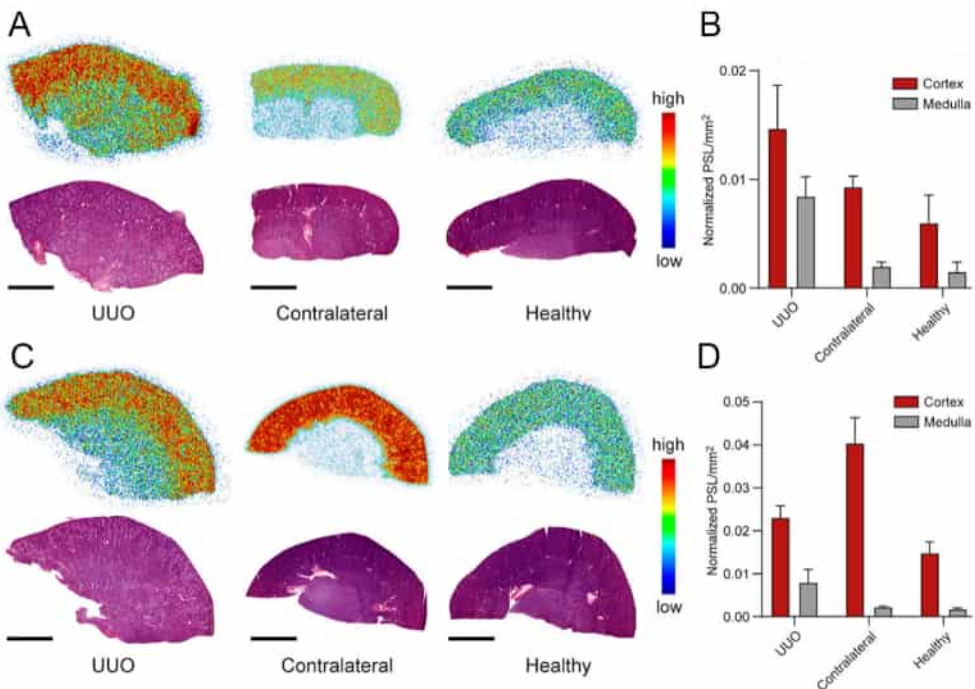


**Figure 34.** Representative digital autoradiographs and H&E staining of neighboring 20  $\mu$ m cryosections and quantification of ARG data from UUO, CL and healthy kidneys at 24 hours (A & B) and 7 days (C & D) after injection. ARG uptake in the cortex and medulla presented in PSL/mm<sup>2</sup>. Scale bar = 5 mm.

### 5.5.5 Estimation of human dosimetry

The equivalent human radiation dose was extrapolated from source organ TACs namely liver, spleen, kidneys, bone and bone marrow, as well as blood and heart (myocardium). The organs with highest absorbed doses extrapolated to a 70-kg male were the liver ( $5.86 \pm 1.10$  mGy/MBq), gall bladder wall ( $2.58 \pm 0.42$  mGy/MBq) and adrenal glands ( $1.777 \pm 0.240$  mGy/MBq). The mean effective dose as defined in ICRP 103, was  $0.70 \pm 0.05$  mSv/MBq. As an example, a 37 MBq intravenously injected dose of [ $^{89}\text{Zr}$ ]Zr-DFO-bexmarlimab would, based on this data, result in an effective dose of 25 mSv.

## 6 Discussion

### 6.1 $^{68}\text{Ga}$ - and $\text{Al}^{18}\text{F}$ -NOTA-Siglec-9 in skin inflammation

The aim of study I was to explore the viability of alternative labelling strategies for the Siglec-9 peptide, with the foremost goal of using the  $^{18}\text{F}$ AlF-method. The results showed that these methods may be considered as good alternatives for producing Siglec-9 peptide radioligands in the future.  $^{68}\text{Ga}$ Ga- and  $^{18}\text{F}$ AlF-NOTA-Siglec-9 were produced in high radiochemical purity and sufficiently high molar activity. Turpentine-induced skin inflammation was clearly visualized, with high inflamed area-to-control area and inflamed area-to-muscle ratios ( $1.8 \pm 0.3$  for  $^{68}\text{Ga}$ Ga- and  $2.1 \pm 0.2$  for  $^{18}\text{F}$ AlF-NOTA-Siglec-9). PET/CT imaging results were confirmed by *ex vivo* gamma counting of tissues collected after sacrifice. Low bone uptake was indicative of the absence of demetallation or defluorination, which may be a concern on some  $^{18}\text{F}$ -labelled ligands. The two tracers showed comparable uptake to each other. Further, biodistribution and uptake in the inflamed area were similar to other Siglec-9 radioligands studied previously in the same disease model, namely  $^{68}\text{Ga}$ Ga-DOTA-Siglec-9 (Aalto et al., 2011; Virtanen et al., 2017). Notably, with the  $^{18}\text{F}$ AlF-method,  $^{18}\text{F}$  can be incorporated on the radiotracer more conveniently compared to earlier use of  $^{18}\text{F}$ fluorodeoxyribose (Li et al., 2013).

Regarding the radiosynthesis protocols presented in this study, some considerations need to be addressed. For  $^{18}\text{F}$ AlF-labelling, the trace metal content of  $^{18}\text{F}$ F<sup>-</sup> is known to have a significant effect on labelling efficiency. In our case, AlF-labelling was conducted on a remotely operated synthesis device used for production of other  $^{18}\text{F}$ -labelled tracers. Although trace-metal reagents and solvents were used for the AlF-protocol, trace metal contamination of the device itself from routine production of other tracers cannot be discounted. As a result, a relatively high 55 nmol precursor loading was necessary to produce sufficiently high yields. Further, size-exclusion chromatography was used to produce the end product in relatively low volume and normalize the end product buffer between  $^{68}\text{Ga}$ Ga- and  $^{18}\text{F}$ AlF-NOTA-Siglec-9. As it is not required to reach sufficient radiochemical purity, the size exclusion step is not necessary in all use cases and reduces radiochemical yields

as a portion of tracer-bound radioactivity is always retained in the size-exclusion columns.

When considering clinical translation, the greater amount of preclinical evidence for successful imaging of inflammatory conditions with the [ $^{68}\text{Ga}$ ]Ga-DOTA-Siglec-9 tracer led to it being the obvious choice for clinical studies.

## 6.2 First-in-man study of $^{68}\text{Ga}$ -DOTA-Siglec-9

The VAP-1 targeting tracer [ $^{68}\text{Ga}$ ]Ga-DOTA-Siglec-9 has shown promise in multiple preclinical models of inflammation, paving way for clinical studies. In Study II, an efficient GMP-compliant radiosynthesis was previously established (Käkelä et al., 2018), allowing us to undercut the planned clinical dose of 40  $\mu\text{g}$  per injection used to establish the absence of acute toxicity in rats *i.v.* injected with the DOTA-Siglec-9 precursor (Chrusciel et al., 2019). In the rat study, a 1000-fold excess of the planned clinical dose was found safe. For reference, the final clinical dose for the study subjects was  $13.6 \pm 3.0$  mg per subject.

Biodistribution and dosimetry analysis afforded an effective dose of 0.022 mSv/MBq, which was found within range of other commonly used  $^{68}\text{Ga}$ -labelled peptides, such as  $^{68}\text{Ga}$ -DOTATOC (0.023 mSv/MBq),  $^{68}\text{Ga}$ -DOTANOC (0.025 mSv/MBq), and  $^{68}\text{Ga}$ -NOTA-RGD (0.022 mSv/MBq). The previously reported mean effective dose extrapolated from rat data was 0.024 mSv/MBq which is within variation of the value we observed in human subjects. However, when looking at the absorbed doses in individual organs, the doses reported for the kidneys and urinary bladder wall were higher in human subjects. Nevertheless, the human radiation exposure was moderate (0.022 mSv/MBq) and allows for multiple scans to be performed on the same patient if needed for longitudinal medical studies.

[ $^{68}\text{Ga}$ ]Ga-DOTA-Siglec-9 showed accumulation on the inflamed finger joints of a patient with rheumatoid arthritis. The tracer showed comparable target-to-background contrast to [ $^{18}\text{F}$ ]FDG in PET images. Perhaps more important for the comparison, the uptake of [ $^{68}\text{Ga}$ ]Ga-DOTA-Siglec-9 should be more specific to inflammation. However promising, it needs to be recognized that single patient data is still anecdotal, and further conclusions should not be drawn. It remains to be seen whether the positive trend continues in a larger patient cohort, and whether the optimization of the [ $^{68}\text{Ga}$ ]Ga-DOTA-Siglec-9 imaging protocol might improve imaging performance. On the otherhand, the study also raised some questions about the *in vivo* stability of the parent tracer in humans.

Following *i.v.* injection, [ $^{68}\text{Ga}$ ]Ga-DOTA-Siglec-9 demonstrated fast renal clearance, which is likely connected to the hydrophilicity, relatively small size of the peptide and the observed metabolic behaviour. In this context, the tracer exhibited fast metabolism, with the intact tracer levels in plasma showing a rapid decrease after

injection. The radioactive metabolites observed in plasma may contribute to kidney and urinary bladder uptake. It is noted that the identities of the detected metabolites are unknown, so definite conclusions about the nature of the metabolites cannot be made. For reference, relatively fast metabolism was observed previously in pigs, with approximately 30% intact [ $^{68}\text{Ga}$ ]Ga-DOTA-Siglec-9 remaining after 60 minutes. In this context, in addition to acting as a VAP-1 ligand, it may be possible that the enzymatic amine oxidase activity of VAP-1/AOC-3 also has a metabolic effect on the Siglec-9 peptide especially at inflamed sites with high VAP-1 expression. That said, based on earlier preclinical studies as well as the patient with RA imaged in this study, the tracers accumulates in the inflamed tissue rapidly with maximum target uptake usually seen within 5 minutes of injection, so the fast metabolism of the tracer may not be a disqualifying factor. Speculatively, it is likewise possible that some of the observed metabolites may retain affinity towards VAP-1.

Regarding the observed fast metabolism of the parent tracer, one possible future avenue of research could be to characterize some of the metabolites observed *in vivo*. Of course, this is not possible through analysis of *in vivo* blood samples during PET imaging, as tracer and metabolite concentrations following in plasma are far too low for meaningful analysis. In this context, it may be viable to produce a set of possible metabolite validation compounds through *in vitro* incubation of the tracer in human plasma or human (or animal) liver homogenates. While *in vitro* behaviour may not directly transfer to *in vivo*, it could prove useful in determining metabolic “soft spots” on the tracer for future improvement. This could allow for a rational starting point for improving stability through peptide backbone modifications, such as incorporation of D- (J. Lu et al., 2020) or  $\beta$ -amino acids (Mortenson et al., 2018).

Nonetheless, further studies in patients with rheumatoid arthritis, vasculitis or pulmonary sarcoidosis are ongoing (Clinicaltrials.gov; NCT03755245), and studies in patients with cancer (NCT05108857) and systemic sclerosis (NCT05108857) have recently been started.

### 6.3 $^{68}\text{Ga}$ -NOTA-Folate visualizes atherosclerotic plaques

In Study III, [ $^{68}\text{Ga}$ ]Ga-NOTA-Folate showed high binding affinity towards human FR- $\beta$ , with  $K_D$  of  $5.1 \pm 1.1$  nM. This is within range compared to previously reported [ $^{18}\text{F}$ ]AIF-NOTA-Folate  $K_D$  of 1.0 nM towards the alpha variant of the folate receptor. In the PET/CT and *ex vivo* studies presented in this work, [ $^{68}\text{Ga}$ ]Ga-NOTA-Folate showed higher plaque-to-healthy wall ratios and lower myocardial uptake compared to [ $^{18}\text{F}$ ]FDG. Likewise, the tracer showed high uptake in tissues known to be FR-



positive in both mice and rat studies, with a significant decrease in activities following blocking with folate glucosamine.

Comparing the result of this study to previously published evaluation of [ $^{18}\text{F}$ ]AIF-NOTA-Folate in the same mouse model of atherosclerosis (Silvola et al., 2018), both PET/CT and *ex vivo* results seemed comparable. Plaque-to-healthy vessel wall ratios were similar ( $2.44 \pm 0.15$  for [ $^{68}\text{Ga}$ ]Ga- and  $2.60 \pm 0.58$  for [ $^{18}\text{F}$ ]AIF-NOTA-Folate). *Ex vivo* uptake in the atherosclerotic aorta was likewise similar ( $2.32 \pm 0.70$  %ID/g vs  $2.4 \pm 0.56$  %ID/g), as was uptake in healthy aorta ( $1.39 \pm 0.45$  %ID/g vs  $1.3 \pm 0.46$  %ID/g). Some difference was however detected in *in vivo* stability, with the  $^{68}\text{Ga}$ -labelled variant showing slightly lower percentage of intact tracer at 60 minutes post-injection ( $63\% \pm 1$  vs  $85\% \pm 6$ ). In any case, conclusions about difference in imaging performance cannot be made based on these studies and the performance of the two tracers was comparable.

As a general observation within our laboratory, we have found the better resolution provided by the  $^{18}\text{F}$  radionuclide in [ $^{18}\text{F}$ ]AIF-NOTA-Folate can be a benefit, especially in rodent studies (Elo et al., 2019; Jahandideh et al., 2020). In the case of the LDLR $^{-/-}$ ApoB $^{100/100}$  mouse model of atherosclerosis used in this study, plaque dimensions are clearly below 1.0 mm, which is under the resolution achieved by typical small animal PET scanners (1.5 mm). The resulting partial volume effects and spillover effects from blood radioactivity, which are compounded by the high positron energy of  $^{68}\text{Ga}$  prevent meaningful quantification directly from PET/CT images. Therefore, most quantification of the aorta and atherosclerotic plaques could not be performed on PET/CT imaged, but was rather achieved with autoradiographs of aortic tissue sections. However, it should be noted that is true for the  $^{18}\text{F}$ -variant as well, as the PET scanner resolution is still a limitation, despite shorter positron range.

The decision of labelling method when larger animals and humans are concerned ultimately depends on other factors, notably radionuclide availability and convenience. This conclusion is similar with [ $^{68}\text{Ga}$ ]Ga- and [ $^{18}\text{F}$ ]AIF-NOTA-Siglec-9. Interestingly, there seems to be an emerging trend of parallel development of  $^{68}\text{Ga}$ - and Al $^{18}\text{F}$ -labelled compounds using the same precursor. An example of this would be the fibroblast activation protein inhibitor FAPI-74, developed by Novartis, with both  $^{68}\text{Ga}$ - and  $^{18}\text{F}$ -labelled variants submitted to clinical evaluation (Giesel et al., 2021). In this case, the  $^{68}\text{Ga}$ -variant was introduced as a cold-kit system for convenience and accessibility, while the Al $^{18}\text{F}$  may be applied to meet increased demand in higher-volume studies or possible future higher-throughput clinical practice. A similar approach to radiopharmaceutical development was recently proposed by Allot and colleagues: conducting initial studies with  $^{68}\text{Ga}$ -labelled radiopharmaceuticals for rapid clinical translation with parallel development of a  $^{18}\text{F}$ -labelled variant allow scalability in the future (Allott et al., 2020). The use of the

NOTA chelator is particularly convenient for this purpose as it allows both  $^{68}\text{Ga}$  and  $^{18}\text{F}$  labelling with the same precursor.

## 6.4 Increased $^{89}\text{Zr}$ -DFO-bexmarilimab uptake in renal fibrosis

In Study IV, DFO was successfully conjugated to bexmarilimab without significant loss of immunoreactivity and labelled with  $^{89}\text{Zr}$ . In general, [ $^{89}\text{Zr}$ ]Zr-DFO-bexmarilimab showed surprisingly fast pharmacokinetic clearance coupled with fast initial uptake in tissues of interest. PET/CT-imaging, *ex vivo* gamma counting of excised tissues and autoradiography analysis of tissue sections increased uptake of radioactivity in the CLEVER-1-positive macrophage-rich UUO kidney, coinciding with lower uptake in the contralateral and healthy rabbit kidneys at 24 hours after i.v. injection with [ $^{89}\text{Zr}$ ]Zr-DFO-bexmarilimab. In general terms, organs showing high or moderate uptake were also tissues that have been previously shown to have physiological CLEVER-1 expression (Kzhyshkowska et al., 2006), namely the liver, spleen, adrenal glands and lymph nodes. CLEVER-1 has been also shown to be expressed on bone marrow sinusoidal endothelial cells (Hansen et al., 2005). However, it should be noted that while uptake of [ $^{89}\text{Zr}$ ]Zr-DFO-bexmarilimab in these tissues clearly coincides with these earlier findings, claims of specificity of said uptake should be avoided as, for example, blocking experiments or broader anti-CLEVER-1 immunohistochemical tissue staining was not conducted in this study. Moderately high uptakes in the gall bladder and feces, especially in healthy rabbits, may be an indication of biliary clearance, which is a possible clearance route for many antibodies (Ovacik & Lin, 2018).

Notably, UUO kidney radioactivity remained stable at later timepoints (3, 4 and 7 days), while the contralateral and healthy kidneys showed an increase in radioactivity uptake towards the 7-day timepoint. While anti-CLEVER-1 IHC confirmed the presence of CLEVER-1<sup>+</sup> macrophages in the UUO kidney, making it a likely target of specific uptake, the kidneys are also a likely route of radiometabolite clearance. Indeed, SDS-PAGE analysis of plasma samples collected from UUO and healthy rabbits showed on average 84% and 67% metabolites of total plasma radioactivity at the 3 days post-injection timepoint, respectively. At the 7-day timepoint, almost no intact [ $^{89}\text{Zr}$ ]Zr-DFO-bexmarilimab was detected, however it is recognized that the activity of samples at that timepoint was too low for accurate measurement. This indicates that the observed increase in kidney uptake at later timepoints is likely an effect of unspecific radiometabolite accumulation. Moreover, the increase in contralateral and healthy kidney uptake coincides with the release of radioactivity from the liver at later timepoints, making the liver a likely source of radiometabolites. Lastly, supporting the hypothesis of unspecific metabolite uptake

at later timepoints, the contralateral kidney showed approximately double uptake at 7-days compared to the healthy kidney. As the contralateral kidney compensates for the loss of function in the UUO kidney, a double metabolite uptake compared to healthy kidney would be expected.

The relatively fast pharmacokinetics and metabolic behaviour of [ $^{89}\text{Zr}$ ]Zr-DFO-bexmarilimab highlight the importance of determining the optimal time window for achieving meaningful results and in the UUO rabbit model, that timepoint was clearly at 24 h. In this context, the kidneys are a challenging target as the site of both specific uptake in the UUO kidney and physiological metabolite uptake in contralateral and healthy kidneys.

In regards to the strengths and weaknesses of this study, although the uptake [ $^{89}\text{Zr}$ ]Zr-DFO-bexmarilimab coincided with immunohistochemical findings, the specificity of uptake to CLEVER-1 positive macrophages, although very likely, remains ultimately unconfirmed. This should be further reinforced in future research by *in vivo* blocking studies or additional *in vitro* studies. Likewise, although the M2 phenotype has been robustly linked to upregulation of CLEVER-1 in previous studies, the identity of macrophages seen in the rabbit UUO kidney were not co-validated with other common M2 markers. Further, the dose-dependency of the tracer was not explored. In this regard, injected mAb dose can have significant effect on pharmacokinetics and target accumulation and may be a factor to optimize in future studies (Dijkers et al., 2010). Regarding the pharmacokinetics observed with [ $^{89}\text{Zr}$ ]Zr-DFO-bexmarilimab (with a 0.1 mg/kg mAb dose), recently published pharmacokinetic data of bexmarilimab in cynomolgus monkeys showed comparable pharmacokinetic parameters with a mAb dose of 3 mg/kg (Hollmén et al., 2022). For future consideration, the already relatively fast clearance of the whole mAb from circulation at low doses could be further hastened by using F(ab')<sub>2</sub> or Fab fragments of bexmarilimab, possibly allowing for a shorter imaging window and the use of radionuclides with a lower radioactivity dose to the imaging subject (e.g.  $^{18}\text{F}$  instead of  $^{89}\text{Zr}$ ).

## 6.5 General study limitations

As an observation, the studies presented are in nature pilot studies: either first-in-human studies or initial investigations of radiopharmaceuticals tested for the first time in a particular disease model. Thus, the amount of research animals used in these studies was low and the resulting statistical power is likewise low. Fortunately, the magnitude of respective differences in uptake or other characteristics seen in target tissues were generally large and *P*-values of < 0.005 were typically observed. Moreover, efforts were made to evaluate the produced data comprehensively, considering whole-body biodistribution, plasma radiometabolites and

pharmacokinetics, as well as observations from earlier studies. Although the use of Student's t-test is widely accepted in the field of preclinical PET, caution should be used when interpreting results based only on claims "statistically significant" or "not statistically significant". Another general limitation is that the effect of molar- or specific activity on target uptake has not been evaluated for these tracers.

## 7 Conclusions

The goal of the work presented herein was to develop and investigate new PET radiopharmaceuticals to visualize inflammation and inflammation-related phenomena based on new biological mechanisms. The tracers studied in this thesis showed increased uptake at intended targets *in vivo*, potentially providing new tools in the future for evaluating disease progression and treatment response in inflammatory diseases where the selected targets, VAP-1, FR-B or CLEVER-1 are of interest. In addition to promising results, avenues for further tracer development, research and optimization of imaging protocols were also recognized.

The primary findings of each study were as follows:

- 1) [ $^{68}\text{Ga}$ ]Ga- and [ $^{18}\text{F}$ ]AlF-NOTA-Siglec-9 showed clear accumulation into the inflamed left shoulder in a rat model of sterile skin inflammation. These tracers can be considered potential alternatives to [ $^{68}\text{Ga}$ ]Ga-DOTA-Siglec-9 (Study I).
- 2) Intravenously injected [ $^{68}\text{Ga}$ ]Ga-DOTA-Siglec-9 was found safe and well tolerated in healthy subjects and importantly, the tracer was able to detect the inflamed finger joints of a patient with rheumatoid arthritis. Further, the estimated radiation dose to humans was moderate and allows for multiple scans on the same subjects (Study II).
- 3) [ $^{68}\text{Ga}$ ]Ga-NOTA-Folate was found to bind to FR- $\beta$  with high affinity and accumulates in M1 macrophage-rich atherosclerotic plaques in a mouse model. Further, the tracer showed a higher plaque-to-healthy vessel wall uptake ratio combined with lower myocardial uptake when compared to [ $^{18}\text{F}$ ]FDG (Study III).
- 4) [ $^{89}\text{Zr}$ ]Zr-DFO-bexmarilimab was produced in high yield and radiochemical purity while retaining immunoreactivity. Significantly increased uptake was observed in fibrotic rabbit kidneys containing resident CLEVER-1 $^{+}$ -macrophages compared to contralateral kidneys in the same rabbits, or the kidneys of healthy rabbits (Study I)

# Acknowledgements

This research was carried out at Turku PET Centre, University of Turku and was financially supported by University of Turku Drug Research Doctoral Programme (DRDP), Sigrid Juselius Foundation, Finnish Cultural foundation, Federal research grant for Turku University Hospital District, Inflammes Research Flagship and Business Finland grants. The thesis was reviewed by Assistant Professor Cecile Philippe from the Medical University of Vienna and Associate Professor Peter J. Scott from the University of Michigan. Your comments and encouraging words were much appreciated and will certainly give me courage in my defence. In this context, I am honored by the acceptance of Professor Jason P. Holland from the university of Zurich to be my esteemed opponent.

My supervisors Professor Anne Roivainen and Assistant Professor Xiang-Guo Li merit great praise for their supportive and emphatic style of guidance. You have always been ready to help no matter the circumstance and for that, I cannot understate my appreciation. Although research has not always been easy, I have never had any regrets joining your research group and that notion has only been reinforced over time.

In addition to Anne and Xiang, my PhD supervisory committee also included Professor Pasi Virta and Professor Sirpa Jalkanen, both academic leaders whom I greatly admire and was honored to involve in my PhD process. I've been working with Pasi already during my bioorganic chemistry undergraduate studies, a time which I remember fondly. I've very much enjoyed visiting your office to chat from time to time, typically not in a professional capacity.

Comprehensive PET studies would not be possible with a team of people whose skills cover the wide ranges of practical and analytical areas needed to conduct quality science. First and foremost, I would like to thank the two supporting pillars without whom I'm sure many of my preclinical studies would have completely collapsed: Heidi Liljenbäck and Aake Honkaniemi. What I may lack in organizational skills, you have definitely compensated for. In this regard Jenni Virta also deserves a separate mention for amazing and untiring contribution and friendship.

I have been assisted and co-authored by countless other investigators. Riikka Viitanen, Petri Elo, Senthil Palani, Emrah Yatkin, Tuula Tolvanen, Vesa Oikonen, Helena Virtanen and Erika Atencio Herre are especially thanked for work of various and significant nature during PET studies. Of course, this list is far from complete, and the contributions of all co-authors is thoroughly appreciated.

A special thanks also goes to all the lab nurses of PET 22<sup>nd</sup> floor lab and especially Sanna Suominen, Heidi Partanen and Eija Salo from whom I've received important and warm-hearted training to get rid of any bad lab habits I'd picked up during the years. I will remember you and my time in the lab very warmly. Likewise, the supporting environment provided by both old and new colleagues and friends in our research group and the PET centre is much appreciated and many of these wonderful people have already been listed as co-authors above. To list everyone, I sincerely thank Andriana Putri, Imran Iqbal, Maria Grönman, Mia Ståhle, Sanna Hellberg, Max Kiugel, Imran Waggan, Miikka Honka, Janne Verho, Kerttu Seppälä, Prince Dadson, Jouni Tuisku, Sanna Laurila, Simona Malaspina, Thomas Keller, Eleni Rebelos, Tania Auchynnika, Milena Monfort-Pires, Priyanka Motiani, Kumail Motiani, Obada Alzghool, Louis Juarez-Orosco and Francisco Acosta for memorable discussions and lovely company. Likewise, the original DRDP student committee crew, Srikar Nagelli, Mitro Miihkinen, Gabrielle Martinez Chacon and Hanne Heikelä are thanked for company as well as organizing many amazing events and get-togethers to make the whole process of getting a PhD more enjoyable. Srikar, thank you inviting me to experience your wedding in India, all the best to you and the family.

Out of all my colleagues at the university, I'd like to specially thank Max Miner and Päivi Marjamäki. Max, I'm happy to consider you a good friend and your likeminded company and humour has made the journey so much more enjoyable. Likewise, having shared an office with Päivi for 4 years was a great pleasure. Both of your contributions to my research work are also appreciated.

I have been blessed to have many amazing friends who have all in their own way contributed to my life as a PhD researcher. The meaning of almost weekly sauna events with my brother Atte Moisio and people I can consider close friends, Juho Ylikylä and Anssi IImanen, cannot be understated and I sincerely thank you for great times, great discussions and letting me always win Terraforming Mars. Narender Joon, thank you for always having time for peer support, discussion, tee or beer at your home, thank you also for cooking me great curries and allowing me to stay with your family in India. My high school friends, Viljami Schleutker, Timo Naskali and Ville Koivuranta already honed my critical thinking skills and interest in science way back when via discussions of science, movies and various, sometimes ridiculous, but interesting arguments on whatever topic came about. Likewise, I truly appreciate my childhood friends Juho Jaakkola and Joni Paavola for continued friendship and

shared life experiences over countless years. There are plenty of additional friends and who in their own way have affect my decision to pursue a PhD and have given me company during it. In no particular order, thank you Hanna-Mari and Kimmo Qvist, Marica Engström, Tero and Hanna Laihinen, Minnea Tuomisto, Mihail Ruotsi, Zoe Allen-Mercier and Cyprian Adamski.

I express my deepest gratitude to everyone who has contributed to this work, both directly and indirectly. This list has not been exhaustive and countless people have been involved in making this research successful, and I could not be more grateful. To be frank, I value the friends and meaningful connections, both existing and new, that I've made during this time more than any career or superficial success.

Lastly a warm thank you to my parents and grandparent, also those who have passed, for support and love throughout my life. I hope to make you proud now and going forward. Finally, most important person during this process and my life in its entirety has been Jasmin. Thank you for being there.

Turku, November 2022

Olli Moisio



# References

- Aalto, K., Autio, A., Kiss, E. A., Elima, K., Nymalm, Y., Veres, T. Z., Marttila-Ichihara, F., Elovaara, H., Saanijoki, T., Crocker, P. R., Maksimow, M., Bligt, E., Salminen, T. A., Salmi, M., Roivainen, A., & Jalkanen, S. (2011). Siglec-9 is a novel leukocyte ligand for vascular adhesion protein-1 and can be used in PET imaging of inflammation and cancer. *Blood*, *118*(13), 3725–3733.
- Aalto, K., Havulinna, A. S., Jalkanen, S., Salomaa, V., & Salmi, M. (2014). Soluble vascular adhesion protein-1 predicts incident major adverse cardiovascular events and improves reclassification in a Finnish prospective cohort study. *Circulation: Cardiovascular Genetics*, *7*(4), 529–535.
- Abou, D. S., Ku, T., & Smith-Jones, P. M. (2011). In vivo biodistribution and accumulation of <sup>89</sup>Zr in mice. *Nuclear Medicine and Biology*, *38*(5), 675–681.
- Ahmed, M., Tegnebratt, T., Tran, T. A., Lu, L., Damberg, P., Gisterå, A., Tarnawski, L., Bone, D., Hedén, U., Eriksson, P., Holmin, S., Gustafsson, B., & Caidahl, K. (2020). Molecular imaging of inflammation in a mouse model of atherosclerosis using a zirconium-89-labeled probe. *International Journal of Nanomedicine*, *15*, 6137–6152.
- Ahtinen, H., Kulkova, J., Lindholm, L., Eerola, E., Hakanen, A. J., Moritz, N., Söderström, M., Saanijoki, T., Jalkanen, S., Roivainen, A., & Aro, H. T. (2014). <sup>68</sup>Ga-DOTA-Siglec-9 PET/CT imaging of peri-implant tissue responses and staphylococcal infections. *EJNMMI Research*, *4*(1), 1–11.
- Alavi, A., & Werner, T. J. (2017). FDG-PET imaging to detect and characterize infectious disorders; an unavoidable path for the foreseeable future. *European Journal of Nuclear Medicine and Molecular Imaging*, *44*(3), 417–420.
- Alizadeh, E., Ahmed, K. B. A., Solomon, V. R., Gaja, V., Bernhard, W., Makhlof, A., Gonzalez, C., Barreto, K., Casaco, A., Geyer, C. R., & Fonge, H. (2021). <sup>89</sup>Zr-labeled domain II-specific scfv-fc immunopet probe for imaging epidermal growth factor receptor in vivo. *Cancers*, *13*(3), 1–16.
- Alizadeh, E., Solomon, V. R., Zuluaga, C., Bernhard, W., Makhlof, A., Barreto, K., Geyer, C., & Fonge, H. (2018). <sup>89</sup>Zr-labeled domain II specific anti-EGFR ScFv-Fc antibody fragment for imaging and monitoring of response to anti-EGFR treatment by PET. *Journal of Nuclear Medicine*, *59*(supplement 1).
- Allott, L., Dubash, S., & Aboagye, E. O. (2020). [<sup>18</sup>F]FET-βAG-TOCA: The design, evaluation and clinical translation of a fluorinated octreotide. *Cancers*, *12*(4), 865.
- Amouroux, G., Pan, J., Jenni, S., Zhang, C., Zhang, Z., Hundal-Jabal, N., Colpo, N., Liu, Z., Bénard, F., & Lin, K. S. (2015). Imaging Bradykinin B1 Receptor with <sup>68</sup>Ga-Labeled [des-Arg<sup>10</sup>]Kallidin Derivatives: Effect of the Linker on Biodistribution and Tumor Uptake. *Molecular Pharmaceutics*, *12*(8), 2879–2888.
- Anzola, L. K., Glaudemans, A. W. J. M., Dierckx, R. A. J. O., Martinez, F. A., Moreno, S., & Signore, A. (2019). Somatostatin receptor imaging by SPECT and PET in patients with chronic inflammatory disorders: a systematic review. *European Journal of Nuclear Medicine and Molecular Imaging*, *46*(12), 2496–2513.
- Archibald, S. J., & Allott, L. (2021). The aluminium-[<sup>18</sup>F]fluoride revolution: simple radiochemistry with a big impact for radiolabelled biomolecules. *EJNMMI Radiopharmacy and Chemistry*, *6*(1), 30.
- Baranski, A. C., Schäfer, M., Bauder-Wüst, U., Wacker, A., Schmidt, J., Liolios, C., Mier, W., Haberkorn, U., Eisenhut, M., Kopka, K., & Eder, M. (2017). Improving the Imaging Contrast of <sup>68</sup>Ga-PSMA-11 by

- Targeted Linker Design: Charged Spacer Moieties Enhance the Pharmacokinetic Properties. *Bioconjugate Chemistry*, 28(9), 2485–2492.
- Bartholomä, M. D. (2012). Recent developments in the design of bifunctional chelators for metal-based radiopharmaceuticals used in Positron Emission Tomography. *Inorganica Chimica Acta*, 389, 36–51.
- Beckers, C., Ribbens, C., André, B., Marcelis, S., Kaye, O., Mathy, L., Kaiser, M.-J., Hustinx, R., Foidart, J., & Malaise, M. G. (2004). Assessment of Disease Activity in Rheumatoid Arthritis with 18F-FDG PET. *Journal of Nuclear Medicine*, 45(6), 956–964.
- Ber, A. J., Pelisek, J., Heider, P., Saraste, A., Reeps, C., Metz, S., Seidl, S., Kessler, H., Wester, H. J., Eckstein, H. H., & Schwaiger, M. (2014). PET/CT imaging of integrin  $\alpha\beta3$  expression in human carotid atherosclerosis. *JACC: Cardiovascular Imaging*, 7(2), 178–187.
- Berg, E., Gill, H., Marik, J., Ogasawara, A., Williams, S., van Dongen, G., Vugts, D., Cherry, S. R., & Tarantal, A. F. (2020). Total-Body PET and Highly Stable Chelators Together Enable Meaningful 89Zr-Antibody PET Studies up to 30 Days After Injection. *Journal of Nuclear Medicine*, 61(3), 453–460.
- Blasi, F., Oliveira, B. L., Rietz, T. A., Rotile, N. J., Day, H., Looby, R. J., Ay, I., & Caravan, P. (2014). Effect of chelate type and radioisotope on the imaging efficacy of 4 fibrin-specific PET probes. *Journal of Nuclear Medicine*, 55(7), 1157–1163.
- Blodgett, T. M., Meltzer, C. C., & Townsend, D. W. (2007). PET/CT: Form and function. *Radiology*, 242(2), 360–385.
- Bolch, W. E., Eckerman, K. F., Sgouros, G., Thomas, S. R., Brill, A. B., Fisher, D. R., Howell, R. W., Meredith, R., & Wessels, B. W. (2009). MIRD pamphlet No. 21: A generalized schema for radiopharmaceutical dosimetry-standardization of nomenclature. *Journal of Nuclear Medicine*, 50(3), 477–484.
- Boros, E., Ferreira, C. L., Cawthray, J. F., Price, E. W., Patrick, B. O., Wester, D. W., Adam, M. J., & Orvig, C. (2010). Acyclic chelate with ideal properties for 68Ga PET imaging agent elaboration. *Journal of the American Chemical Society*, 132(44), 15726–15733.
- Boros, E., Ferreira, C. L., Yapp, D. T. T., Gill, R. K., Price, E. W., Adam, M. J., & Orvig, C. (2012). RGD conjugates of the H2dedpa scaffold: Synthesis, labeling and imaging with 68Ga. *Nuclear Medicine and Biology*, 39(6), 785–794.
- Bouhrel, M. A., Derudas, B., Rigamonti, E., Dièvert, R., Brozek, J., Haulon, S., Zawadzki, C., Jude, B., Torpier, G., Marx, N., Staels, B., & Chinetti-Gbaguidi, G. (2007). PPAR $\gamma$  Activation Primes Human Monocytes into Alternative M2 Macrophages with Anti-inflammatory Properties. *Cell Metabolism*, 6(2), 137–143.
- Bouter, C., Meller, B., Sahlmann, C. O., Staab, W., Wester, H. J., Kropf, S., & Meller, J. (2018). 68 Ga-pentixafor PET/CT imaging of chemokine receptor CXCR4 in chronic infection of the bone: First insights. *Journal of Nuclear Medicine*, 59(2), 320–326.
- Breeman, W. A. P., de Blois, E., Sze Chan, H., Konijnenberg, M., Kwekkeboom, D. J., & Krenning, E. P. (2011). 68Ga-labeled DOTA-peptides and 68Ga-labeled radiopharmaceuticals for positron emission tomography: Current status of research, clinical applications, and future Perspectives. *Seminars in Nuclear Medicine*, 41(4), 314–321.
- Brody, S. L., Gunsten, S. P., Luehmann, H. P., Sultan, D. H., Hoelscher, M., Heo, G. S., Pan, J., Koenitzer, J. R., Lee, E. C., Huang, T., Mpoy, C., Guo, S., Laforest, R., Salter, A., Russell, T. D., Shifren, A., Combadiere, C., Lavine, K. J., Kreisler, D., ... Liu, Y. (2021). Chemokine Receptor 2–targeted Molecular Imaging in Pulmonary Fibrosis. *American Journal of Respiratory and Critical Care Medicine*, 203(1), 78–89.
- Bruce Martin, R. (1996). Ternary complexes of Al $^{3+}$  and F $^{-}$  with a third ligand. *Coordination Chemistry Reviews*, 149, 23–32.
- Burger, C., Goerres, G., Schoenes, S., Buck, A., Lonn, A., & von Schulthess, G. (2002). PET attenuation coefficients from CT images: Experimental evaluation of the transformation of CT into PET 511-keV attenuation coefficients. *European Journal of Nuclear Medicine*, 29(7), 922–927.

- Calais, J., & Mona, C. E. (2021). Will FAPI PET/CT replace FDG PET/CT in the next decade? Point—an important diagnostic, phenotypic, and biomarker role. *American Journal of Roentgenology*, 216(2), 305–306.
- Carrasquillo, J. A., Pandit-Taskar, N., O'Donoghue, J. A., Humm, J. L., Zanzonico, P., Smith-Jones, P. M., Divgi, C. R., Pryma, D. A., Ruan, S., Kemeny, N. E., Fong, Y., Wong, D., Jaggi, J. S., Scheinberg, D. A., Gonen, M., Panageas, K. S., Ritter, G., Jungbluth, A. A., Old, L. J., & Larson, S. M. (2011). 124I-huA33 antibody PET of colorectal cancer. *Journal of Nuclear Medicine*, 52(8), 1173–1180.
- Chen, Q., Meng, X., McQuade, P., Rubins, D., Lin, S. A., Zeng, Z., Haley, H., Miller, P., González Trotter, D., & Low, P. S. (2016). Synthesis and Preclinical Evaluation of Folate-NOTA-Al<sup>18</sup>F for PET Imaging of Folate-Receptor-Positive Tumors. *Molecular Pharmaceutics*, 13(5), 1520–1527.
- Chomet, M., Schreurs, M., Bolijn, M. J., Verlaan, M., Beaino, W., Brown, K., Poot, A. J., Windhorst, A. D., Gill, H., Marik, J., Williams, S., Cowell, J., Gasser, G., Mindt, T. L., van Dongen, G. A. M. S., & Vugts, D. J. (2021). Head-to-head comparison of DFO\* and DFO chelators: selection of the best candidate for clinical <sup>89</sup>Zr-immuno-PET. *European Journal of Nuclear Medicine and Molecular Imaging*, 48(3), 694–707.
- Chrusciel, P., Yarkin, E., Li, X. G., Jaakkola, U. M., Knuuti, J., Jalkanen, S., & Roivainen, A. (2019). Safety Study of Single-Dose Intravenously Administered DOTA-Siglec-9 Peptide in Sprague Dawley Rats. *International Journal of Toxicology*, 38(1), 4–11.
- Cleeren, F., Lecina, J., Ahamed, M., Raes, G., Devoogdt, N., Caveliers, V., McQuade, P., Rubins, D. J., Li, W., Verbruggen, A., Xavier, C., & Bormans, G. (2017). Al<sup>18</sup>F-labeling of heat-sensitive biomolecules for positron emission tomography imaging. *Theranostics*, 7(11), 2924–2939.
- Cleeren, F., Lecina, J., Billaud, E. M. F., Ahamed, M., Verbruggen, A., & Bormans, G. M. (2016). New Chelators for Low Temperature Al<sup>18</sup>F-Labeling of Biomolecules. *Bioconjugate Chemistry*, 27(3), 790–798.
- Coenen, H. H., Gee, A. D., Adam, M., Antoni, G., Cutler, C. S., Fujibayashi, Y., Jeong, J. M., Mach, R. H., Mindt, T. L., Pike, V. W., & Windhorst, A. D. (2017). Consensus nomenclature rules for radiopharmaceutical chemistry — Setting the record straight. *Nuclear Medicine and Biology*, 55, v–xi.
- Conti, M., & Eriksson, L. (2016). Physics of pure and non-pure positron emitters for PET: A review and a discussion. *EJNMMI Physics*, 3(1).
- Coussens, L. M., & Werb, Z. (2002). Inflammation and cancer. *Nature*, 420(6917), 860–867.
- de Winther, M. P. J., van Dijk, K. W., Havekes, L. M., & Hofker, M. H. (2000). Macrophage scavenger receptor class A: A multifunctional receptor in atherosclerosis. *Arteriosclerosis, Thrombosis, and Vascular Biology*, 20(2), 290–297.
- Deng, X., Rong, J., Wang, L., Vasdev, N., Zhang, L., Josephson, L., & Liang, S. H. (2019). Chemistry for Positron Emission Tomography: Recent Advances in <sup>11</sup>C-, <sup>18</sup>F-, <sup>13</sup>N-, and <sup>15</sup>O-Labeling Reactions. *Angewandte Chemie - International Edition*, 58(9), 2580–2605.
- Derlin, T., Gueler, F., Bräsen, J. H., Schmitz, J., Hartung, D., Herrmann, T. R., Ross, T. L., Wacker, F., Wester, H. J., Hiss, M., Haller, H., Bengel, F. M., & Hueper, K. (2017). Integrating MRI and chemokine receptor CXCR4-targeted PET for detection of leukocyte infiltration in complicated urinary tract infections after kidney transplantation. *Journal of Nuclear Medicine*, 58(11), 1831–1837.
- Dietz, M., Kamani, C. H., Deshayes, E., Dunet, V., Mitsakis, P., Coukos, G., Nicod Lalonde, M., Schaefer, N., & Prior, J. O. (2021). Imaging angiogenesis in atherosclerosis in large arteries with +68Ga-NODAGA-RGD PET/CT: relationship with clinical atherosclerotic cardiovascular disease. *EJNMMI Research*, 11(71).
- Dietz, M., Kamani, C. H., Dunet, V., Fournier, S., Rubimbura, V., Testart Dardel, N., Schaefer, A., Jreige, M., Boughdad, S., Nicod Lalonde, M., Schaefer, N., Mewton, N., Prior, J. O., & Treglia, G. (2022). Overview of the RGD-Based PET Agents Use in Patients With Cardiovascular Diseases: A Systematic Review. *Frontiers in Medicine*, 9.
- Dijkers, E. C., Oude Munnink, T. H., Kosterink, J. G., Brouwers, A. H., Jager, P. L., de Jong, J. R., van Dongen, G. A., Schröder, C. P., Lub-de Hooge, M. N., & de Vries, E. G. (2010). Biodistribution of

- +<sup>89</sup>Zr-trastuzumab and PET Imaging of HER2-Positive Lesions in Patients With Metastatic Breast Cancer. *Clinical Pharmacology & Therapeutics*, 87(5), 586–592.
- Disselhorst, J. A., Brom, M., Laverman, P., Slump, C. H., Boerman, O. C., Oyen, W. J. G., Gotthardt, M., & Visser, E. P. (2010). Image-quality assessment for several positron emitters using the NEMA NU 4-2008 standards in the siemens inveon small-animal PET scanner. *Journal of Nuclear Medicine*, 51(4), 610–617.
- Divgi, C. R., Pandit-Taskar, N., Jungbluth, A. A., Reuter, V. E., Gönen, M., Ruan, S., Pierre, C., Nagel, A., Pryma, D. A., Humm, J., Larson, S. M., Old, L. J., & Russo, P. (2007). Preoperative characterisation of clear-cell renal carcinoma using iodine-124-labelled antibody chimeric G250 (<sup>124</sup>I-cG250) and PET in patients with renal masses: a phase I trial. *Lancet Oncology*, 8(4), 304–310.
- Donnelly, D. J. (2020). PET Imaging in Drug Discovery and Development. In *Handbook of Radiopharmaceuticals* (pp. 703–725). Wiley.
- Downer, O. M., Marcus, R. E. G., Zürcher, N. R., & Hooker, J. M. (2020). Tracing the History of the Human Translocator Protein to Recent Neurodegenerative and Psychiatric Imaging. *ACS Chemical Neuroscience*, 11(15), 2192–2200.
- D'Souza, C. A., McBride, W. J., Sharkey, R. M., Todaro, L. J., & Goldenberg, D. M. (2011). High-Yielding Aqueous <sup>18</sup>F-Labeling of Peptides via Al<sup>18</sup>F Chelation. *Bioconjugate Chemistry*, 22(9), 1793–1803.
- Dwyer, F. P., & Mellor, D. P. (1964). Background and fundamental concepts. In *Chelating Agents and Metal Chelates* (pp. 3–5). Elsevier.
- Ebenhan, T., Sathekge, M. M., Lengana, T., Koole, M., Gheysens, O., Govender, T., & Zeevaart, J. R. (2018). <sup>68</sup>Ga-NOTA-functionalized ubiquitin: Cytotoxicity, biodistribution, radiation dosimetry, and first-in-human PET/CT imaging of infections. *Journal of Nuclear Medicine*, 59(2), 334–339.
- Eder, M., Neels, O., Müller, M., Bauder-Wüst, U., Remde, Y., Schäfer, M., Hennrich, U., Eisenhut, M., Afshar-Oromieh, A., Haberkorn, U., & Kopka, K. (2014). Novel Preclinical and Radiopharmaceutical Aspects of [<sup>68</sup>Ga]Ga-PSMA-HBED-CC: A New PET Tracer for Imaging of Prostate Cancer. *Pharmaceuticals*, 7(7), 779–796.
- Eiber, M., Maurer, T., Souvatzoglou, M., Beer, A. J., Ruffani, A., Haller, B., Graner, F. P., Kübler, H., Haberkorn, U., Eisenhut, M., Wester, H. J., Gschwend, J. E., & Schwaiger, M. (2015). Evaluation of hybrid <sup>68</sup>Ga-PSMA ligand PET/CT in 248 patients with biochemical recurrence after radical prostatectomy. *Journal of Nuclear Medicine*, 56(5), 668–674.
- Eigenbrot, C., Ultsch, M., Dubnovitsky, A., Abrahmsén, L., & Härd, T. (2010). Structural basis for high-affinity HER2 receptor binding by an engineered protein. *Proceedings of the National Academy of Sciences of the United States of America*, 107(34), 15039–15044.
- Elo, P., Li, X. G., Liljenbäck, H., Helin, S., Teuvo, J., Koskensalo, K., Saunavaara, V., Marjamäki, P., Oikonen, V., Virta, J., Chen, Q., Low, P. S., Knuuti, J., Jalkanen, S., Airas, L., & Roivainen, A. (2019). Folate receptor-targeted positron emission tomography of experimental autoimmune encephalomyelitis in rats. *Journal of Neuroinflammation*, 16(1).
- Eppard, E., Wuttke, M., Nicodemus, P. L., & Roßch, F. (2014). Ethanol-based post-processing of generator-derived <sup>68</sup>Ga Toward kit-type preparation of <sup>68</sup>Ga-radiopharmaceuticals. *Journal of Nuclear Medicine*, 55(6), 1023–1028.
- Fan, A. P., An, H., Moradi, F., Rosenberg, J., Ishii, Y., Nariai, T., Okazawa, H., & Zaharchuk, G. (2020). Quantification of brain oxygen extraction and metabolism with [<sup>15</sup>O]-gas PET: A technical review in the era of PET/MRI. *NeuroImage*, 220, 117136.
- Fan, A. P., Jahani, H., Holdsworth, S. J., & Zaharchuk, G. (2015). Comparison of cerebral blood flow measurement with [<sup>15</sup>O]-water positron emission tomography and arterial spin labeling magnetic resonance imaging: A systematic review. *Journal of Cerebral Blood Flow and Metabolism*, 36(5), 842–861.
- Fani, M., & Maecke, H. R. (2012). Radiopharmaceutical development of radiolabelled peptides. *European Journal of Nuclear Medicine and Molecular Imaging*, 39(1), 11–30.
- Fani, M., Mansi, R., Nicolas, G. P., & Wild, D. (2022). Radiolabeled Somatostatin Analogs—A Continuously Evolving Class of Radiopharmaceuticals. *Cancers*, 14(5), 1172.

- Feiner, I. V. J., Brandt, M., Cowell, J., Demuth, T., Vugts, D., Gasser, G., & Mindt, T. L. (2021). The Race for Hydroxamate-Based Zirconium-89 Chelators. *Cancers*, *13*(17), 4466
- Gaemperli, O., Shalhoub, J., Owen, D. R. J., Lamare, F., Johansson, S., Fouladi, N., Davies, A. H., Rimoldi, O. E., & Camici, P. G. (2012). Imaging intraplaque inflammation in carotid atherosclerosis with  $^{11}\text{C}$ -PK11195 positron emission tomography/computed tomography. *European Heart Journal*, *33*(15), 1902–1910.
- Ge, L., Fu, Z., Wei, Y., Shi, D., Geng, Y., Fan, H., Zhang, R., Zhang, Y., Li, S., Wang, S., Shi, H., Song, G., Pan, J., Cheng, K., & Wang, L. (2022). Preclinical evaluation and pilot clinical study of [ $^{18}\text{F}$ ]AlF-NOTA-FAPI-04 for PET imaging of rheumatoid arthritis. *European Journal of Nuclear Medicine and Molecular Imaging*, 1–12.
- Gent, Y. Y. J., ter Wee, M. M., Voskuyl, A. E., den Uyl, D., Ahmadi, N., Dowling, C., van Kuijk, C., Hoekstra, O. S., Boers, M., Lems, W. F., & van der Laken, C. J. (2015). Subclinical synovitis detected by macrophage PET, but not MRI, is related to short-term flare of clinical disease activity in early RA patients: An exploratory study. *Arthritis Research and Therapy*, *17*(1).
- Gent, Y. Y. J., Weijers, K., Molthoff, C. F. M., Windhorst, A. D., Huisman, M. C., Smith, D. E. C., Kularatne, S. A., Jansen, G., Low, P. S., Lammertsma, A. A., & van der Laken, C. J. (2013). Evaluation of the novel folate receptor ligand [ $^{18}\text{F}$ ]fluoro-PEG-folate for macrophage targeting in a rat model of arthritis. *Arthritis Research and Therapy*, *15*(2), R37.
- Giesel, F. L., Adeberg, S., Syed, M., Lindner, T., Jiménez-Franco, L. D., Mavriopoulou, E., Staudinger, F., Tonndorf-Martini, E., Regnery, S., Rieken, S., Shafie, R. el, Röhrich, M., Flechsig, P., Kluge, A., Altmann, A., Debus, J., Haberkorn, U., & Kratochwil, C. (2021). FAPI-74 PET/CT using either  $^{18}\text{F}$ -AlF or cold-kit  $^{68}\text{Ga}$  labeling: Biodistribution, radiation dosimetry, and tumor delineation in lung cancer patients. *Journal of Nuclear Medicine*, *62*(2), 201–207.
- Gillis, E. P., Eastman, K. J., Hill, M. D., Donnelly, D. J., & Meanwell, N. A. (2015). Applications of Fluorine in Medicinal Chemistry. *Journal of Medicinal Chemistry*, *58*(21), 8315–8359.
- Gnesin, S., Müller, J., Burger, I. A., Meisel, A., Siano, M., Früh, M., Choschzick, M., Müller, C., Schibli, R., Ametamey, S. M., Kaufmann, P. A., Treyer, V., Prior, J. O., & Schaefer, N. (2020). Radiation dosimetry of  $^{18}\text{F}$ -AzaFol: A first in-human use of a folate receptor PET tracer. *EJNMMI Research*, *10*(1), 32.
- Goerdts, S., Walsh, L. J., Murphy, G. F., & Pober, J. S. (1991). Identification of a novel high molecular weight protein preferentially expressed by sinusoidal endothelial cells in normal human tissues. *Journal of Cell Biology*, *113*(6), 1425–1437.
- Gormsen, L. C., Haraldsen, A., Kramer, S., Dias, A. H., Kim, W. Y., & Borghammer, P. (2016). A dual tracer  $^{68}\text{Ga}$ -DOTANOC PET/CT and  $^{18}\text{F}$ -FDG PET/CT pilot study for detection of cardiac sarcoidosis. *EJNMMI Research*, *6*(1).
- Goud, N. S., Bhattacharya, A., Joshi, R. K., Nagaraj, C., Bharath, R. D., & Kumar, P. (2021). Carbon-11: Radiochemistry and Target-Based PET Molecular Imaging Applications in Oncology, Cardiology, and Neurology. *Journal of Medicinal Chemistry*, *64*(3), 1223–1259.
- Gourni, E., del Pozzo, L., Bartholomä, M., Kiefer, Y., T. Meyer, P., Maecke, H. R., & Holland, J. P. (2017). Radiochemistry and Preclinical PET Imaging of  $^{68}\text{Ga}$ -Desferrioxamine Radiotracers Targeting Prostate-Specific Membrane Antigen. *Molecular Imaging*, *16*, 153601211773701.
- Greten, F. R., & Grivennikov, S. I. (2019). Inflammation and Cancer: Triggers, Mechanisms, and Consequences. *Immunity*, *51*(1), 27–41.
- Grover, V. P. B., Tognarelli, J. M., Crossey, M. M. E., Cox, I. J., Taylor-Robinson, S. D., & McPhail, M. J. W. (2015). Magnetic Resonance Imaging: Principles and Techniques: Lessons for Clinicians. *Journal of Clinical and Experimental Hepatology*, *5*(3), 246–255.
- Guglielmo, P., & Guerra, L. (2021). Radiolabeled fibroblast activation protein inhibitor (FAPI) PET in oncology: has the time come for  $^{18}\text{F}$ -fluorodeoxyglucose to think to a well-deserved retirement? *Clinical and Translational Imaging*, *9*(1), 1–2.
- Guillou, A., Ouadi, A., & Holland, J. P. (2022). Heptadentate chelates for  $^{89}\text{Zr}$ -radiolabelling of monoclonal antibodies. *Inorganic Chemistry Frontiers*, *9*(12), 3071–3081

- Hansen, B., Longati, P., Elvevold, K., Nedredal, G. I., Schledzewski, K., Olsen, R., Falkowski, M., Kzhyshkowska, J., Carlsson, F., Johansson, S., Smedsrød, B., Goerdts, S., Johansson, S., & McCourt, P. (2005). Stabilin-1 and stabilin-2 are both directed into the early endocytic pathway in hepatic sinusoidal endothelium via interactions with clathrin/AP-2, independent of ligand binding. *Experimental Cell Research*, 303(1), 160–173.
- Hellberg, S., Liljenbäck, H., Eskola, O., Morisson-Iveson, V., Morrison, M., Trigg, W., Saukko, P., Ylä-Herttuala, S., Knuuti, J., Saraste, A., & Roivainen, A. (2018). Positron Emission Tomography Imaging of Macrophages in Atherosclerosis with <sup>18</sup>F-GE-180, a Radiotracer for Translocator Protein (TSPO). *Contrast Media and Molecular Imaging*, 2018.
- Hellberg, S., Silvola, J. M. U., Kiugel, M., Liljenbäck, H., Metsälä, O., Viljanen, T., Metso, J., Jauhiainen, M., Saukko, P., Nuutila, P., Ylä-Herttuala, S., Knuuti, J., Roivainen, A., & Saraste, A. (2016). Type 2 diabetes enhances arterial uptake of choline in atherosclerotic mice: An imaging study with positron emission tomography tracer 18F-fluoromethylcholine. *Cardiovascular Diabetology*, 15(1).
- Henrich, U., & Eder, M. (2021). [<sup>68</sup>Ga]Ga-psma-11: The first FDA-approved <sup>68</sup>Ga-radiopharmaceutical for pet imaging of prostate cancer. *Pharmaceuticals*, 14(8).
- Heo, G. S., Kopecky, B., Sultan, D., Ou, M., Feng, G., Bajpai, G., Zhang, X., Luehmann, H., Detering, L., Su, Y., Leuschner, F., Combadière, C., Kreisel, D., Gropler, R. J., Brody, S. L., Liu, Y., & Lavine, K. J. (2019). Molecular Imaging Visualizes Recruitment of Inflammatory Monocytes and Macrophages to the Injured Heart. *Circulation Research*, 124(6), 881–890.
- Herschman, H. R. (2003). Micro-PET imaging and small animal models of disease. *Current Opinion in Immunology*, 15(4), 378–384.
- Herth, M. M., Ametamey, S., Antuganov, D., Bauman, A., Berndt, M., Brooks, A. F., Bormans, G., Choe, Y. S., Gillings, N., Häfeli, U. O., James, M. L., Kopka, K., Kramer, V., Krasikova, R., Madsen, J., Mu, L., Neumaier, B., Piel, M., Rösch, F., ... Zeglis, B. M. (2021). On the consensus nomenclature rules for radiopharmaceutical chemistry – Reconsideration of radiochemical conversion. *Nuclear Medicine and Biology*, 93, 19–21.
- Herzog, B. A., Husmann, L., Valenta, I., Gaemperli, O., Siegrist, P. T., Tay, F. M., Burkhard, N., Wyss, C. A., & Kaufmann, P. A. (2009). Long-Term Prognostic Value of <sup>13</sup>N-Ammonia Myocardial Perfusion Positron Emission Tomography: Added Value of Coronary Flow Reserve. *Journal of the American College of Cardiology*.
- Hicks, R. J., Roselt, P. J., Kallur, K. G., Tothill, R. W., & Mileskin, L. (2021). FAPI PET/CT: Will It End the Hegemony of <sup>18</sup>F-FDG in Oncology? *Journal of Nuclear Medicine: Official Publication, Society of Nuclear Medicine*, 62(3), 296–302.
- Hofman, M., Eu, P., Jackson, P., Hong, E., Binns, D., Irvani, A., Murphy, D., Mitchell, C., Young, J., Hicks, R., Blower, P., & Mullen, G. (2017). Cold Kit PSMA Imaging: First In-Man Study of <sup>68</sup>Ga-THP-PSMA PET/CT in Patients with Prostate Cancer. *Journal of Nuclear Medicine*, 58(supplement 1).
- Hofmann, M., Maecke, H., Börner, A. R., Weckesser, E., Schöffski, P., Oei, M. L., Schumacher, J., Henze, M., Heppeler, A., Meyer, G. J., & Knapp, W. H. (2001). Biokinetics and imaging with the somatostatin receptor PET radioligand <sup>68</sup>Ga-DOTATOC: Preliminary data. *European Journal of Nuclear Medicine*, 28(12), 1751–1757.
- Hollmén, M., Figueiredo, C. R., & Jalkanen, S. (2020). New tools to prevent cancer growth and spread: a ‘Clever’ approach. *British Journal of Cancer*, 123(4), 501–509.
- Hollmén, M., Maksimow, M., Rannikko, J. H., Karvonen, M. K., Vainio, M., Jalkanen, S., Jalkanen, M., & Mandelin, J. (2022). Nonclinical characterization of bexmarilimab, a Clever-1-targeting antibody for supporting immune defense against cancers. *Molecular Cancer Therapeutics*, 21(7), 1207–1218.
- Hyafil, F., Pelisek, J., Laitinen, I., Schottelius, M., Mohring, M., Döring, Y., van der Vorst, E. P. C., Kallmayer, M., Steiger, K., Poschenrieder, A., Notni, J., Fischer, J., Baumgartner, C., Rischpler, C., Nekolla, S. G., Weber, C., Eckstein, H. H., Wester, H. J., & Markus, S. (2017). Imaging the Cytokine Receptor CXCR4 in atherosclerotic plaques with the radiotracer <sup>68</sup>Ga-Pentixafor for PET. *Journal of Nuclear Medicine*, 58(3), 499–506.

- Jaakkola, K., Nikula, T., Holopainen, R., Vahasilta, T., Matikainen, M. T., Laukkanen, M. L., Huupponen, R., Halkola, L., Nieminen, L., Hiltunen, J., Parviainen, S., Clark, M. R., Knuuti, J., Savunen, T., Kaapa, P., Voipio-Pulkki, L. M., & Jalkanen, S. (2000). In vivo detection of vascular adhesion protein-1 in experimental inflammation. *American Journal of Pathology*, *157*(2), 463–471.
- Jackson, J. A., Hungnes, I. N., Ma, M. T., & Rivas, C. (2020). Bioconjugates of Chelators with Peptides and Proteins in Nuclear Medicine: Historical Importance, Current Innovations, and Future Challenges. *Bioconjugate Chemistry*, *31*(3), 483–491.
- Jahandideh, A., Uotila, S., Stähle, M., Virta, J., Li, X. G., Kytö, V., Marjamäki, P., Liljenbäck, H., Taimen, P., Oikonen, V., Lehtonen, J., Mäyränpää, M. I., Chen, Q., Low, P. S., Knuuti, J., Roivainen, A., & Saraste, A. (2020). Folate receptor b–targeted PET imaging of macrophages in autoimmune myocarditis. *Journal of Nuclear Medicine*, *61*(11), 1643–1649.
- Jain, P., Chaney, A. M., Carlson, M. L., Jackson, I. M., Rao, A., & James, M. L. (2020). Neuroinflammation pet imaging: Current opinion and future directions. *Journal of Nuclear Medicine*, *61*(8), 1107–1112.
- Jalkanen, S., Karikoski, M., Mercier, N., Koskinen, K., Henttinen, T., Elima, K., Salmivirta, K., & Salmi, M. (2007). The oxidase activity of vascular adhesion protein-1 (VAP-1) induces endothelial E- and P-selectins and leukocyte binding. *Blood*, *110*(6), 1864–1870.
- Jenkins, W. S. A., Vesey, A. T., Stirrat, C., Connell, M., Lucatelli, C., Neale, A., Moles, C., Vickers, A., Fletcher, A., Pawade, T., Wilson, I., Rudd, J. H. F., van Beek, E. J. R., Mirsadraee, S., Dweck, M. R., & Newby, D. E. (2017). Cardiac  $\alpha v \beta_3$  integrin expression following acute myocardial infarction in humans. *Heart*, *103*(8), 607–615.
- Jenkins, W. S., Vesey, A. T., Vickers, A., Neale, A., Moles, C., Connell, M., Joshi, N. V., Lucatelli, C., Fletcher, A. M., Spratt, J. C., Mirsadraee, S., van Beek, E. J. R., Rudd, J. H. F., Newby, D. E., & Dweck, M. R. (2019). In vivo  $\alpha$ -V beta-3 integrin expression in human aortic atherosclerosis. *Heart*, *105*(24).
- Jensen, S. B., Käkälä, M., Jødal, L., Moisio, O., Alstrup, A. K. O., Jalkanen, S., & Roivainen, A. (2017). Exploring the radiosynthesis and in vitro characteristics of [ $^{68}\text{Ga}$ ]Ga-DOTA-Siglec-9. *Journal of Labelled Compounds and Radiopharmaceuticals*, *60*(9), 439–449.
- Jødal, L., Roivainen, A., Oikonen, V., Jalkanen, S., Hansen, S. B., Afzelius, P., Alstrup, A. K. O., Nielsen, O. L., & Jensen, S. B. (2019). Kinetic modelling of [ $^{68}\text{Ga}$ ]Ga-DOTA-siglec-9 in porcine osteomyelitis and soft tissue infections. *Molecules*, *24*(22).
- Judenhofer, M. S., Wehrli, H. F., Newport, D. F., Catana, C., Siegel, S. B., Becker, M., Thielscher, A., Kneilling, M., Lichy, M. P., Eichner, M., Klingel, K., Reischl, G., Widmaier, S., Röcken, M., Nutt, R. E., Machulla, H. J., Uludag, K., Cherry, S. R., Claussen, C. D., & Pichler, B. J. (2008). Simultaneous PET-MRI: A new approach for functional and morphological imaging. *Nature Medicine*, *14*(4), 459–465.
- Käkälä, M., Luoto, P., Viljanen, T., Virtanen, H., Liljenbäck, H., Jalkanen, S., Knuuti, J., Roivainen, A., & Li, X. G. (2018). Adventures in radiosynthesis of clinical grade [ $^{68}\text{Ga}$ ]Ga-DOTA-Siglec-9. *RSC Advances*, *8*(15), 8051–8056.
- Karikoski, M., Irjala, H., Maksimow, M., Miiluniemi, M., Granfors, K., Hernesniemi, S., Elima, K., Moldenhauer, G., Schledzewski, K., Kzhyshkowska, J., Goerdts, S., Salmi, M., & Jalkanen, S. (2009). Clever-1/Stabilin-1 regulates lymphocyte migration within lymphatics and leukocyte entrance to sites of inflammation. *European Journal of Immunology*, *39*(12), 3477–3487.
- Khalil, M. M., Tremoleda, J. L., Bayomy, T. B., & Gsell, W. (2011). Molecular SPECT Imaging: An Overview. *International Journal of Molecular Imaging*, *2011*, 1–15.
- Kim, E. J., Kim, S., Seo, H. S., Lee, Y. J., Eo, J. S., Jeong, J. M., Lee, B., Kim, J. Y., Park, Y. M., & Jeong, M. (2016). Novel PET imaging of atherosclerosis with  $^{68}\text{Ga}$ -Labeled NOTA-Neomannosylated human serum albumin. *Journal of Nuclear Medicine*, *57*(11), 1792–1797.
- Kim, Y. S., Yang, C. T., Wang, J., Wang, L., Li, Z. B., Chen, X., & Liu, S. (2008). Effects of targeting moiety, linker, bifunctional chelator, and molecular charge on biological properties of  $^{64}\text{Cu}$ -labeled triphenylphosphonium cations. *Journal of Medicinal Chemistry*, *51*(10), 2971–2984.
- Kircher, M., Tran-Gia, J., Kemmer, L., Zhang, X., Schirbel, A., Werner, R. A., Buck, A. K., Wester, H. J., Hacker, M., Lapa, C., & Li, X. (2020). Imaging Inflammation in Atherosclerosis with CXCR4-Directed

- <sup>68</sup>Ga-Pentixafor PET/CT: Correlation with 18F-FDG PET/CT. *Journal of Nuclear Medicine : Official Publication, Society of Nuclear Medicine*, 61(5), 751–756.
- Klingler, S., & Holland, J. P. (2022). Automated light-induced synthesis of <sup>89</sup>Zr-radiolabeled antibodies for immuno-positron emission tomography. *Scientific Reports*, 12(1), 1–10.
- Koskinen, K., Vainio, P. J., Smith, D. J., Pihlavisto, M., Ylä-Herttua, S., Jalkanen, S., & Salmi, M. (2004). Granulocyte transmigration through the endothelium is regulated by the oxidase activity of vascular adhesion protein-1 (VAP-1). *Blood*, 103(9), 3388–3395.
- Kou, Y., Yao, Z., & Cheng, Z. (2021). Al<sup>18</sup>F-NOTA-FAPI-04 Outperforms 18F-FDG PET/CT in Identifying the Primary Lesion and Rare Metastases From Gastric Cancer. *Clinical Nuclear Medicine*, 46(12), e570–e571.
- Kuo, H. T., Pan, J., Zhang, Z., Lau, J., Merkens, H., Zhang, C., Colpo, N., Lin, K. S., & Bénard, F. (2018). Effects of Linker Modification on Tumor-to-Kidney Contrast of <sup>68</sup>Ga-Labeled PSMA-Targeted Imaging Probes. *Molecular Pharmaceutics*, 15(8), 3502–3511.
- Kzhyshkowska, J., Gratchev, A., & Goerdts, S. (2006). Stabilin-1, a homeostatic scavenger receptor with multiple functions. *Journal of Cellular and Molecular Medicine*, 10(3), 635–649.
- Laboratoire National Henri Becquerel. (n.d.). Retrieved July 6, 2022, from <http://www.lnhb.fr/nuclear-data/nuclear-data-table/>.
- Lamare, F., Hinz, R., Gaemperli, O., Pugliese, F., Mason, J. C., Spinks, T., Camici, P. G., & Rimoldi, O. E. (2011). Detection and quantification of large-vessel inflammation with <sup>11</sup>C-(R)-PK11195 PET/CT. *Journal of Nuclear Medicine*, 52(1), 33–39.
- Lamb, J., & Holland, J. P. (2018). Advanced methods for radiolabeling multimodality nanomedicines for SPECT/MRI and PET/MRI. *Journal of Nuclear Medicine*, 59(3), 382–389.
- Lancelot, S., & Zimmer, L. (2010). Small-animal positron emission tomography as a tool for neuropharmacology. *Trends in Pharmacological Sciences*, 31(9), 411–417.
- Lapa, C., Reiter, T., Li, X., Werner, R. A., Samnick, S., Jahns, R., Buck, A. K., Ertl, G., & Bauer, W. R. (2015). Imaging of myocardial inflammation with somatostatin receptor based PET/CT - A comparison to cardiac MRI. *International Journal of Cardiology*, 194, 44–49.
- Laverman, P., van der Geest, T., Terry, S. Y. A., Gerrits, D., Walgreen, B., Helsen, M. M., Nayak, T. K., Freimoser-Grundschober, A., Waldhauer, I., Hosse, R. J., Moessner, E., Umana, P., Klein, C., Oyen, W. J. G., Koenders, M. I., & Boerman, O. C. (2015). Immuno-PET and immuno-SPECT of rheumatoid arthritis with radiolabeled anti-fibroblast activation protein antibody correlates with severity of arthritis. *Journal of Nuclear Medicine*, 56(5), 778–783.
- Lee, S. P., Im, H. J., Kang, S., Chung, S. J., Cho, Y. S., Kang, H., Park, H. S., Hwang, D. W., Park, J. B., Paeng, J. C., Cheon, G. J., Lee, Y. S., Jeong, J. M., & Kim, Y. J. (2017). Noninvasive imaging of myocardial inflammation in myocarditis using <sup>68</sup>Ga-tagged mannosylated human serum albumin positron emission tomography. *Theranostics*, 7(2), 413–424.
- Lepareur, N. (2022). Cold Kit Labeling: The Future of <sup>68</sup>Ga Radiopharmaceuticals? *Frontiers in Medicine*, 9, 59.
- Li, X., Bauer, W., Kreissl, M. C., Weirather, J., Bauer, E., Israel, I., Richter, D., Riehl, G., Buck, A., & Samnick, S. (2013). Specific somatostatin receptor II expression in arterial plaque: <sup>68</sup>Ga-DOTATATE autoradiographic, immunohistochemical and flow cytometric studies in apoE-deficient mice. *Atherosclerosis*, 230(1), 33–39.
- Li, X. G., Autio, A., Ahtinen, H., Helariutta, K., Liljenbäck, H., Jalkanen, S., Roivainen, A., & Airaksinen, A. J. (2013). Translating the concept of peptide labeling with 5-deoxy-5-[<sup>18</sup>F]fluororibose into preclinical practice: <sup>18</sup>F-labeling of Siglec-9 peptide for PET imaging of inflammation. *Chemical Communications*, 49(35), 3682–3684.
- Li, X. G., Dall'angelo, S., Schweiger, L. F., Zanda, M., & O'hagan, D. (2012). [<sup>18</sup>F]-5-Fluoro-5-deoxyribose, an efficient peptide bioconjugation ligand for positron emission tomography (PET) imaging. *Chemical Communications*, 48(43), 5247–5249.
- Lin, M., Welch, M. J., & Lapi, S. E. (2013). Effects of Chelator Modifications on <sup>68</sup>Ga-Labeled [Tyr 3] Octreotide Conjugates. *Molecular Imaging and Biology*, 15(5), 606–613.



- Lindner, T., Giesel, F. L., Kratochwil, C., & Serfling, S. E. (2021). Radioligands targeting fibroblast activation protein (FAP). *Cancers*, *13*(22).
- Harris, L.J., Larson, S.B., Hasel, K.W., & McPherson A. (1997). Refined Structure of an Intact IgG2a Monoclonal Antibody. *Biochemistry* *36*(7), 1581-1597.
- Liu, X., & Laforest, R. (2009). Quantitative small animal PET imaging with nonconventional nuclides. *Nuclear Medicine and Biology*, *36*(5), 551-559.
- Liu, Y., Gunsten, S. P., Sultan, D. H., Luehmann, H. P., Zhao, Y., Blackwell, T. S., Bollermann-Nowlis, Z., Pan, J. H., Byers, D. E., Atkinson, J. J., Kreisel, D., Holtzman, M. J., Gropler, R. J., Combadiere, C., & Brody, S. L. (2017). PET-based imaging of chemokine receptor 2 in experimental and Disease-related lung inflammation. *Radiology*, *283*(3), 758-768.
- Loktionova, N. S., Belozub, A. N., Filosofov, D. v., Zhemosekov, K. P., Wagner, T., Türler, A., & Rösch, F. (2011). Improved column-based radiochemical processing of the generator produced  $^{68}\text{Ga}$ . *Applied Radiation and Isotopes*, *69*(7), 942-946.
- Lu, J., Xu, H., Xia, J., Ma, J., Xu, J., Li, Y., & Feng, J. (2020). D- and Unnatural Amino Acid Substituted Antimicrobial Peptides With Improved Proteolytic Resistance and Their Proteolytic Degradation Characteristics. *Frontiers in Microbiology*, *11*, 2869.
- Lu, R. M., Hwang, Y. C., Liu, I. J., Lee, C. C., Tsai, H. Z., Li, H. J., & Wu, H. C. (2020). Development of therapeutic antibodies for the treatment of diseases. *Journal of Biomedical Science*, *27*(1), 1-30.
- Luo, Y., Pan, Q., Yang, H., Peng, L., Zhang, W., & Li, F. (2021). Fibroblast activation protein-targeted PET/CT with  $^{68}\text{Ga}$ -FAPI for imaging igg4-related disease: Comparison to  $^{18}\text{F}$ -FDG PET/CT. *Journal of Nuclear Medicine*, *62*(2), 266-271.
- Lütje, S., Franssen, G. M., Herrmann, K., Boerman, O. C., Rijpkema, M., Gotthardt, M., & Heskamp, S. (2019). In vitro and in vivo characterization of an  $^{18}\text{F}$ -ALF-labeled PSMA ligand for imaging of PSMA-expressing xenografts. *Journal of Nuclear Medicine*, *60*(7), 1017-1022.
- Malik, N., Baur, B., Winter, G., Reske, S. N., Beer, A. J., & Solbach, C. (2015). Radiofluorination of PSMA-HBED via  $\text{Al}^{18}\text{F}2+$  Chelation and Biological Evaluations In Vitro. *Molecular Imaging and Biology*, *17*(6), 777-785.
- Martens, J. H., Kzhyshkowska, J., Falkowski-Hansen, M., Schledzewski, K., Gratchev, A., Mansmann, U., Schmuttermaier, C., Dippel, E., Koenen, W., Riedel, F., Sankala, M., Tryggvason, K., Kobzik, L., Moldenhauer, G., Arnold, B., & Goerdts, S. (2006). Differential expression of a gene signature for scavenger/lectin receptors by endothelial cells and macrophages in human lymph node sinuses, the primary sites of regional metastasis. *Journal of Pathology*, *208*(4), 574-589.
- Martins, A. F., Prata, M. I. M., Rodrigues, S. P. J., Geraldes, C. F. G. C., Riss, P. J., Amor-Coarasa, A., Burchardt, C., Kroll, C., & Roesch, F. (2013). Spectroscopic, radiochemical, and theoretical studies of the  $\text{Ga}^{3+}$ -N-2-hydroxyethyl piperazine-N'-2-ethanesulfonic acid (HEPES buffer) system: evidence for the formation of  $\text{Ga}^{3+}$ -HEPES complexes in  $^{68}\text{Ga}$  labeling reactions. *Contrast Media & Molecular Imaging*, *8*(3), 265-273.
- McBride, W. J., Sharkey, R. M., Karacay, H., D'Souza, C. A., Rossi, E. A., Laverman, P., Chang, C. H., Boerman, O. C., & Goldenberg, D. M. (2009). A novel method of  $^{18}\text{F}$  radiolabeling for PET. *Journal of Nuclear Medicine*, *50*(6), 991-998.
- Melson, G. A. (1979). Coordination Chemistry of Macrocyclic Compounds. In G. A. Melson (Ed.), *Angewandte Chemie* (Issue 5). Plenum Press.
- Meyer, G. J., Mäcke, H., Schuhmacher, J., Knapp, W. H., & Hofmann, M. (2004).  $^{68}\text{Ga}$ -labelled DOTA-derivatised peptide ligands. *European Journal of Nuclear Medicine and Molecular Imaging*, *31*(8), 1097-1104.
- Meyer, J. P., Adumeau, P., Lewis, J. S., & Zeglis, B. M. (2016). Click Chemistry and Radiochemistry: The First 10 Years. *Bioconjugate Chemistry*, *27*(12), 2791-2807.
- Miller, P. W., Long, N. J., Vilar, R., & Gee, A. D. (2008). Synthesis of  $^{11}\text{C}$ ,  $^{18}\text{F}$ ,  $^{15}\text{O}$ , and  $^{13}\text{N}$  radiolabels for positron emission tomography. *Angewandte Chemie - International Edition*, *47*(47), 8998-9033.
- Moisio, O., Palani, S., Virta, J., Elo, P., Liljenbäck, H., Tolvanen, T., Käkälä, M., Miner, M. G., Herre, E. A., Marjamäki, P., Örd, T., Heinäniemi, M., Kaikkonen, M. U., Zhang, F., Srinivasarao, M., Knuuti, J., Low,

- P. S., Saraste, A., Li, X. G., & Roivainen, A. (2020). Radiosynthesis and preclinical evaluation of [<sup>68</sup>Ga]Ga-NOTA-folate for PET imaging of folate receptor β-positive macrophages. *Scientific Reports*, *10*(1), 1–10.
- Moisis, O., Siitonen, R., Liljenbäck, H., Suomela, E., Jalkanen, S., Li, X.-G., & Roivainen, A. (2018). Exploring Alternative Radiolabeling Strategies for Sialic Acid-Binding Immunoglobulin-Like Lectin 9 Peptide: [<sup>68</sup>Ga]Ga- and [<sup>18</sup>F]AlF-NOTA-Siglec-9. *Molecules*, *23*(2), 305.
- Morris, O., Fairclough, M., Grigg, J., Prenant, C., & McMahon, A. (2019). A review of approaches to 18 F radiolabelling affinity peptides and proteins. *Journal of Labelled Compounds and Radiopharmaceuticals*, *62*(1), 4–23.
- Mortenson, D. E., Kreidler, D. F., Thomas, N. C., Guzei, I. A., Gellman, S. H., & Forest, K. T. (2018). Evaluation of β-Amino Acid Replacements in Protein Loops: Effects on Conformational Stability and Structure. *ChemBioChem*, *19*(6), 604–612.
- Muehllhner, G., & Karp, J. S. (2006). Positron emission tomography. *Physics in Medicine and Biology*, *51*(13), R117.
- Mueller, D., Breeman, W. A. P., Klette, I., Gottschaldt, M., Odparlik, A., Baehre, M., Tworowska, I., & Schultz, M. K. (2016). Radiolabeling of DOTA-like conjugated peptides with generator-produced <sup>68</sup>Ga and using NaCl-based cationic elution method. *Nature Protocols*, *11*(6), 1057–1066.
- Mueller, D., Fuchs, A., Leshch, Y., & Proehl, M. (2019). The Shortage of Approved <sup>68</sup>Ge/<sup>68</sup>Ga Generators - Incoming Material Inspection and GMP Compliant Use of Non-Approved Generators. *Journal of Nuclear Medicine*, *60*(supplement 1).
- Mueller, D., Klette, I., Baum, R. P., Gottschaldt, M., Schultz, M. K., & Breeman, W. A. P. (2012). Simplified NaCl based <sup>68</sup>Ga concentration and labeling procedure for rapid synthesis of <sup>68</sup>Ga radiopharmaceuticals in high radiochemical purity. *Bioconjugate Chemistry*, *23*(8), 1712–1717.
- Müller, A., Beck, K., Rancic, Z., Müller, C., Fischer, C. R., Betzel, T., Kaufmann, P. A., Schibli, R., Krämer, S. D., & Ametamey, S. M. (2014). Imaging atherosclerotic plaque inflammation via folate receptor targeting using a novel 18F-folate radiotracer. *Molecular Imaging*, *13*(2).
- Müller, K., Faeh, C., & Diederich, F. (2007). Fluorine in pharmaceuticals: Looking beyond intuition. *Science*, *317*(5846), 1881–1886.
- Munoz, C., Ellis, S., Nekolla, S. G., Kunze, K. P., Vitadello, T., Neji, R., Botnar, R. M., Schnabel, J. A., Reader, A. J., & Prieto, C. (2021). MRI-Guided Motion-Corrected PET Image Reconstruction for Cardiac PET/MRI. *Journal of Nuclear Medicine*, *62*(12), 1768–1774.
- Nagengast, W. B., Lub-de Hooge, M. N., Oosting, S. F., den Dunnen, W. F. A., Warnders, F. J., Brouwers, A. H., de Jong, J. R., Price, P. M., Hollema, H., Hospers, G. A. P., Elsinga, P. H., Hesselink, J. W., Gietema, J. A., & de Vries, E. G. E. (2011). VEGF-PET imaging is a noninvasive biomarker showing differential changes in the tumor during sunitinib treatment. *Cancer Research*, *71*(1), 143–153.
- Naka, S., Watabe, T., Lindner, T., Cardinale, J., Kurimoto, K., Moore, M., Tatsumi, M., Mori, Y., Shimosegawa, E., Valla, F., Kato, H., & Giesel, F. L. (2021). One-pot and one-step automated radio-synthesis of [<sup>18</sup>F]AlF-FAPI-74 using a multipurpose synthesizer: a proof-of-concept experiment. *EJNMMI Radiopharmacy and Chemistry*, *6*(1), 28.
- Namavari, M., Cheng, Z., Zhang, R., de Abhijit, Levi, J., Hoerner, J. K., Yaghoubi, S. S., Syud, F. A., & Gambhir, S. S. (2009). A novel method for direct site-specific radiolabeling of peptides Using [<sup>18</sup>F]FDG. *Bioconjugate Chemistry*, *20*(3), 432–436.
- Nawaz, S., Mullen, G. E. D., Sunassee, K., Bordoloi, J., Blower, P. J., & Ballinger, J. R. (2017). Simple, mild, one-step labelling of proteins with gallium-68 using a tris(hydroxypyridinone) bifunctional chelator: a <sup>68</sup>Ga-THP-scFv targeting the prostate-specific membrane antigen. *EJNMMI Research*, *7*(1), 1–9.
- Nobashi, T., Nakamoto, Y., Kubo, T., Ishimori, T., Handa, T., Tanizawa, K., Sano, K., Mishima, M., & Togashi, K. (2016). The utility of PET/CT with <sup>68</sup>Ga-DOTATOC in sarcoidosis: comparison with <sup>67</sup>Ga-scintigraphy. *Annals of Nuclear Medicine*, *30*(8), 544–552.
- Notni, J., Pohle, K., & Wester, H. J. (2013). Be spoilt for choice with radiolabelled RGD peptides: Preclinical evaluation of <sup>68</sup>Ga-TRAP(RGD)3. *Nuclear Medicine and Biology*, *40*(1), 33–41.

- Notni, J., Šimeček, J., Hermann, P., & Wester, H.-J. (2011). TRAP, a Powerful and Versatile Framework for Gallium-68 Radiopharmaceuticals. *Chemistry - A European Journal*, *17*(52), 14718–14722.
- Orecchioni, M., Ghosheh, Y., Pramod, A. B., & Ley, K. (2019). Macrophage polarization: Different gene signatures in M1(Lps<sup>+</sup>) vs. Classically and M2(LPS<sup>-</sup>) vs. Alternatively activated macrophages. *Frontiers in Immunology*, *10*(MAY), 1084.
- Ovacik, M., & Lin, K. (2018). Tutorial on Monoclonal Antibody Pharmacokinetics and Its Considerations in Early Development. *Clinical and Translational Science*, *11*(6), 540–552.
- Palani, S., Maksimow, M., Mäilüniemi, M., Auvinen, K., Jalkanen, S., & Salmi, M. (2011). Stabilin-1/CLEVER-1, a type 2 macrophage marker, is an adhesion and scavenging molecule on human placental macrophages. *European Journal of Immunology*, *41*(7), 2052–2063.
- Parker, N., Turk, M. J., Westrick, E., Lewis, J. D., Low, P. S., & Leamon, C. P. (2005). Folate receptor expression in carcinomas and normal tissues determined by a quantitative radioligand binding assay. *Analytical Biochemistry*, *338*(2), 284–293.
- Patra, M., Bauman, A., Mari, C., Fischer, C. A., Häussinger, D., Gasser, G., & Mindt, T. L. (2014). An octadentate bifunctional chelating agent for the development of stable zirconium-89 based molecular imaging probes. *Chemical Communications*, *50*(78), 11523–11525.
- Pattison, D. A., Debowski, M., Gulhane, B., Arnfield, E. G., Pelecanos, A. M., Garcia, P. L., Latter, M. J., Lin, C. Y., Roberts, M. J., Ramsay, S. C., & Thomas, P. A. (2022). Prospective intra-individual blinded comparison of [<sup>18</sup>F]PSMA-1007 and [<sup>68</sup>Ga]Ga-PSMA-11 PET/CT imaging in patients with confirmed prostate cancer. *European Journal of Nuclear Medicine and Molecular Imaging*, *49*(2), 763–776.
- Perk, L. R., Vosjan, M. J. W. D., Visser, G. W. M., Budde, M., Jurek, P., Kiefer, G. E., & van Dongen, G. A. M. S. (2010). P-Isothiocyanatobenzyl-desferrioxamine: A new bifunctional chelate for facile radiolabeling of monoclonal antibodies with zirconium-89 for immuno-PET imaging. *European Journal of Nuclear Medicine and Molecular Imaging*, *37*(2), 250–259.
- Pfaff, S., Nehring, T., Pichler, V., Cardinale, J., Mitterhauser, M., Hacker, M., & Wadsak, W. (2018). Development and evaluation of a rapid analysis for HEPES determination in <sup>68</sup>Ga-radiotracers. *EJNMMI Research*, *8*(1), 95.
- Pichler, B. J., Judenhofer, M. S., & Pfannenbergl, C. (2008). Multimodal imaging approaches: PET/CT and PET/MRI. *Handbook of Experimental Pharmacology*, *185*, 109–132.
- Pijl, J. P., Nienhuis, P. H., Kwee, T. C., Glaudemans, A. W. J. M., Slart, R. H. J. A., & Gormsen, L. C. (2021). Limitations and Pitfalls of FDG-PET/CT in Infection and Inflammation. *Seminars in Nuclear Medicine*, *51*(6), 633–645.
- Piron, S., de Man, K., van Laeken, N., D’Asseler, Y., Bacher, K., Kersemans, K., Ost, P., Decaestecker, K., Deseyne, P., Fonteyne, V., Lumen, N., Achten, E., Brans, B., & de Vos, F. (2019). Radiation dosimetry and biodistribution of <sup>18</sup>F-PSMA-11 for PET imaging of prostate cancer. *Journal of Nuclear Medicine*, *60*(12), 1736–1742.
- Poels, K., Schreurs, M., Jansen, M., Vugts, D. J., Seijkens, T. T. P., van Dongen, G. A. M. S., Lutgens, E., & Beaino, W. (2022). Immuno-PET Imaging of Atherosclerotic Plaques with [<sup>89</sup>Zr]Zr-Anti-CD40 mAb—Proof of Concept. *Biology*, *11*(3), 408.
- Price, E. W., & Orvig, C. (2014). Matching chelators to radiometals for radiopharmaceuticals. *Chemical Society Reviews*, *43*(1), 260–290.
- Quigley, N. G., Steiger, K., Hoberück, S., Czech, N., Zierke, M. A., Kossatz, S., Pretze, M., Richter, F., Weichert, W., Pox, C., Kotzerke, J., & Notni, J. (2022). PET/CT imaging of head-and-neck and pancreatic cancer in humans by targeting the “Cancer Integrin” α<sub>v</sub>β<sub>6</sub> with Ga-68-Trivehexin. *European Journal of Nuclear Medicine and Molecular Imaging*, *49*(4), 1136–1147.
- Raavé, R., Sandker, G., Adumeau, P., Jacobsen, C. B., Mangin, F., Meyer, M., Moreau, M., Bernhard, C., da Costa, L., Dubois, A., Goncalves, V., Gustafsson, M., Rijpkema, M., Boerman, O., Chambron, J. C., Heskamp, S., & Denat, F. (2019). Direct comparison of the in vitro and in vivo stability of DFO, DFO\* and DFOcyclo\* for <sup>89</sup>Zr-immunoPET. *European Journal of Nuclear Medicine and Molecular Imaging*, *46*(9), 1966–1977.

- Rantakari, P., Patten, D. A., Valtonen, J., Karikoski, M., Gerke, H., Dawes, H., Laurila, J., Ohlmeier, S., Elima, K., Hübscher, S. G., Weston, C. J., Jalkanen, S., Adams, D. H., Salmi, M., & Shetty, S. (2016). Stabilin-1 expression defines a subset of macrophages that mediate tissue homeostasis and prevent fibrosis in chronic liver injury. *Proceedings of the National Academy of Sciences of the United States of America*, *113*(33), 9298–9303.
- Reiter, T., Kircher, M., Schirbel, A., Werner, R. A., Kropf, S., Ertl, G., Buck, A. K., Wester, H. J., Bauer, W. R., & Lapa, C. (2018). Imaging of C-X-C Motif Chemokine Receptor CXCR4 Expression After Myocardial Infarction With [<sup>68</sup>Ga]Pentixafor-PET/CT in Correlation With Cardiac MRI. *JACC: Cardiovascular Imaging*, *11*(10), 1541–1543.
- Retamal, J., Sörensen, J., Lubberink, M., Suarez-Sipmann, F., Borges, J. B., Feinstein, R., Jalkanen, S., Antoni, G., Hedenstierna, G., Roivainen, A., Larsson, A., & Velikyan, I. (2016). Feasibility of <sup>68</sup>Ga-labeled Siglec-9 peptide for the imaging of acute lung inflammation: a pilot study in a porcine model of acute respiratory distress syndrome. *American Journal of Nuclear Medicine and Molecular Imaging*, *6*(1), 18–31.
- Reubi, J. C., & Maecke, H. R. (2008). Peptide-based probes for cancer imaging. *Journal of Nuclear Medicine*, *49*(11), 1735–1738.
- Richter, S., & Wuest, F. (2014). <sup>18</sup>F-labeled peptides: The future is bright. *Molecules*, *19*(12), 20536–20556.
- Rinne, S. S., Leitao, C. D., Abouzayed, A., Vorobyeva, A., Tolmachev, V., Ståhl, S., Löfblom, J., & Orlova, A. (2021). HER3 PET Imaging: <sup>68</sup>Ga-Labeled Affibody Molecules Provide Superior HER3 Contrast to <sup>89</sup>Zr-Labeled Antibody and Antibody-Fragment-Based Tracers. *Cancers*, *13*(19), 4791.
- Rodnick, M. E., Sollert, C., Stark, D., Clark, M., Katsifis, A., Hockley, B. G., Parr, D. C., Frigell, J., Henderson, B. D., Bruton, L., Preshlock, S., Abghari-Gerst, M., Piert, M. R., Fulham, M. J., Eberl, S., Gagnon, K., & Scott, P. J. H. (2022). Synthesis of <sup>68</sup>Ga-radiopharmaceuticals using both generator-derived and cyclotron-produced <sup>68</sup>Ga as exemplified by [<sup>68</sup>Ga]Ga-PSMA-11 for prostate cancer PET imaging. *Nature Protocols*, *17*(4), 980–1003.
- Rudd, J. H. F., Warburton, E. A., Fryer, T. D., Jones, H. A., Clark, J. C., Antoun, N., Johnström, P., Davenport, A. P., Kirkpatrick, P. J., Arch, B. N., Pickard, J. D., & Weissberg, P. L. (2002). Imaging atherosclerotic plaque inflammation with [<sup>18</sup>F]-fluorodeoxyglucose positron emission tomography. *Circulation*, *105*(23), 2708–2711.
- Rudd, S. E., Roselt, P., Cullinane, C., Hicks, R. J., & Donnelly, P. S. (2016). A desferrioxamine B squaramide ester for the incorporation of zirconium-89 into antibodies. *Chemical Communications*, *52*(80), 11889–11892.
- Russelli, L., Martinelli, J., de Rose, F., Reder, S., Herz, M., Schwaiger, M., Weber, W., Tei, L., & D'Alessandria, C. (2020). Room Temperature Al<sup>18</sup>F Labeling of 2-Aminomethylpiperidine-Based Chelators for PET Imaging. *ChemMedChem*, *15*(3), 284–292.
- Salmi, M., & Jalkanen, S. (2019). Vascular Adhesion Protein-1: A Cell Surface Amine Oxidase in Translation. *Antioxidants & Redox Signaling*, *30*(3), 314–332.
- Salmi, M., Kalimo, K., & Jalkanen, S. (1993). Induction and function of vascular adhesion protein-1 at sites of inflammation. *Journal of Experimental Medicine*, *178*(6), 2255–2260.
- Salmi, M., Koskinen, K., Henttinen, T., Elima, K., & Jalkanen, S. (2004). CLEVER-1 mediates lymphocyte transmigration through vascular and lymphatic endothelium. *Blood*, *104*(13), 3849–3857.
- Sanchez-Crespo, A. (2013). Comparison of Gallium-68 and Fluorine-18 imaging characteristics in positron emission tomography. *Applied Radiation and Isotopes*, *76*, 55–62.
- Schniering, J., Benešová, M., Brunner, M., Haller, S., Cohrs, S., Frauenfelder, T., Vrugt, B., Feghali-Bostwick, C., Schibli, R., Distler, O., Müller, C., & Maurer, B. (2019). <sup>18</sup>F-AzaFol for Detection of Folate Receptor-β Positive Macrophages in Experimental Interstitial Lung Disease—A Proof-of-Concept Study. *Frontiers in Immunology*, *10*.
- Schollhammer, R., Lepreux, S., Barthe, N., Vimont, D., Rullier, A., Sibon, I., Berard, X., Zhang, A., Kimura, Y., Fujita, M., Innis, R. B., Zanotti-Fregonara, P., & Morgat, C. (2021). In vitro and pilot in vivo imaging of 18 kDa translocator protein (TSPO) in inflammatory vascular disease. *EJNMMI Research*, *11*(1), 45.

- Schönbeck, U., & Libby, P. (2001). CD40 Signaling and Plaque Instability. *Circulation Research*, 89(12), 1092–1103.
- Seemann, J., Eppard, E., Waldron, B. P., Ross, T. L., & Roesch, F. (2015). Cation exchange-based post-processing of  $^{68}\text{Ga}$ -eluate: A comparison of three solvent systems for labelling of DOTATOC, NO2APBP and DATAm. *Applied Radiation and Isotopes*, 98, 54–59.
- Shetty, D., Choi, S. Y., Jeong, J. M., Hoigebazar, L., Lee, Y., Lee, D. S., Chung, J., Lee, M. C., & Chung, Y. K. (2010). Formation and Characterization of Gallium(III) Complexes with Monoamide Derivatives of 1,4,7-Triazacyclononane-1,4,7-triacetic Acid: A Study of the Dependency of Structure on Reaction pH. *European Journal of Inorganic Chemistry*, 2010(34), 5432–5438.
- Siebermair, J., Köhler, M. I., Kupusovic, J., Nekolla, S. G., Kessler, L., Ferdinandus, J., Guberina, N., Stuschke, M., Grafe, H., Siveke, J. T., Kochhäuser, S., Fendler, W. P., Totzeck, M., Wakili, R., Umutilu, L., Schlosser, T., Rassaf, T., & Rischpler, C. (2021). Cardiac fibroblast activation detected by Ga-68 FAPI PET imaging as a potential novel biomarker of cardiac injury/remodeling. *Journal of Nuclear Cardiology*, 28(3), 812–821.
- Siitonen, R., Pietikäinen, A., Liljenbäck, H., Käkälä, M., Söderström, M., Jalkanen, S., Hytönen, J., & Roivainen, A. (2017). Targeting of vascular adhesion protein-1 by positron emission tomography visualizes sites of inflammation in *Borrelia burgdorferi*-infected mice. *Arthritis Research and Therapy*, 19(1).
- Silvola, J. M. U., Li, X. G., Virta, J., Marjamäki, P., Liljenbäck, H., Hytönen, J. P., Tarkia, M., Saunavaara, V., Hurme, S., Palani, S., Hakovirta, H., Ylä-Herttua, S., Saukko, P., Chen, Q., Low, P. S., Knuuti, J., Saraste, A., & Roivainen, A. (2018). Aluminum fluoride-18 labeled folate enables in vivo detection of atherosclerotic plaque inflammation by positron emission tomography. *Scientific Reports*, 8(1), 1–15.
- Šimeček, J., Notni, J., Kapp, T. G., Kessler, H., & Wester, H. J. (2014). Benefits of NOPO as chelator in gallium-68 peptides, exemplified by preclinical characterization of  $^{68}\text{Ga}$ -NOPO-c(RGDfK). *Molecular Pharmaceutics*, 11(5), 1687–1695.
- Sinnes, J. P., Nagel, J., Waldron, B. P., Maina, T., Nock, B. A., Bergmann, R. K., Ullrich, M., Pietzsch, J., Bachmann, M., Baum, R. P., & Rösch, F. (2019). Instant kit preparation of  $^{68}\text{Ga}$ -radiopharmaceuticals via the hybrid chelator DATA: clinical translation of [ $^{68}\text{Ga}$ ]Ga-DATA-TOC. *EJNMMI Research*, 9(1), 1–11.
- Sipilä, H. T., Clark, J. C., Peltola, O., & Teräs, M. (2001). An automatic [ $^{15}\text{O}$ ]H<sub>2</sub>O production system for heart and brain studies. *Journal of Labelled Compounds and Radiopharmaceuticals*, 44(S1), S1066–S1068.
- Skovgaard, D., Persson, M., & Kjaer, A. (2017). Urokinase Plasminogen Activator Receptor–PET with  $^{68}\text{Ga}$ -NOTA-AE105: First Clinical Experience with a Novel PET Ligand. *PET Clinics*, 12(3), 311–319.
- Stabin, M. G., & Siegel, J. A. (2018). RADAR dose estimate report: A compendium of radiopharmaceutical dose estimates based on OLINDA/EXM version 2.0. *Journal of Nuclear Medicine*, 59(1), 154–160.
- Summer, D., Garousi, J., Oroujeni, M., Mitran, B., Andersson, K. G., Vorobyeva, A., Löfblom, J., Orlova, A., Tolmachev, V., & Decristoforo, C. (2018). Cyclic versus Noncyclic Chelating Scaffold for  $^{89}\text{Zr}$ -Labeled ZEGFR:2377 Affibody Bioconjugates Targeting Epidermal Growth Factor Receptor Overexpression. *Molecular Pharmaceutics*, 15(1), 175–185.
- Sun, Y., Zeng, Y., Zhu, Y., Feng, F., Xu, W., Wu, C., Xing, B., Zhang, W., Wu, P., Cui, L., Wang, R., Li, F., Chen, X., & Zhu, Z. (2014). Application of  $^{68}\text{Ga}$ -PRGD2 PET/CT for  $\alpha_v\beta_3$ -integrin imaging of myocardial infarction and stroke. *Theranostics*, 4(8), 778–786.
- Tahara, N., Mukherjee, J., de Haas, H. J., Petrov, A. D., Tawakol, A., Haider, N., Tahara, A., Constantinescu, C. C., Zhou, J., Boersma, H. H., Imaizumi, T., Nakano, M., Finn, A., Fayad, Z., Virmani, R., Fuster, V., Bosca, L., & Narula, J. (2014). 2-deoxy-2- $^{[18}\text{F}]$ fluoro-d-mannose positron emission tomography imaging in atherosclerosis. *Nature Medicine*, 20(2), 215–219.
- Tanios, F., Pelisek, J., Lutz, B., Reutersberg, B., Matevossian, E., Schwamborn, K., Hösel, V., Eckstein, H. H., & Reeps, C. (2015). CXCR4: A Potential Marker for Inflammatory Activity in Abdominal Aortic Aneurysm Wall. *European Journal of Vascular and Endovascular Surgery*, 50(6), 745–753.

- Tarkin, J. M., Calcagno, C., Dweck, M. R., Evans, N. R., Chowdhury, M. M., Gopalan, D., Newby, D. E., Fayad, Z. A., Bennett, M. R., & Rudd, J. H. F. (2019).  $^{68}\text{Ga}$ -DOTATATE PET Identifies Residual Myocardial Inflammation and Bone Marrow Activation After Myocardial Infarction. *Journal of the American College of Cardiology*, 73(19), 2489–2491.
- Tarkin, J. M., Joshi, F. R., Evans, N. R., Chowdhury, M. M., Figg, N. L., Shah, A. v., Starks, L. T., Martin-Garrido, A., Manavaki, R., Yu, E., Kuc, R. E., Grassi, L., Kreuzhuber, R., Kostadima, M. A., Frontini, M., Kirkpatrick, P. J., Coughlin, P. A., Gopalan, D., Fryer, T. D., ... Rudd, J. H. F. (2017). Detection of Atherosclerotic Inflammation by  $^{68}\text{Ga}$ -DOTATATE PET Compared to [ $^{18}\text{F}$ ]FDG PET Imaging. *Journal of the American College of Cardiology*, 69(14), 1774–1791.
- Thackeray, J. T., Hupe, H. C., Wang, Y., Bankstahl, J. P., Berding, G., Ross, T. L., Bauersachs, J., Wollert, K. C., & Bengel, F. M. (2018). Myocardial Inflammation Predicts Remodeling and Neuroinflammation After Myocardial Infarction. *Journal of the American College of Cardiology*, 71(3), 263–275.
- Tieu, W., Hollis, C. A., Kuan, K. K. W., Takhar, P., Stuckings, M., Spooner, N., & Malinconico, M. (2019). Rapid and automated production of [ $^{68}\text{Ga}$ ]Gallium chloride and [ $^{68}\text{Ga}$ ]Ga-DOTA-TATE on a medical cyclotron. *Nuclear Medicine and Biology*, 74–75, 12–18.
- Tinianow, J. N., Pandya, D. N., Pailloux, S. L., Ogasawara, A., Vanderbilt, A. N., Gill, H. S., Williams, S. P., Wadas, T. J., Magda, D., & Marik, J. (2016). Evaluation of a 3-hydroxypyridin-2-one (2,3-HOPO) based macrocyclic chelator for  $^{89}\text{Zr}^{4+}$  and its use for immunoPET imaging of HER2 positive model of ovarian carcinoma in mice. *Theranostics*, 6(4), 511–521.
- Tshibangu, T., Cawthorne, C., Serdons, K., Pauwels, E., Gsell, W., Bormans, G., Deroose, C. M., & Cleeren, F. (2020). Automated GMP compliant production of [ $^{18}\text{F}$ ]AIF-NOTA-octreotide. *EJNMMI Radiopharmacy and Chemistry*, 5(1), 1–23.
- Tsuneyoshi, Y., Tanaka, M., Nagai, T., Sunahara, N., Matsuda, T., Sonoda, T., Ijiri, K., Komiyama, S., & Matsuyama, T. (2012). Functional folate receptor beta-expressing macrophages in osteoarthritis synovium and their M1/M2 expression profiles. *Scandinavian Journal of Rheumatology*, 41(2), 132–140.
- Ueda, M., Hisada, H., Temma, T., Shimizu, Y., Kimura, H., Ono, M., Nakamoto, Y., Togashi, K., & Saji, H. (2015). Gallium-68-Labeled Anti-HER2 Single-Chain Fv Fragment: Development and In Vivo Monitoring of HER2 Expression. *Molecular Imaging and Biology*, 17(1), 102–110.
- Van Have, F. der, Vastenhout, B., Ramakers, R. M., Branderhorst, W., Krah, J. O., Ji, C., Staelens, S. G., & Beekman, F. J. (2009). U-SPECT-II: An ultra-high-resolution device for molecular small-animal imaging. *Journal of Nuclear Medicine*, 50(4), 599–605.
- Varasteh, Z., Braeuer, M., Mohanta, S., Steinsiek, A.-L., Habenicht, A., Omidvari, N., Topping, G. J., Rischpler, C., Weber, W. A., Sager, H. B., Raes, G., Hernot, S., & Schwaiger, M. (2022). In vivo Visualization of M2 Macrophages in the Myocardium After Myocardial Infarction (MI) Using  $^{68}\text{Ga}$ -NOTA-Anti-MMR Nb: Targeting Mannose Receptor (MR, CD206) on M2 Macrophages. *Frontiers in Cardiovascular Medicine*, 9.
- Varasteh, Z., de Rose, F., Mohanta, S., Li, Y., Zhang, X., Miritsch, B., Scafetta, G., Yin, C., Sager, H. B., Glasl, S., Gorpas, D., Habenicht, A. J. R., Ntziachristos, V., Weber, W. A., Bartolazzi, A., Schwaiger, M., & D'Alessandria, C. (2021). Imaging atherosclerotic plaques by targeting Galectin-3 and activated macrophages using ( $^{89}\text{Zr}$ )-DFO- Galectin3-F(ab')<sub>2</sub> mAb. *Theranostics*, 11(4), 1864–1876.
- Varasteh, Z., Mohanta, S., Li, Y., López Armbruster, N., Braeuer, M., Nekolla, S. G., Habenicht, A., Sager, H. B., Raes, G., Weber, W., Hernot, S., & Schwaiger, M. (2019). Targeting mannose receptor expression on macrophages in atherosclerotic plaques of apolipoprotein E-knockout mice using  $^{68}\text{Ga}$ -NOTA-anti-MMR nanobody: non-invasive imaging of atherosclerotic plaques. *EJNMMI Research*, 9(1), 1–10.
- Varasteh, Z., Mohanta, S., Robu, S., Braeuer, M., Li, Y., Omidvari, N., Topping, G., Sun, T., Nekolla, S. G., Richter, A., Weber, C., Habenicht, A., Haberkorn, U. A., & Weber, W. A. (2019). Molecular imaging of fibroblast activity after myocardial infarction using a  $^{68}\text{Ga}$ -labeled fibroblast activation protein inhibitor, FAPI-04. *Journal of Nuclear Medicine*, 60(12), 1743–1749.
- Vävere, A. L., & Scott, P. J. H. (2017). Clinical Applications of Small-molecule PET Radiotracers: Current Progress and Future Outlook. *Seminars in Nuclear Medicine*, 47(5), 429–453.

- Velikyan, I. (2015).  $^{68}\text{Ga}$ -Based Radiopharmaceuticals: Production and Application Relationship. *Molecules*, 20(7), 12913–12943.
- Verweij, N. J. F., Yaqub, M., Bruijnen, S. T. G., Pieplensbosch, S., ter Wee, M. M., Jansen, G., Chen, Q., Low, P. S., Windhorst, A. D., Lammertsma, A. A., Hoekstra, O. S., Voskuyl, A. E., & van der Laken, C. J. (2020). First in man study of [ $^{18}\text{F}$ ]fluoro-PEG-folate PET: a novel macrophage imaging technique to visualize rheumatoid arthritis. *Scientific Reports*, 10(1), 1047.
- Viitanen, R., Moisio, O., Lankinen, P., Li, X. G., Koivumaki, M., Suilamo, S., Tolvanen, T., Taimen, K., Mali, M., Kohonen, I., Koskivirta, I., Oikonen, V., Virtanen, H., Santalahti, K., Autio, A., Saraste, A., Pirilä, L., Nuutila, P., Knuuti, J., ... Roivainen, A. (2021). First-in-humans study of  $^{68}\text{Ga}$ -DOTA-Siglec-9, a PET ligand targeting vascular adhesion protein 1. *Journal of Nuclear Medicine*, 62(4), 577–583.
- Vilche, M., Banchero, A., Menandez, J., Balter, H., Gaudiano, P., & Engler, H. (2019).  $^{68}\text{Ga}$ -NOTA-UBI 29-41: A specific radiopharmaceutical for diagnosis of bacterial infection by PET/CT in hip prosthesis. *Journal of Nuclear Medicine*, 60(supplement 1).
- Virtakoivu, R., Rannikko, J. H., Viitala, M., Vaura, F., Takeda, A., Lonnberg, T., Koivunen, J., Jaakkola, P., Pasanen, A., Shetty, S., de Jonge, M. J. A., Robbrecht, D., Ma, Y. T., Skytta, T., Minchom, A., Jalkanen, S., Karvonen, M. K., Mandelin, J., Bono, P., & Hollmen, M. (2021). Systemic blockade of clever-1 elicits lymphocyte activation alongside checkpoint molecule downregulation in patients with solid tumors: Results from a phase I/II clinical trial. *Clinical Cancer Research*, 27(15), 4205–4220.
- Virtanen, H., Autio, A., Siitonen, R., Liljenbäck, H., Saanijoki, T., Lankinen, P., Mäkilä, J., Käkälä, M., Teuho, J., Savisto, N., Jaakkola, K., Jalkanen, S., & Roivainen, A. (2015).  $^{68}\text{Ga}$ -DOTA-Siglec-9 - a new imaging tool to detect synovitis. *Arthritis Research and Therapy*, 17(1), 1–11.
- Virtanen, H., Silvola, J. M. U., Autio, A., Li, X. G., Liljenbäck, H., Hellberg, S., Siitonen, R., Stahle, M., Käkälä, M., Airaksinen, A. J., Helariutta, K., Tolvanen, T., Veres, T. Z., Saraste, A., Knuuti, J., Jalkanen, S., & Roivainen, A. (2017). Comparison of  $^{68}\text{Ga}$ -DOTA-Siglec-9 and  $^{18}\text{F}$ -fluorodeoxyribose-Siglec-9: Inflammation imaging and radiation dosimetry. *Contrast Media and Molecular Imaging*, 2017.
- Vosjan, M. J. W. D., Perk, L. R., Roovers, R. C., Visser, G. W. M., Stigter-Van Walsum, M., van Bergen En Henegouwen, P. M. P., & van Dongen, G. A. M. S. (2011). Facile labelling of an anti-epidermal growth factor receptor Nanobody with  $^{68}\text{Ga}$  via a novel bifunctional desferal chelate for immuno-PET. *European Journal of Nuclear Medicine and Molecular Imaging*, 38(4), 753–763.
- Vosjan, M. J. W. D., Perk, L. R., Visser, G. W. M., Budde, M., Jurek, P., Kiefer, G. E., & van Dongen, G. A. M. S. (2010). Conjugation and radiolabeling of monoclonal antibodies with zirconium-89 for PET imaging using the bifunctional chelate p-isothiocyanatobenzyl-desferrioxamine. *Nature Protocols*, 5(4), 739–743.
- Vuğts, D. J., Klaver, C., Sewing, C., Poot, A. J., Adamzek, K., Huegli, S., Mari, C., Visser, G. W. M., Valverde, I. E., Gasser, G., Mindt, T. L., & van Dongen, G. A. M. S. (2017). Comparison of the octadentate bifunctional chelator DFO\*-pPhe-NCS and the clinically used hexadentate bifunctional chelator DFO-pPhe-NCS for  $^{89}\text{Zr}$ -immuno-PET. *European Journal of Nuclear Medicine and Molecular Imaging*, 44(2), 286–295.
- Wang, S., Zhou, X., Xu, X., Ding, J., Liu, S., Hou, X., Li, N., Zhu, H., & Yang, Z. (2021). Clinical translational evaluation of  $\text{Al}^{18}\text{F}$ -NOTA-FAPI for fibroblast activation protein-targeted tumour imaging. *European Journal of Nuclear Medicine and Molecular Imaging*, 48(13), 4259–4271.
- Wang, X., Jaraquemada-Peláez, M. D. G., Cao, Y., Pan, J., Lin, K. S., Patrick, B. O., & Orvig, C. (2019). H 2 hox: Dual-Channel Oxine-Derived Acyclic Chelating Ligand for  $^{68}\text{Ga}$  Radiopharmaceuticals. *Inorganic Chemistry*, 58(4), 2275–2285.
- Wang, Z., Zhang, M., Wang, L., Wang, S., Kang, F., Li, G., Jacobson, O., Niu, G., Yang, W., Wang, J., & Chen, X. (2015). Prospective study of  $^{68}\text{Ga}$ -NOTA-NFB: Radiation dosimetry in healthy volunteers and first application in glioma patients. *Theranostics*, 5(8), 882–889.
- Wei, W., Rosenkrans, Z. T., Liu, J., Huang, G., Luo, Q. Y., & Cai, W. (2020). ImmunoPET: Concept, Design, and Applications. *Chemical Reviews*, 120(8), 3787–3851.
- Wibowo, A. S., Singh, M., Reeder, K. M., Carter, J. J., Kovach, A. R., Meng, W., Ratnam, M., Zhang, F., & Dann, C. E. (2013). Structures of human folate receptors reveal biological trafficking states and diversity

- in folate and antifolate recognition. *Proceedings of the National Academy of Sciences of the United States of America*, 110(38), 15180–15188.
- Withers, P. J., Bouman, C., Carmignato, S., Cnudde, V., Grimaldi, D., Hagen, C. K., Maire, E., Manley, M., du Plessis, A., & Stock, S. R. (2021). X-ray computed tomography. *Nature Reviews Methods Primers*, 1(1), 1–21.
- Wu, M., Ning, J., Li, J., Lai, Z., Shi, X., Xing, H., Hacker, M., Liu, B., Huo, L., & Li, X. (2022). Feasibility of in vivo Imaging of Fibroblast Activation Protein in Human Arterial Walls. *Journal of Nuclear Medicine*, 63(6), 948–951.
- Xia, W., Hilgenbrink, A. R., Matteson, E. L., Lockwood, M. B., Cheng, J. X., & Low, P. S. (2009). A functional folate receptor is induced during macrophage activation and can be used to target drugs to activated macrophages. *Blood*, 113(2), 438–446.
- Xu, Y., Wang, L., Pan, D., Yan, J., Wang, X., Yang, R., Li, M., Liu, Y., & Yang, M. (2020). Synthesis of a novel <sup>89</sup>Zr-labeled HER2 affibody and its application study in tumor PET imaging. *EJNMMI Research*, 10.
- Yoon, J. K., Park, B. N., Ryu, E. K., An, Y. S., & Lee, S. J. (2020). Current perspectives on <sup>89</sup>Zr-PET imaging. *International Journal of Molecular Sciences*, 21(12), 1–18.
- Young, J. D., Abbate, V., Imberti, C., Meszaros, L. K., Ma, M. T., Terry, S. Y. A., Hider, R. C., Mullen, G. E., & Blower, P. J. (2017). <sup>68</sup>Ga-THP-PSMA: A PET imaging agent for prostate cancer offering rapid, room-temperature, 1-step kit-based radiolabeling. *Journal of Nuclear Medicine*, 58(8), 1270–1277.
- Zettlitz, K. A., Tavaré, R., Knowles, S. M., Steward, K. K., Timmerman, J. M., & Wu, A. M. (2017). ImmunoPET of malignant and normal B cells with <sup>89</sup>Zr- and <sup>124</sup>I-labeled obinutuzumab antibody fragments reveals differential CD20 internalization in vivo. *Clinical Cancer Research*, 23(23), 7242–7252.
- Zhai, C., Franssen, G. M., Petrik, M., Laverman, P., Summer, D., Rangger, C., Haubner, R., Haas, H., & Decristoforo, C. (2016). Comparison of Ga-68-Labeled Fusarinine C-Based Multivalent RGD Conjugates and [<sup>68</sup>Ga]NODAGA-RGD—In Vivo Imaging Studies in Human Xenograft Tumors. *Molecular Imaging and Biology*, 18(5), 758–767.
- Zhai, C., Summer, D., Rangger, C., Franssen, G. M., Laverman, P., Haas, H., Petrik, M., Haubner, R., & Decristoforo, C. (2015). Novel bifunctional cyclic chelator for <sup>89</sup>Zr-labeling - radiolabeling and targeting properties of RGD conjugates. *Molecular Pharmaceutics*, 12(6), 2142–2150.
- Zhu, Z., Yin, Y., Zheng, K., Li, F., Chen, X., Zhang, F., & Zhang, X. (2014). Evaluation of synovial angiogenesis in patients with rheumatoid arthritis using <sup>68</sup>Ga-PRGD2 PET/CT: A prospective proof-of-concept cohort study. *Annals of the Rheumatic Diseases*, 73(6), 1269–1272.



# Supplementary material

**Supplementary Table 1.** *Ex vivo* biodistribution of <sup>68</sup>GaGa-NOTA-Folate in mice (STUDY III) at 60 minutes post-injection expressed as standardized uptake values (mean ± SD).

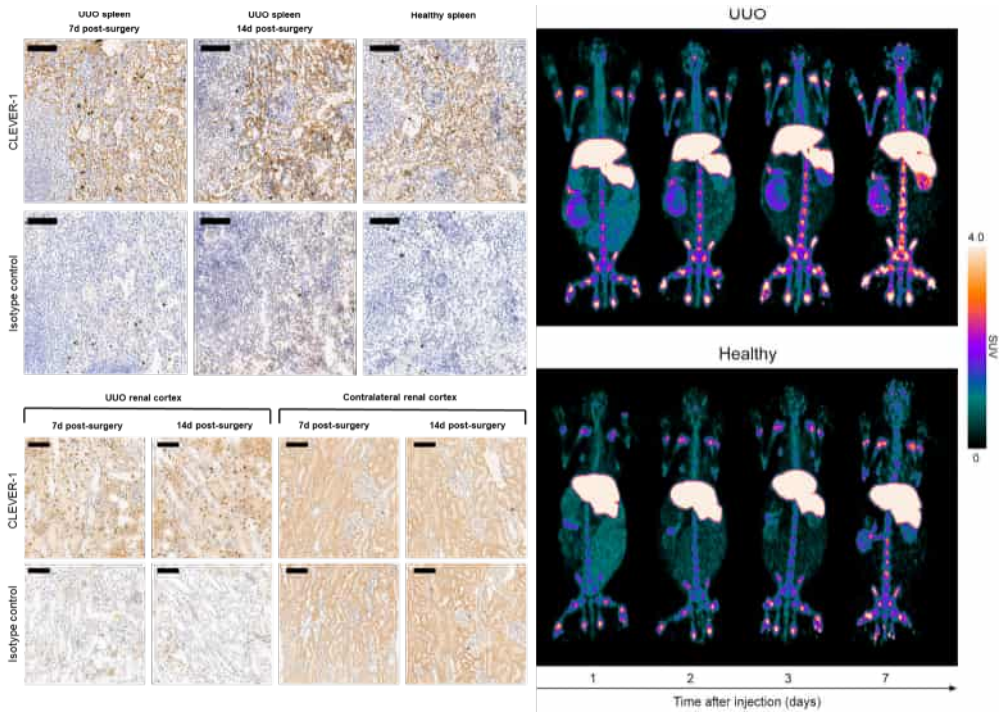
Tissue	Atherosclerotic mice ( <i>n</i> = 4)	Atherosclerotic mice, blocking ( <i>n</i> = 4)	C67BL/6JRj control mice ( <i>n</i> = 6)
Aorta	0.75 ± 0.12	0.09 ± 0.03 ( <i>P</i> = 0.001) <sup>a</sup>	0.41 ± 0.10 ( <i>P</i> = 0.004) <sup>b</sup>
BAT	0.29 ± 0.04	0.06 ± 0.02 ( <i>P</i> = 0.006) <sup>a</sup>	0.31 ± 0.05 ( <i>P</i> = 0.51) <sup>b</sup>
Blood	0.23 ± 0.09	0.29 ± 0.10 ( <i>P</i> = 0.48) <sup>a</sup>	0.25 ± 0.14 ( <i>P</i> = 0.84) <sup>b</sup>
Bone (skull)	0.13 ± 0.05	0.06 ± 0.02 ( <i>P</i> = 0.04) <sup>a</sup>	0.16 ± 0.04 ( <i>P</i> = 0.42) <sup>b</sup>
Bone + marrow (femur)	0.24 ± 0.18	0.07 ± 0.01 ( <i>P</i> = 0.17) <sup>a</sup>	0.18 ± 0.04 ( <i>P</i> = 0.57) <sup>b</sup>
Brain	0.08 ± 0.01	0.02 ± 0.00 ( <i>P</i> = 0.001) <sup>a</sup>	0.06 ± 0.01 ( <i>P</i> = 0.02) <sup>b</sup>
Heart	0.20 ± 0.02	0.05 ± 0.02 ( <i>P</i> < 0.001) <sup>a</sup>	0.24 ± 0.03 ( <i>P</i> = 0.04) <sup>b</sup>
Intestine, small (empty)	0.44 ± 0.06	0.42 ± 0.10 ( <i>P</i> = 0.84) <sup>a</sup>	0.47 ± 0.27 ( <i>P</i> = 0.76) <sup>b</sup>
Intestine, large (empty)	0.73 ± 0.14	0.19 ± 0.06 ( <i>P</i> = 0.003) <sup>a</sup>	0.66 ± 0.08 ( <i>P</i> = 0.38) <sup>b</sup>
Kidneys	22.30 ± 3.28	2.65 ± 1.80 ( <i>P</i> < 0.001) <sup>a</sup>	20.27 ± 5.48 ( <i>P</i> = 0.49) <sup>b</sup>
Lungs	0.46 ± 0.03	0.19 ± 0.04 ( <i>P</i> < 0.001) <sup>a</sup>	0.39 ± 0.06 ( <i>P</i> = 0.05) <sup>b</sup>
Liver	1.04 ± 0.43	0.33 ± 0.13 ( <i>P</i> = 0.04) <sup>a</sup>	0.76 ± 0.16 ( <i>P</i> = 0.29) <sup>b</sup>
Lymph node	1.37 ± 0.57	0.14 ± 0.02 ( <i>P</i> = 0.02) <sup>a</sup>	4.07 ± 0.73 ( <i>P</i> < 0.001) <sup>b</sup>
Muscle	0.20 ± 0.02	0.05 ± 0.01 ( <i>P</i> < 0.001) <sup>a</sup>	0.13 ± 0.02 ( <i>P</i> < 0.001) <sup>b</sup>
Pancreas	0.43 ± 0.06	0.07 ± 0.02 ( <i>P</i> < 0.001) <sup>a</sup>	0.37 ± 0.03 ( <i>P</i> = 0.17) <sup>b</sup>
Plasma	0.40 ± 0.15	0.48 ± 0.13 ( <i>P</i> = 0.44) <sup>a</sup>	0.34 ± 0.15 ( <i>P</i> = 0.61) <sup>b</sup>
Spleen	0.23 ± 0.07	0.15 ± 0.05 ( <i>P</i> = 0.11) <sup>a</sup>	0.28 ± 0.13 ( <i>P</i> = 0.42) <sup>b</sup>
Stomach (empty)	0.78 ± 0.14	0.25 ± 0.05 ( <i>P</i> = 0.002) <sup>a</sup>	0.65 ± 0.12 ( <i>P</i> = 0.17) <sup>b</sup>
Thymus	0.42 ± 0.13	0.06 ± 0.01 ( <i>P</i> = 0.01) <sup>a</sup>	0.33 ± 0.08 ( <i>P</i> = 0.25) <sup>b</sup>
WAT	0.22 ± 0.16	0.03 ± 0.01 ( <i>P</i> = 0.10) <sup>a</sup>	0.30 ± 0.08 ( <i>P</i> = 0.40) <sup>b</sup>

The blocking study was performed by injecting a 100-fold molar excess of folate glucosamine 1 minute before the [<sup>68</sup>Ga]Ga-NOTA-folate. P-values determined by independent samples *t*-test. <sup>a</sup>Difference between atherosclerotic mice vs. atherosclerotic mice + blocking, <sup>b</sup>Difference between atherosclerotic vs. control mice. BAT = brown adipose tissue; WAT = white adipose tissue. Atherosclerosis was induced by a high fat diet in LDLR-/-ApoB100/100 mice.

**Supplementary Table 2.** *Ex Vivo* Biodistribution of  $^{89}\text{Zr}$ -DFO-bexmarilimab in Rabbits

	24 hours after injection			7 days after injection		
	UUO ( <i>n</i> = 4)	Healthy ( <i>n</i> = 3)	<i>P</i> value	UUO ( <i>n</i> = 3)	Healthy ( <i>n</i> = 3)	<i>P</i> value
Kidney, UUO	1.93 ± 0.05		<0.001*	2.24 ± 0.26		0.010*
Kidney, contralateral	1.01 ± 0.05		<0.001†	3.62 ± 0.27		0.007†
Kidney, healthy		1.00 ± 0.11	0.819‡		1.39 ± 0.02	<0.001‡
Adrenal gland	1.78 ± 0.63	1.15 ± 0.09	0.206	1.39 ± 0.10	1.45 ± 0.29	0.809
Blood	0.47 ± 0.08	0.31 ± 0.01	0.029	0.14 ± 0.05	0.27 ± 0.22	0.463
Bone (femur)	0.40 ± 0.08	0.40 ± 0.13	0.992	0.81 ± 0.11	0.55 ± 0.08	0.062
Bone marrow	1.51 ± 0.10	1.09 ± 0.14	0.011	2.39 ± 0.18	1.52 ± 0.34	0.034
Brain	0.02 ± 0.00	0.02 ± 0.00	0.162	0.02 ± 0.00	0.01 ± 0.00	0.182
Cecum (with content)	0.98 ± 0.06	1.06 ± 0.17	0.487	0.13 ± 0.09	0.04 ± 0.03	0.212
Feces	1.19 ± 0.22	1.15 ± 0.19	0.844	0.10 ± 0.10	0.02 ± 0.00	0.298
Gall bladder	1.96 ± 0.90	3.14 ± 0.95	0.216	1.50 ± 0.66	1.27 ± 0.59	0.725
Heart	0.41 ± 0.06	0.20 ± 0.16	0.096	0.25 ± 0.03	0.26 ± 0.02	0.868
Large intestine, lower	0.10 ± 0.11	0.15 ± 0.01	0.577	0.17 ± 0.02	0.14 ± 0.01	0.089
Large intestine, upper	0.24 ± 0.03	0.20 ± 0.04	0.307	0.18 ± 0.01	0.14 ± 0.00	0.003
Liver	24.2 ± 2.28	22.9 ± 2.02	0.535	19.5 ± 1.81	22.4 ± 0.70	0.104
Lungs	0.42 ± 0.07	0.26 ± 0.16	0.193	0.32 ± 0.07	0.27 ± 0.02	0.379
Lymph node	0.92 ± 0.17	0.65 ± 0.30	0.250	0.71 ± 0.12	0.45 ± 0.10	0.079
Muscle	0.03 ± 0.00	0.03 ± 0.01	0.383	0.02 ± 0.00	0.02 ± 0.00	0.993
Ovary	1.01 ± 0.07	0.53 ± 0.19	0.013	0.67 ± 0.12	0.57 ± 0.06	0.395
Pancreas	0.17 ± 0.02	0.17 ± 0.06	0.904	0.19 ± 0.03	0.19 ± 0.06	0.957
Salivary gland	0.24 ± 0.05	0.20 ± 0.06	0.497	0.20 ± 0.03	0.15 ± 0.02	0.130
Skin	0.12 ± 0.02	0.12 ± 0.03	0.869	0.05 ± 0.02	0.05 ± 0.01	0.578
Small intestine	0.69 ± 0.32	0.34 ± 0.23	0.229	0.09 ± 0.02	0.04 ± 0.03	0.096
Spleen	6.10 ± 0.59	4.26 ± 1.53	0.124	7.42 ± 1.62	3.81 ± 0.16	0.035
Stomach (with content)	0.62 ± 0.33	0.54 ± 0.23	0.767	0.07 ± 0.01	0.03 ± 0.03	0.174
Thymus	0.12 ± 0.01	0.20 ± 0.13	0.325	0.17 ± 0.04	0.08 ± 0.00	0.022
Thyroid gland	0.12 ± 0.01	0.32 ± 0.24	0.227	0.15 ± 0.03	0.12 ± 0.04	0.432
Urinary bladder	0.43 ± 0.05	0.41 ± 0.06	0.656	0.26 ± 0.04	0.37 ± 0.14	0.355
Urine	0.42 ± 0.12	0.16 ± 0.17	0.246	0.16 ± 0.06	0.09 ± 0.04	0.240
Uterus	0.59 ± 0.06	0.45 ± 0.03	0.026	0.32 ± 0.07	0.18 ± 0.01	0.049
White adipose tissue	0.13 ± 0.05	0.05 ± 0.01	0.065	0.09 ± 0.02	0.04 ± 0.00	0.035

Results are expressed as standardized uptake values (SUV), mean ± SD. UUO = unilateral ureteral obstruction. *P* values are from independent samples *t*-test. \*UUO kidney versus healthy kidney; †UUO kidney versus contralateral kidney; ‡UUO rabbits' contralateral kidney versus healthy kidney.



**Supplementary Figure 1. Left:** Representative CLEVER-1 immunohistochemical staining of rabbits' spleen and renal cortex at different time points after UUU surgery as well as spleen from a healthy rabbit. There was no detectable difference in CLEVER-1 expression when comparing tissues collected 7 or 14 days after surgery. Scale bar is 100  $\mu$ m. **Right:** Sequential PET maximum intensity projection images of UUU-operated and healthy rabbits.